ROYAUME DU MAROC
Université Mohammed V - RABAT -
جامعة محمد الخامس – الرباط –
Faculté des sciences
كلية العلوم
CENTRE D'ETUDES DOCTORALES - SCIENCES ET TECHNOLOGIES

N° d'ordre **3732**

THESE

En vue de l'obtention du : ***DOCTORAT***

Structure de Recherche *: Laboratoire de Matière Condensée et Sciences Interdisciplinaires*
Discipline *: Physique*
Spécialité *: Matière Condensée, Nanomatériaux et Modélisation des Systèmes.*

Présentée et soutenue le 24/12/2022 Par :
Ahmed Ahmed Mohsen Al-Shami

Computational design of hybrid-Perovskite materials ($CH_3NH_3PbI_3$) for Photovoltaic and Photocatalytic applications: First Principles Study

JURY

Mohammed LOULIDI	**PES, Université Mohammed V, Faculté des Sciences, de Rabat**	**Président**
Ahmed HOURMATALLAH	**PES, Université Sidi Mohamed Ben Abdellah, Ecole Normale Supérieure, Fès**	**Examinateur/rapporteur**
Hamid EZ-ZAHRAOUY	**PES, Université Mohammed V, Faculté des Sciences, de Rabat**	**Examinateur/rapporteur**
Abdeljalil RACHADI	**PES, Université Mohammed V, Faculté des Sciences, de Rabat**	**Examinateur/rapporteur**
Abdelilah BENYOUSSEF	**PES/Expert, Académie Hassan II des sciences et techniques-Rabat**	**Examinateur**
Mustapha JOUIAD	**PES, Université de Picardie Jules Verne, France**	**Examinateur**
Omar MOUNKACHI	**PH, Université Mohammed V, Faculté des Sciences, de Rabat**	**Co-Directeur de Thèse**
Abdallah El KENZ	**PES Université Mohammed V, Faculté des Sciences, de Rabat**	**Directeur de Thèse**

Année Universitaire : 2022-2023

✉ Faculté des Sciences, avenue Ibn Battouta, BP. 1014 RP, Rabat –Maroc
☎ 00212 (05) 37 77 18 76 🖷 00212(05) 37 77 42 61; http://www. fsr.um5.ac.ma

إهداء

اهدي تخرجي إلى اغلى من في حياتي الحاضرين في قلبي

ومن كان دعاؤهم سر نجاحي كم كنت أتمنى وجودهم في هذا اليوم المميز بالنسبة لي

والدي الحبيبين حفظهما الله وأدامهما لي

إلى أخي الغالي محمد وكل اخواتي الغاليات

إلى رفيق دربي في مرحلة الدكتوراة أخي وصديقي عبده احمد محرز ملهي

لكل من علمني كلمة أو فكرة أو درس في الحياة.

إلى كل من كان سبباً وعوناً لي في تحقيق أحلامي

إلى كل أساتذتي . . . شكراً لكم جميعاً

Acknowledgments

This thesis was carried out at the Laboratory of Condensed Matter and Interdisciplinary Sciences (LaMCScI) of Faculty of Science, University of Mohammed V-Rabat, Morocco under the supervision of Prof. **Abdallah EL KENZ**

I am immensely grateful to my Principal supervisor, Professor **Abdallah EL KENZ**, for his invaluable guidance and support throughout my research and dissertation writing. He was always generous with his time and provided me with insightful and inspiring discussions, as well as invaluable advice. I am particularly thankful for the opportunities he gave me to attend international scientific conferences, which allowed me to learn from renowned researchers and establish valuable collaborations.

I extend my heartfelt gratitude to Professor **Omar MOUNKACHI**, of the Faculty of Sciences at the University of Mohammed V in Rabat, for his invaluable co-supervision, guidance, and assistance. I am deeply appreciative of his encouragement and support throughout my research and publications. I am particularly thankful for the opportunities he provided me to attend international scientific conferences, which allowed me to learn from renowned researchers and establish valuable collaborations.

I would also thank the thesis committee for reviewing my work and giving their insightful and useful comments. It is an honor for me that they agreed to judge this work.

I wish to thank Prof. **Mohammed LOULIDI** from University Mohammed V-Rabat, Faculty of Science, to be the president of the jury members of this thesis and for his patience in revising my papers and thesis, for providing invaluable insights and constructive criticism

to the work I have done.

I would like also to offer my sincerest gratitude to Prof. **Ahmed HOURMATALLAH** PES Ecole Normale Supérieure - Fes, Sidi Mohamed Ben Abdellah University, for reporting and examining my PhD thesis.

would like also to offer my sincerest gratitude Prof. **Hamid EZ-ZAHRAOUY** from International University of Rabat, for reporting and examining my Ph.D. thesis.

I would also like to extend my thanks to Prof. **Abdeljalil RACHADI** from University Mohammed V-Rabat, Faculty of Science, for reporting and examining this PhD thesis.

I would like to express my very great appreciation, deep gratitude and sincere thanks to Prof **Abdelilah BENYOUSSEF**, from the Académie Hassan II des sciences et techniques-Rabat, for examining this thesis and also for his indispensable practical teaching and supervision, for extended discussions and valuable suggestions which have contributed greatly to the improvement of the thesis. I would like to express my very great appreciation, deep gratitude and sincere thanks to Prof **Mustapha JOUIAD**, from the University of Picardie Jules Verne, for examining this thesis.

I am grateful for the assistance offered by members of the Laboratory of Condensed Matter and Interdisciplinary Sciences (LaMCScI) of Faculty of Science, University of Mohammed V-Rabat, for their useful discussions, contributions, and friendship.

Personal thanks and love to my family that supported me during the years of my study. Without their love and support I could never have achieved everything that I have in life.

Most importantly, I must express sincere gratefulness to my mother and father for bringing me to this wonderful world, and all my teachers (direct and indirect teachings from nature as well) since my childhood for bringing me up to this stage.

Abstract

Solar energy is the most abundant and cleanest renewable energy source. In recent years, the era of perovskites has experienced splendid development. Among perovskites, flexible perovskite solar cells have received increasing attention due to their high efficiency, light weight, low cost, excellent flexibility, Due to the novelty of these materials, they lack complete and accurate knowledge of many of their properties, advantages, and developments. Based on this, we decided to do an in-depth study on the influence of the different strategies used to improve the properties of $CH_3NH_3PbI_3$ in two parts. The first part investigated the effect of strain on the electronic properties and electrical conductivity by controlling the band gap of the material. In addition, we investigated the improvement of power conversion efficiency (PCE) through cation replacement. where the study showed a significant increase of these effects on the electronic properties and an increase in the (PCE)to 25% with the NH3OHPbI3 cation. We also discussed in the second part the formation of a heterostructure of Fe_2O_3, $CH_3NH_3PbI_3$, and ZnO to split water and produce hydrogen gas while protecting $CH_3NH_3PbI_3$ from degradation by water. Fe_2O_3 has significantly increased the oxidation process. As for ZnO, it is a transparent carrier that transfers electrons while allowing photons of light to reach $CH_3NH_3PbI_3$ and, most importantly, protects the degradation of $CH_3NH_3PbI_3$. where the study showed a production of about 150 moles/gram.

Keywords: perovskite, photovoltaic, photocatalysis, first-principles calculation, strain effect, substation, cation.

Résumé

L'énergie solaire est la source d'énergie renouvelable la plus propre et la plus abondante qui existe. Ces dernières années, l'ère des matériaux pérovskites a connu un développement immense. Parmi eux, les cellules solaires flexibles en pérovskite ont reçu une attention croissante en raison de leur haut rendement, légèreté, faible coût et de leur excellente flexibilité. En raison de la nouveauté de ces matériaux, il manque une connaissance complète et précise de leurs propriétés, avantages et développement. Partant de ce constat, nous avons décidé de réaliser une étude approfondie sur l'influence des différentes stratégies utilisées pour améliorer les propriétés du pérovskite $CH_3NH_3PbI_3$ en deux parties. Dans la première partie, nous avons étudié l'effet de la contrainte sur les propriétés électroniques et la conductivité électrique en contrôlant la bande interdite du matériau. En plus, nous avons étudié l'amélioration de l'efficacité de conversion de puissance (PCE) par le remplacement des cations où l'étude a montré une augmentation significative de ces effets sur les propriétés électroniques et une augmentation du (PCE) à 25% avec le cation NH3OHPbI3. Nous avons également discuté dans la deuxième partie de la formation d'une hétérostructure de Fe_2O_3, $CH_3NH_3PbI_3$, et ZnO pour séparer l'eau et produire du gaz hydrogène tout en protégeant $CH_3NH_3PbI_3$ de la dégradation par l'eau. Fe_2O_3 a considérablement augmenté le processus d'oxydation. Quant au ZnO, c'est un support transparent qui transfère les électrons tout en permettant aux photons de lumière d'atteindre le $CH_3NH_3PbI_3$ et surtout de protéger la dégradation du $CH_3NH_3PbI_3$. L'étude a montré une production d'environ 150 moles/gramme.

Mots-clefs : Pérovskite, Photovoltaïque, Photocatalyse, DFT, Effet de contrainte, Cation.

Résumé détaillé

L'énergie solaire est une source d'énergie renouvelable propre et abondante qui a gagné en popularité ces dernières années. L'un des domaines les plus prometteurs de la recherche sur l'énergie solaire est le développement de cellules solaires à pérovskite, en particulier de cellules solaires à pérovskite flexibles. Ces cellules présentent plusieurs avantages par rapport aux cellules solaires traditionnelles, notamment un rendement élevé, un poids léger, un faible coût et une excellente flexibilité. Cependant, malgré le potentiel de ces matériaux, on manque encore de connaissances complètes et précises sur leurs propriétés, leurs avantages et leur potentiel de développement.

Pour combler cette lacune dans les connaissances, nous avons décidé de mener une étude approfondie sur l'influence des différentes stratégies utilisées pour améliorer les propriétés de $CH_3NH_3PbI_3$, un type de matériau pérovskite. L'étude a été divisée en deux parties.

Dans la première partie, nous avons étudié l'effet de la contrainte sur les propriétés électroniques et la conductivité électrique de $CH_3NH_3PbI_3$. En contrôlant la bande interdite du matériau, nous avons pu observer une amélioration significative des propriétés électroniques et une augmentation du rendement de conversion de puissance (PCE) à 25%. De plus, nous avons étudié l'effet du remplacement des cations sur le PCE du matériau. Nos résultats ont montré que l'utilisation du cation NH3OH entraînait une augmentation significative de la PCE.

Dans la deuxième partie de notre étude, nous avons exploré la formation d'une hétérostructure de Fe_2O_3, $CH_3NH_3PbI_3$ et ZnO. Cette hétérostructure a été conçue pour séparer l'eau et produire de l'hydrogène gazeux tout en protégeant $CH_3NH_3PbI_3$ de la dégradation par

l'eau. Il a été constaté que Fe_2O_3 augmentait considérablement le processus d'oxydation, tandis que ZnO agissait comme un support transparent qui transférait des électrons tout en permettant aux photons de lumière d'atteindre CH3NH3PbI3. Fait important, l'utilisation de ZnO a également protégé $CH_3NH_3PbI_3$ de la dégradation par l'eau. Nos résultats ont montré que cette hétérostructure produisait environ 151 moles/gramme d'hydrogène gazeux.

Dans l'ensemble, notre étude fournit de nouvelles informations sur les propriétés et le potentiel des matériaux pérovskites, en particulier $CH_3NH_3PbI_3$. Les résultats de notre étude démontrent qu'en contrôlant la bande interdite et le remplacement des cations, il est possible d'améliorer les propriétés électroniques et l'efficacité des cellules solaires $CH_3NH_3PbI_3$. De plus, notre étude met en évidence le potentiel d'utilisation d'une hétérostructure de Fe_2O_3, $CH_3NH_3PbI_3$ et ZnO pour produire de l'hydrogène gazeux tout en protégeant $CH_3NH_3PbI_3$ de la dégradation. Ces découvertes ouvrent la voie à de nouvelles recherches et développements dans le domaine des cellules solaires à pérovskite.

Le premier chapitre, Introduction, examine l'évolution des technologies de cellules solaires et les propriétés des pérovskites hybrides $CH_3NH_3PbI_3$. La structure moyenne de $CH_3NH_3PbI_3$ est discutée, y compris sa phase cubique à des températures supérieures à 327 K, sa phase tétragonale entre 165-327 K et sa phase orthorhombique à des températures inférieures à 165 K. De plus, la structure cristalline de la pérovskite $CH_3NH_3PbI_3$ est discutée et le développement d'hybrides la technologie pérovskite est couverte.

Le deuxième chapitre, Théorie et méthodes de calcul: explore les fondements de la chimie quantique et ses premières théories. L'équation de Schrödinger et la théorie fonctionnelle de la densité sont discutées, ainsi que la structure cristalline et le théorème de Bloch. Le chapitre couvre également Plane- Waves et la méthode Projector Augmented Wave (PAW) En outre, le chapitre se penche sur le calcul de la dynamique moléculaire, y compris les logiciels et

la modélisation utilisés tels que Quantum Espresso, le code BoltzTraP et les méthodes de calcul pour l'efficacité de conversion de puissance, l'effet de contrainte et le transport, et l'hétérostructure. Photocatalyse.

Le troisième chapitre, Efficacité et substitution des cations organiques, commence par une introduction et examine le facteur de tolérance et le facteur octaédrique. Le chapitre comprend également une évaluation de l'efficacité, des résultats et de la discussion, de l'optimisation, des propriétés électroniques, de la stabilité, des propriétés optiques et de l'efficacité de conversion de puissance (PCE). Le chapitre se termine par un résumé des résultats et des conclusions.

"Le quatrième chapitre, Propriétés électroniques et de transport de $CH_3NH_3PbI_3$, commence par une introduction et explore les résultats et la discussion du paramètre de relaxation optimal pour les propriétés organométalliques, structurelles, électroniques et thermiques, les propriétés de transport, les effets de contrainte sur la structure de bande électronique , effet de contrainte sur la structure du réseau, structure de bande avec contrainte, bande interdite avec contrainte, énergie de Fermi avec contrainte, effet de contrainte sur la distribution de charge et propriétés thermoélectriques de $MAPbI_3$ sous contrainte De plus, le chapitre couvre la conductivité électrique, la densité de porteurs et la mobilité . Le chapitre se termine par un résumé des constatations et des conclusions.

Le cinquième chapitre, Activité photocatalytique améliorée, commence par une introduction et explore les résultats et la discussion de la fabrication d'hétérostructures et de l'extraction d'électrons d'interface, du mécanisme de fractionnement de l'eau, du rendement de production de H2, de la stabilité thermique et des propriétés optiques. Le chapitre se termine par un résumé des résultats et des conclusions.

"Le dernier chapitre, Conclusion générale et perspectives: résume les principaux résultats de la recherche, met en évidence l'importance de l'étude et donne un aperçu des contributions

apportées au domaine. De plus, le chapitre présente des perspectives sur les orientations futures de la recherche. et les zones potentielles pour une exploration plus approfondie.

List of Publications

0.0.1 Journal publications

1. **A. Al-Shami**, M. Lakhal, M. Hamedoun, A. El Kenz, A. Benyoussef, M. Loulidi, A. Ennaoui, O. Mounkachi, Tuning the optical and electrical properties of orthorhombic hybrid perovskite CH3NH3PbI3 by first-principles simulations: Strain-engineering, Solar Energy Materials and Solar Cells. 180 (2018) 266–270. doi:10.1016/j.solmat.2017.06.047.

2. **A. Al-shami**, A. Sibari, A. El Kenz, A. Benyoussef, A. El Moutaouakil, O. Mounkachi, Improved Power Conversion Efficiency with Tunable Electronic Structures of the Cation-Engineered $[A_i]PbI_3$ perovskites for Solar Cells: First-Principles Calculations, (2022).

This paper is under submission during the candidature. It was produced as Chapter 3 in this thesis.

2. **Ahmed Al-Shami**, Anass Sibari, Zouhir Mansouri, Majid El Kassaoui, Abdallah El Kenz, Abdelilah Benyoussef, Mohammed Loulidi, Mustapha Jouiad, and Omar Mounkachi, Photocatalytic properties of ZnO:Al/ $MAPbI_3$/ Fe_2O_3 heterostructure.

0.0.2 Manuscripts under preparation

1. *Layer Engineering in **Optoelectronic** and Photonic Properties of Single and few Layers Phosphorene using first-principles calculations.*

2. ***Piezoelectric Polarization** of FAPbI3: A Detailed Study Based on DFT.*

3. ***Thermoelectric** characteristics of Bulk Black Phosphorus under strain-engineering: A first principle study.*

5. *Phosphorene-δ Heterostructure as Anode Material for High Performance* ***Lithium-Ion Batteries****: First Principles insights*

6. *Influence of the surface decoration of graphene with phosphorus nano-clusters on* ***Gas Sensing*** *properties*

7. *A first principles study of* ***Hydrogen Storage*** *in lithium decorated defective phosphorene-δ*

8. *Electrochemical and theoretical examinations of the intercalation of two compounds as excellent* ***Corrosion Inhibitors*** *for the Carbon Steel in a 3% HCl solution.*

0.0.3 Co-authored journal publications ascribing to collaboration

1. A. Akrouchi, H. Benzidi, **A. Al-Shami**, A. El kenz, A. Benyoussef, A. El Kharbachi, O. Mounkachi, First-principles study of closo-dodecaborates M2B12H12 (M = Li, Na, K) as solid-state electrolyte materials, Physical Chemistry Chemical Physics. 23 (2021) 27014–27023. doi:10.1039/D1CP03215A.

2. Z. Mansouri, A. Sibari, **A. Al-Shami**, S. Lahbabi, A. El Kenz, A. Benyoussef, A. El Fatimy, O. Mounkachi, Graphene/Phosphorene nano-heterostructure as a potential anode material for (K/Na)-ion batteries: Insights from DFT and AIMD, Computational Materials Science. 202 (2022). doi:10.1016/j.commatsci.2021.110936.

3. A. Boubekraoui, H. Moatassim, **A. Al-Shami**, H. Ez-Zahraouy, DFT study of structural, electronic, and thermoelectric properties of Cs2PdX(X=Br2Be2Te2) compound, Computational Condensed Matter. 29 (2021) e00600. doi:10.1016/j.cocom.2021.e00600.

4. M. EL Kassaoui, Z. Mansouri, A. **Al-Shami**, A. Sibari, A. Benyoussef, A. El Kenz, O. Mounkachi, M. Loulidi, Design of metal-decorated beryllium carbide (Be2C) as a high-capacity hydrogen storage material with strong adsorption characteristics, Applied Surface Science. 589 (2022) 152960. doi:10.1016/j.apsusc.2022.152960.

5. I. Zdeg, A. **Al-Shami**, G. Tiouichi, H. Absike, V. Chaudhary, P. Neugebauer, K. Nouneh, A. Belhboub, O. Mounkachi, A. El Fatimy, Electrical Transport Properties of Layered Black Phosphorus grown by Chemical Vapor Transport, 2200164 (2022) 1–6. doi:10.1002/crat.202200164.

6. L. Taouil, **A. Al-Shami**, H. Ez-Zahraouy, Biaxial strain and electric field effects on the electronic, optical, and photocatalytic properties of full hydrogenated SiSn monolayer, Materials Science in Semiconductor Processing. 153 (2023) 107068. doi:10.1016/j.mssp.2022.107068.

7. L. Attou, **A. Al-Shami**, J. Boujemaa, O. Mounkachi, H. Ez-Zahraouy, Predicting the structural, optoelectronic, dynamical stability and transport properties of Boron-doped $CaTiO_3$: DFT based study, Physica Scripta. 97 (2022) 115808. doi:10.1088/1402-4896/ac95d8.

Research aims and scope

In order for these perovskites to be optimized for use in commercial devices, detailed knowledge of material behavior is needed. As we know, some of the best-performing PV devices include site-substituted perovskite materials (ABX3), where the A-sites are occupied by varying ratios of another cation. On the other hand, perovskite is subjected to strain due to many factors, such as compression or tension, and its effect on transport properties. In addition, the degradation is due to its interaction with oxygen or water and the exploitation of that in the splitting water process. Despite the popularity of site substitution, the strain effect, and coupling with other materials in PV device research, its effect on the fundamental structural properties of perovskites was largely unknown. To address this question, the work aimed to characterize perovskite material in its ideal form.

Research question

The motivated overarching research question addressed in this thesis is: what effect do site substitution, strain, and coupling have on the structure of lead halide perovskites for photovoltaics and photocatalysis?

RESEARCH PROBLEM

The special and remarkable electronic and physical properties of perovskite materials, such as high carrier mobility, good light absorption, mechanical flexibility, and thermal conductivity, have given rise to promising research in both fundamental and applied areas. Although there has been immense research progress in the last decade on these materials, many challenges remain regarding the number of materials that are yet to be studied, characterized, and compared to their bulk counterparts in order to identify possible applications in solar cells, water splitting, and nanoelectronics.

(a) It is determined from a literature review that new materials made of perovskites are significantly less studied than other materials, and there is a shortfall of theoretical data on their properties. There are a few available experimental results, but they have not yet been compared with theoretical studies. This computational investigation based on DFT and MD is undertaken to check their applicability in water splitting and photovoltaic applications.

(b) Further study on suitable materials for use as hole transport materials (HTMs) in perovskite solar cells (PSCs) is highly desired for this fast-growing perovskite field. A new class of organic molecular compounds and other inorganic molecular compounds are considered using DFT analysis to delineate their suitability in PSCs and thus in solar energy applications. The research gap is very clear, and my research contributes to filling this gap to some

extent and will pave the way for selecting new materials for solar cells or in water-splitting studies.

Research Aim

The fundamental aim of the study is to identify and suggest new materials for improving the efficiency of solar based technologies. Under the above aim, the specific goals selected are: -

Goal (1) Methylaminum ions in a perovskite decompose due to the presence of oxygen during illumination. Therefore, we urgently need to look for more stable cations in the presence of oxygen (O2) or water (H2O).

Goal (2) Photo-catalysis applications for clean solar fuel production for solar water splitting to generate hydrogen and oxygen.

Goal (3) Perovskites are subject to stress in ambient conditions. What is the effect of stress on optical and transport properties?

List of abbreviations

DoE	Department of Energy	ab initio	First principal calculation	ab initio	First principal calculation
CNTs	Carbon nanotubes	Ψ	Many-body wave function of electrons	DSSC	the dye sensitized solar cell
MOFs	Metal organic framework	$\hbar$	Planck's constant devised by 2π	HPs	hybrid perovskite
TPES	Total primary energy supply	e	Charge of the electron	HTMs	Hole Transport Materials
GHG	Greenhouse gas	m_e	Mass of the electron	PSCs	Perovskite solar cells
PV	Photovoltaics	M_I	Mass of the nucleus	PV	Photovoltaic
ICE	Internal combustion engine	Z_I	Charge of the nucleus		
PEM	proton exchange membrane	R_I	Position of the nuclei		
PEMFC	proton exchange membrane fuel cell	r_i	Position of electron		
DMFC	Direct Methanol Fuel Cell	T_e	Kinetic energies of the electrons		
PAFC	Phosphoric Acid Fuel Cell	T_n	kinetic energies of the the nuclei		
AFC	Alkaline Fuel Cell	V_{int}	Internal potential		
SOFC	Solid Oxide Fuel Cell	V_{ext}	External potential		
MCFC	Molten Carbon Fuel Cell	V_{nn}	nucleus-nucleus potential		
COFs	Covalent organic frameworks	$n_H(z)$	Number of hydrogen in plan z		
PIMs	Polymers of intrinsic micro-porosity	$n_S(z)$	Number of interstitial sites in plan z		
SWNT	Single wall structure	$\rho(z)$	Density of Hydrogen in plan z		
MWNT	Mmultiple wall structure	t_{eq}	Equilibrium time		
HCP	Hexagonal close-packed	t_f	Filling time		
DC	Direct current	t_r	Relaxation time		
RF	Radio frequency	V_{ee}	Electron electron potential		
UHV	Ultra-high vacuum	V_{KS}	Effective potential		
C_g	Gravimetric capacity	$V_H(r)$	Hartree potential		
C_v	Volumetric capacity	$V_{xc}(r)$	Exchange-correlation potential		
wt.	Weight	$\hat{H}$	Hamiltonian operator		
T_{des}	Desorption Temperature	Z	Partition function		
P	Equilibrium pressure	LDA	Local density approximation		
T	Temperature	LSDA	Local Spin-Density approximation		
R	The gas constant	GGA	Generalized gradient approximation		
E_a	Activation energy	MC	Monte Carlo		
K_β	Boltzmann constant	MMC	Metropolis Monte Carlo		
G	Free energy	MCMC	Markov chain Monte Carlo		
ΔH	Heat of formation	KMC	Kinetic Monte Carlo		
ΔS	Entropy	ΔE	Energies difference		
E_{tot}	Energy total	F	Hydrogen flux		
DOS	Density of states	M_{H_2}	Molecular mass of hydrogen		
PDOS	Partial desnity of states	P_i	probability		
VB	Valence band	R_i	The rate transition		
CB	Conduction band	R	Total rate transition		
TM	Transition metal	DFT	Density functional theory		
DOS	Density of states	M_{H_2}	Molecular mass of hydrogen		
PDOS	Partial desnity of states	P_i	probability		
VB	Valence band	R_i	The rate transition		
CB	Conduction band	R	Total rate transition		
TM	Transition metal	DFT	Density functional theory		

Contents

List of Figures

List of Tables

Part I

Background

CHAPTER 1

Background

1.1 INTRODUCTION

This chapter discusses the motivation, background, and previous work for the topic of perovskite photovoltaic. Photovoltaic (PV) cells convert sunlight into electrical current. Among various renewable resources, solar energy is very attractive because of its abundance. In addition, solar energy is clean and safe. However, current PV technology is not cost effective for bulk power generation under most circumstances. As shown in Figure 1.1, many different types of solar cells have been investigated [5]. Among them, crystalline silicon (Si) technologies are well established, with over 80% of the total PV market share as of 2011 and a history of over 40 years [6,7]. Crystalline Si solar cells have relatively high energy conversion efficiency (η), up to 25%, because of a nearly optimum band gap (Eg) of 1.1 eV. Any photons with energy lower than the band gap of a semiconductor will not be absorbed, while any energy from an absorbed photon in excess of the band gap of the material is rapidly lost to thermalization. Based on these considerations and a few other assumptions, Shockley and

Queisser established the performance limit of solar cells with a single absorbing material and a single band gap [8]. On earth's surface (the AM 1.5 spectrum), η can reach up to 34%, when $Eg \approx 1.4e$V. However, as an indirect gap material, Si is a poor absorber of light near its band gap compared to semiconductors with direct gaps [5]. In order to well absorb sunlight, the Si layer in a solar cell must be hundreds of μm in thickness, requiring extremely high quality pure crystals to avoid the electron and hole recombining near a defect.

1.2 Evolution of Solar Cell Technologies

The National Renewable Energy Laboratory (NREL) tracks the highest efficiencies achieved for all research PV devices. The annual chart is shown in Figure 1.1, which displays perovskite solar cell efficiencies as yellow/orange dots. Despite the first record only appearing in 2013, perovskite device efficiencies are now competing with established technologies like:

First Generation:

solar cells based on inorganic wafers such as silicon and gallium arsenate constitute first generation technologies. These technologies have the merit of high efficiencies over 20% but require the use of high cost processing techniques.

Second Generation:

The other hand third generation solar cell technologies based on thin . films have relatively lower efficiencies around 12% but can be easily processed at lower costs recently a new solar cell technology based on organic inorganic hybrid perovskite has emerged perovskite solar cell technology embodies both high efficiency and low cost.

Third Generation:

The other hand third generation solar cell technologies based on thin . films have relatively

lower efficiencies around 12% but can be easily processed at lower costs.

Recently, a new solar cell technology based on organic inorganic hybrid perovskite has emerged. Perovskite solar cell technology embodies both high efficiency and low cost Fig 1.2. The caveat is that many of these high efficiencies have been recorded on small lab scale

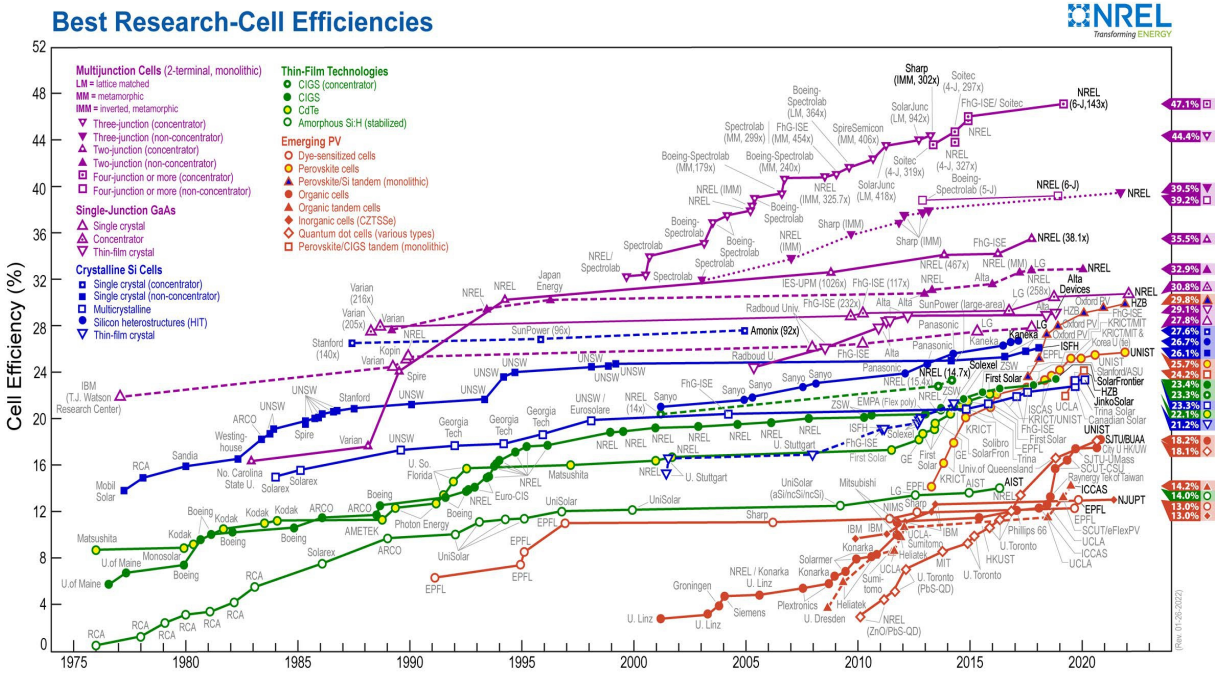

Figure 1.1: Perovskite solar cells have increased in power conversion efficiency at a phenomenal rate compared to other types of photovoltaics. Although this figure only represents lab based "hero cells" it heralds great promise [1] .

devices unsuitable for commercial use, although the community is currently turning its attention to the large-scale manufacture of perovskite PV devices [9]. Primary energy sources are still the most common form of energy production in the world today (nearly 88%), but there is a growing trend toward the use of renewable energy sources such as solar and wind power. Primary energy sources are still the most common form of energy production in the world today. Despite this, solar power is still rather costly in comparison to other traditional

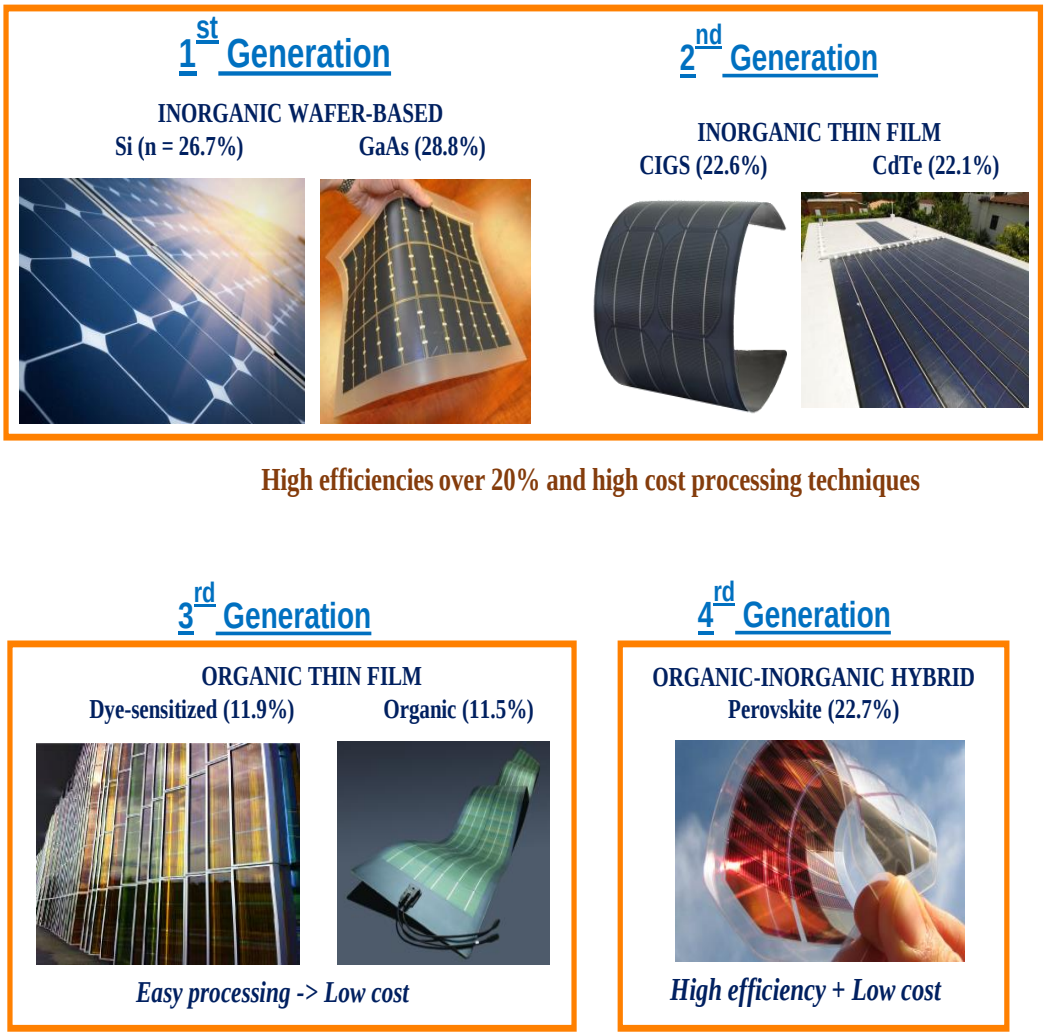

Figure 1.2: Generation solar cell technologies .

forms of energy, and it still accounts for a negligible portion of the overall production of electricity. A solar module, an inverter, and a number of other auxiliary components are the primary constituents of a standard photovoltaic system, which is used for the production of energy from sunlight. At the moment, the cost of the solar module alone accounts for more than fifty percent of the whole price. As a result, the development of modules that have lower manufacturing costs and greater efficiencies is essential if one want to see a reduction in the price of solar electricity in the foreseeable future. The efficiency with which solar cells convert energy into usable form is one of the primary criteria that is considered while evaluating the potential of this technology. It is the ratio of the amount of energy that is produced by solar cells to the amount of energy that is received from the sun. My research for my thesis is especially centered on the usage of solar power as a source of sustainable and environmentally friendly energy Fig 1.3.

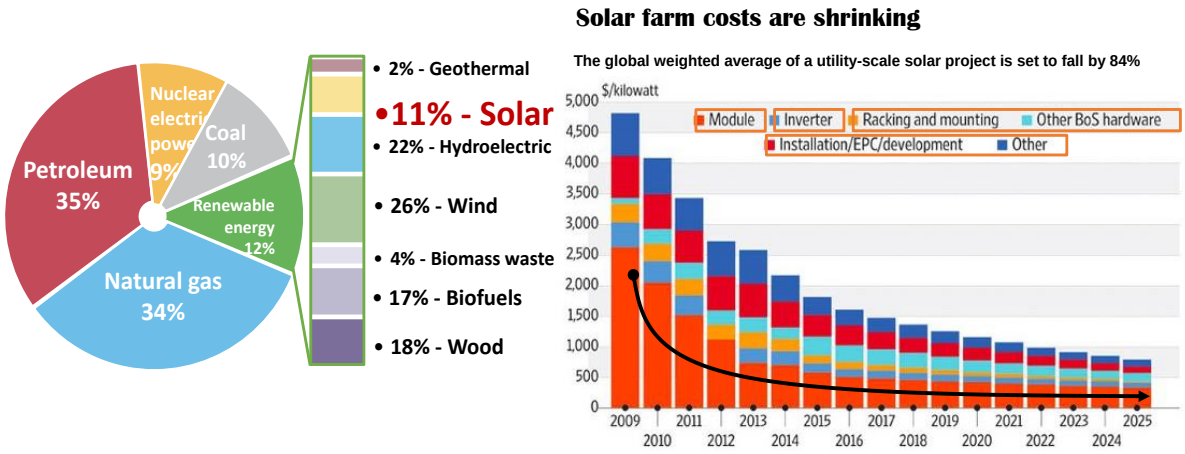

Figure 1.3: primary energy sources are still the most dominant form of energy production in the world today, but there is an increasing trend toward the use of renewable energy sources such as solar and wind power [2] .

Perovskite

The word 'perovskite' refers to the mineral form of $\mathrm{CaTiO_3}$. It adopts a crystal structure consisting of corner-sharing $\mathrm{TiO_6}$ octahedra in three dimensions, with Ca occupying the cuboctahedral cavity in each unit cell. The same crystal structure is also found for a wide range of materials with $\mathrm{ABX_3}$ stoichiometry, with two notable cases being $\mathrm{SrTiO_3}$ and $\mathrm{BaTiO_3}$. Examples of insulating, semiconducting and superconducting perovskite structured materials are known. These materials are the archetypal systems for phases transitions with accessible cubic, tetragonal, orthorhombic, trigonal and monoclinic polymorphs depending on the tilting and rotation of the $\mathrm{BX_3}$ polyhedra in the lattice [10]. Reversible phase changes can be induced by a range of external stimuli including temperature, pressure and magnetic or electric fields. For halide perovskites, the oxidation states of the two cations must sum to three, so the only viable ternary combination is $\mathrm{I{-}II{-}X_3}$, e.g. $\mathrm{CsPbI_3}$. In hybrid halide perovskites such as $\mathrm{CH_3NH_3PbI_3}$, a divalent inorganic cation is present and the monovalent metal is replaced by an organic cation of equal charge as illustrated in Fig. 1.5. In principle, any molecular cation could be used, once there is sufficient space to fit it within the cavity. If the cation size is too large, then the three-dimensional (3D) perovskite network is broken, as demonstrated in the series of hybrid structures with lower dimensionality in the inorganic networks [11]. For layered structures, the crystal properties become highly anisotropic with larger carrier masses and stronger exciton binding energies.

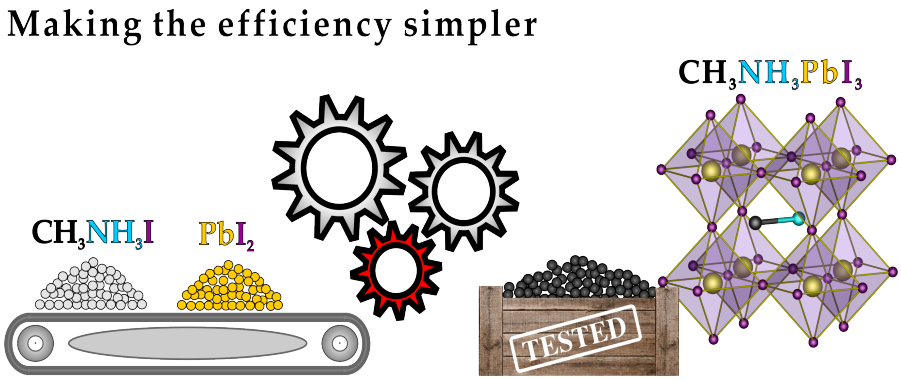

Figure 1.4: Mcthylammonium Lead Iodide $CH_3NH_3PbI_3$ is an organomctal halide perovskite system that is used as an absorber in solar cells. co-evaporation of Methylammonium Iodide (CH_3NH_3I) and Lead Iodide (Pbl_2) require treatment of the resulting $CH_3NH_3PbI_3$ thin film to catalyze the reaction between CH_3NH_3I and Pbl_2 and create a pure perovskite phase.

1.3 Hybrid perovskites $CH_3NH_3PbI_3$

The term hybrid perovskite has been employed to describe perovskite structure where the octahedral network was composed of an inorganic compound, while the central A cation is a small organic molecule, usually an amine. In literature, this class of compounds can also be named Metallo-organic perovskite, with the correspondent IUPAC name R-ammonium metal halide. We will stick with the term hybrid perovskite since it is affirmed and quite concise and precise at the same time. In general, the term hybrid will indicate the presence of organic and inorganic components. The general chemical formula for these compounds is RMX_3. The most studied organic groups R at the center of the cage are methylammonium (MA: CH_3NH_3) and formamidinium (FA: $CH(NH_2)_2^+$). The most common metals in the B-site are Pb and Sn, but other compounds with isovalent metals have been reported. The anion is a halide chosen between Cl, Br, and I. Previously we explained that it is possible to forecast

the presence of a perovskite phase by observing the value of the t-factor and μ. Those values are derived from the model of a hard-sphere, and it is not directly applicable to the MA cation. We adapted the model assuming two different parameters, one is half the length of the molecule (156 pm), and the other, slightly smaller, is the geometric average of the cylinder dimensions where the molecule can be inscribed (146 pm). The final values of t-factors are not significantly affected. Table 3.2 reports the example values of t and μ parameters for different $MAPbX_3$ materials. The parameter found, as observed and previously reported,101 even with some approximation lies in the range for perovskite structure, but are quite far from being ideal. The presence of the molecule breaks the symmetry of the crystal and induces different distortions. Besides the molecules are not held fixed in some position and orientational disorder increases with temperature.

1.3.1 Average Crystal Structure of $CH_3NH_3PbI_3$

Weber first reported $MAPbI_3$ in the cubic perovskite crystal structure (O_h point group), [12] which is inconsistent with the anisotropy of the static molecular building block ($CH_3NH_3^+$ is of C_{3v} point group). However, the molecular cations are orientationally disordered in the crystal, giving rise to an effective higher lattice symmetry on average [13]. Early work on the characterization of the crystal structure identified three phases of $\mathrm{MAPbI_3}$: orthorhombic, tetragonal and cubic Bravais lattices in order of increasing temperature [14]. While the position of Bragg peaks in X-ray diffraction can distinguish between the three phases, the peak intensities arising from $\mathrm{CH_3NH_3}^+$ relative to $\mathrm{PbI_2}^-$ are too weak to assign accurate molecular.

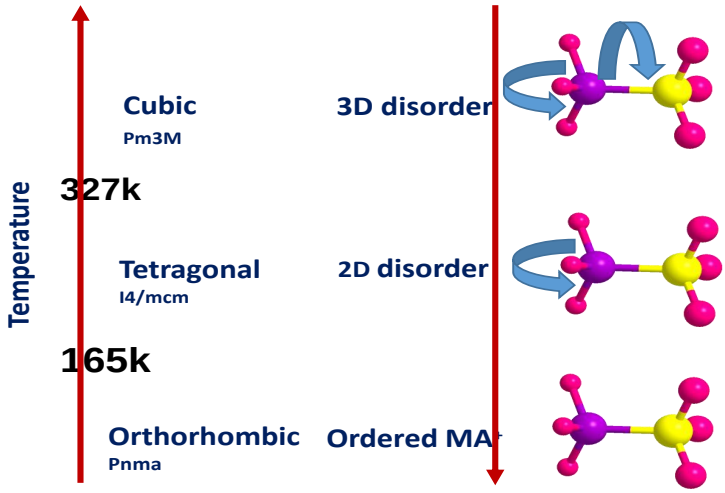

Figure 1.5: Temperature-dependent (100-352 K) powder neutron diffraction pattern of $CH_3NH_3PbI_3$ [3] adapted by permission of the Royal Society of Chemistry. The space groups of the average crystals structures are shown, along with a schematic of the extent of disorder in the $CH_3NH_3^+$ sublattice.

Material	Crystal system	T_c (K)	Crystal system	T_c (K)	Crystal system
$CH_3NH_3PbI_3$	Orthorhombic	< 165	Tetragonal	< 327	Cubic

Table 1.1: Crystal system with transition temperatures of perovskite $CH_3NH_3PbI_3$.

1.3.2 Cubic Phase (T > 327 K)

With increasing temperature the tetragonal lattice parameters become more isotropic with $\frac{c}{2a}$ moving closer to 1. The molecular disorder also increases to the point where a transition to a cubic phase occurs around $327K$. The transition can be seen clearly from changes in the heat capacity, [15] as well as in temperature-dependent neutron diffraction [3]. The cubic space group has been assigned the space group $Pm\bar{3}m$ (O_h symmetry); however, the local structure will necessarily have a lower symmetry. Indeed, for the bromide and chloride analogues of MAPI, pair-distribution function analysis of X-ray scattering data indicates a local structure

with significant distortion of the lead halide framework at room temperature [11].

1.3.3 Tetragonal Phase (165–327 K)

At 165 K, MAPI goes through a first-order phase transition from the orthorhombic to the tetragonal space group $I4/mcm$ (D_{4h} point group), which continuously undergoes a second-order phase transition to the cubic phase by ca. 327 K [3, 16]. As with the orthorhombic phase, this can be considered $a\sqrt{2a} \times \sqrt{2a} \times \sqrt{2a}$ expansion of the cubic perovskite unit cell. The molecular cations are no longer in a fixed position as in the orthorhombic phase. $\mathrm{CH_3NH_3}^+$ is disordered between two non-equivalent positions in each cage. [13], [17] The tetragonal distortion parameter in the cubic basis is greater than unity ($\frac{c}{2a}$ 1.01 at 300 K), corresponding to an elongation of the $\mathrm{PbI_6}$ octahedra along the c axis. The associated octahedral tilting pattern is $a^0a^0c^-$ in Glazer notation.

1.3.4 Orthorhombic Phase (T < 165 K)

The orthorhombic perovskite structure is the low temperature ground state of MAPI and maintains its stability up to ca. 165 K [18] [3, 16]. A comparison of the enthalpy from density functional theory (DFT) calculations confirms this ordering in stability. The difference in enthalpy is $2meV$ per MAPI unit compared to the most stable tetragonal phase, yet $90meV$ compared to the high-temperature cubic phase [19]. Initial analysis of diffraction data assigned the $Pna2_1$ space group [16], [15]. Recent analysis of higher quality powder neutron diffraction data reassigns it to $Pnma$ (a D_{2h} point group) [3]. The structure is $a\sqrt{2a} \times \sqrt{2a} \times \sqrt{2a}$ supercell expansion of the simple cubic perovskite lattice. In the $Pna2_1$ phase, the $\mathrm{PbI_6}$ octahedra are distorted and tilt as $a^+a^-a^-$ in Glazer notation [19] with re-

spect to the orientation of the conventional cubic cell. In this low-temperature phase, the four molecular cations in the unit cell are static on the diagonals of the ab planes pointing towards the undistorted facets of the cuboctahedral cavity. Correspondingly, molecules belonging to different planes are anti-aligned with a head-tail motif. Such an antiferroelectric alignment is expected from consideration of the molecular dipole-dipole interaction [20]. In the low-temperature orthorhombic phase, the $CH_3NH_3{}^+$ sublattice is fully ordered (a low entropy state). The ordering may be sensitive to the material preparation and/or cooling rate into this phase, $i.e.$ the degree of quasi-thermal equilibrium. It is possible that different ordering might be frozen into the low-temperature phase by mechanical strain or electric fields.

1.4 Crystal of Perovskite $CH_3NH_3PbI_3$

We determined the crystal structure of $CH_3NH_3PbI_3$ first, which varies under different temperatures. Stoumpos $etal$, report the crystal is tetragonal $P4mm$ at 400K, tetragonal I4cm at 293K, and a low-symmetry supercell at temperature below $\sim$ 130K. Brivio et al [17, 19]. Claim that cubic $Pm\bar{3}m$, tetragonal $I4/mcm$, and orthorhombic $Pnam$ crystal structures were detected through X-ray diffraction in high quality $CH_3NH_3PbI_3$ crystals. The improved symmetry at the higher temperature is experimentally proposed to be related to the fast dynamic movement of $(CH_3NH_3)^+$ cations within the $Pb-I$ framework. As a result, the location of $(CH_3NH_3)^+$ cations can only be determined experimentally in the orthorhombic phase at low temperature. At the same time, the lattice constants of the orthorhombic crystal vary little at the low temperature [21]. Therefore, this investigation is focused on the orthorhombic perovskite $CH_3NH_3PbI_3$.

Both structural and electronic properties of organic–inorganic hybrid perovskite $CH_3NH_3PbI_3$

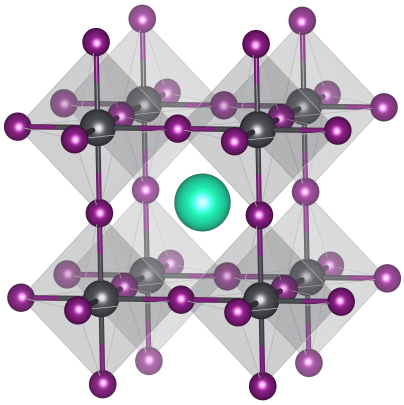

Figure 1.6: Illustration of the perovskite structure based on corner sharing octahedra of BX6 with either a monovalent metal (inorganic) or charged molecule (hybrid) at the centre of the unit cell. For hybrids, there is an orientation dependence on the central cation .

crystals are investigated in the present ab initio calculations. Density functional theory (DFT) is employed as it offers an efficient, yet accurate quantum mechanical method for theorists to optimize structures, determine energies of reactants and products, examine the nature of intermediates, and predict the reaction energies for elementary steps.

Perovskite structure was confirmed by X-ray diffraction, [22] and $CH_3NH_3PbI_3$ shows a orthorhombic phase with lattice parameters [23]

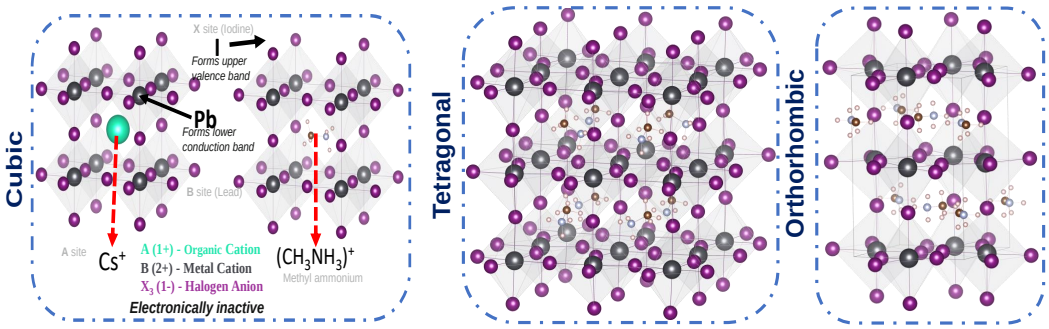

Figure 1.7: The crystal structure of the orthorhombic $CH_3NH_3PbI_3$ with a space group Pnma. The unit cell enclosed by the box consists of two stacked cells in the b direction due to the opposite dipoles of the $(CH_3NH_3)^+$ cations. (b) Each Pb^{2+} cation (Pb6c) is coordinated to $(I)^-$ anions (I2c), forming a [PbI-6] octahedron. (c) Each $(CH_3NH_3)^+$ cation is located in the center of a distorted cubooctahedral pocket with twelve $(I)^-$ anions at the vertices, enclosed by eight corner-connected [PbI-6] octahedra. Green, I; DodgerBlue1, Pb; Dark Purple, N; Yellow, C; Pink, H.

Parameter	a (Å)	b(Å)	c (Å)	v(Å)^3	α	β	γ
Orthorhombic	8.861	12.659	8.581	962.54	90	90	90
Tetragonal	8.810	8.810	12.710	962.54	90	90	90
Cubic	6.320	6.320	6.320	962.54	90	90	90

Table 1.2: The lattice constants and the volume of orthorhombic, tetragonal, and cubic $CH_3NH_3PbI_3$ from powder neutron diffraction (PND) at 100 K, 180 k, and 352 K respectively .

Perovskite challenge and perspectives

Hybrid halide perovskite photovoltaics and photocatalysis

In 1839. a German mineralogist named Gustav Rose discovered the perovskite structure $CaTiO_3$ in the Ural Mountains. The crystal structure is shown in Figure 1.6. The general

formula of this compound is ABX_3. Ca atom occupies the body center (A site) of perovskite structure, Ti atoms are located at each corner (B site), and O atoms stay in the middle of each bond (X site). The ion radius on A site is usually larger than the one on B site. The unit cell of an ideal perovskite structure consists of corner-sharing BX_6 octahedra and A is occupied cuboctahedral in the center. Over a century later of finding the natural perovskite $CaTiO_3$. Weber44 first synthesized hybrid halide perovskite in 1978. The crystal structures of hybrid halide organic-inorganic perovskite are originated from the mineral $CaTiO_3$. A large monovalent organic methylammonimn (CH_3NH_3) cation was located at the A site, a lead atom possesses B site of the structure and halide atoms are located at the X sites between two adjacent lead atoms. The structure is illustrated in Fig. 1.7. Early research of the hybrid perovskites was focused on the potential of superconductor [24], carrier transport as semiconducting channels [25], etc. Until 2009, the first hybrid halide perovskite solar cell was fabricated as a form of dye-sensitized solar cell with a power conversion efficiency (PCE) of 3.81% by Tsutomu Miyasaka [26]. Tsutomu Miyasaka used hybrid halide perovskite as the dye absorbed on mesoscopic TiO_2- However, the first version of the perovskite solar cell was quite unstable. The halide electrolyte will erode the perovskite active layer within a few minutes. A breakthrough came three years later: instead of iodine/iodide redox electrolyte, using a solid-state spiro-OMeTAD as the hole transporter largely increases the stability of hybrid halide perovskite solar cell with a PCE larger than 9% [27–29]. In 2013, Burschka et al. [30] utilized a novel sequential deposition method and made a planar cell structure rather than the previous mesoporous scaffold perovskite, with a PCE about 15%. Introducing another promising formamidinium cation into current methylammonium lead halide perovskite improved the crystallization properties of the perovskite thin film and boosted the PCE to 20.2%. In 2016, Saliba et al. [31] obtained a more stable perovskite solar cell when adding a third type of cation Cs into the perovskite alloy with a PCE of 21.1%. The best

research-cell efficiencies chart from the National Renewable Energy' Laboratory records the development of different photovoltaic technologies have from 1975 to nowadays, shown in Figure 1.6. The chart clearly shows that the dramatic increase of PCE for perovskite-based photovoltaics compared with other emerging photovoltaic technologies. It is certified that the latest world record PCE of perovskite photovoltaics has roared up to 25.2% which have already competed for the thin-film polycrystalline silicon photovoltaics(21.2%). Except for the high PCE of perovskite solar cells, the intrinsic softness of hybrid halide perovskite [25] makes the procedure of cell module fabrication printable [32]. These printable technologies will largely diminish the drawbacks mentioned previously of traditional solar cells. Organic–inorganic metal halide perovskites (HPs) have risen to prominence as cutting-edge materials for optoelectronic and energy applications. In addition to numerous well-known

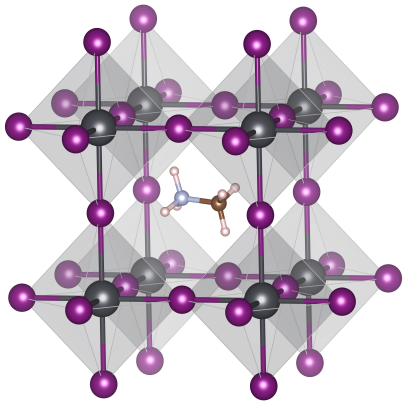

Figure 1.8: The crystal structure of CH3NH3PbI3: the C atom is colored brown, the N atom is colored cyan, the H atom is colored light pink, all are in the center of the octahedron, and the Pb atom is colored black, surrounded by the purple I atom. .

applications, such as solar cells, light-emitting diodes, photodetectors, and resistive switching memories, HPs can be used as efficient photocatalysts for a variety of electrochemical reactions, such as carbon dioxide (CO_2) reduction reactions, hydrogen evolution reaction,

photosynthesis, and wastewater treatment. Due to their low stability in polar solvents, however, the employment of HPs in photo-driven catalysis remains a formidable obstacle. The performance of HPs as efficient photocatalysts in a wide variety of applications, however, has made significant strides towards overcoming this crucial obstacle. This examination begins with a discussion of the structures and properties of HPs. Next, we will discuss the most modern methods for fabricating HPs, including thin films and nanostructures. Strategies for applying HPs in catalysis systems are exhaustively summarized and their functioning mechanisms are examined. Finally, the present obstacles and future potential of the application of HPs to photocatalytic reactions are thoroughly discussed.

1.5 Development of Hybrid Perovskite

The history of hybrid perovskite spans over a century, but they became one topic material since employed in photovoltaic from 2012. The last years of development have been intense with counter-intuitive results and contradictory reports. Hereby we report a brief overview of the perovskite development milestones. The first type of hybrid perovskite has been reported at the beginning of the century and, an initial characterization is reported in the literature.102 The materials have been almost entirely ignored for decades, with a few exceptions.102–107 Mitzi et al. investigated hybrid perovskites for their semiconductor properties and employed them in LED and electronic devices. Other consequent studies arrived in 1990s when Onada et al.108,109 performed a thermodynamic analysis of the material suggesting some structural phases for $MAPbX_3$. Applications in the photovoltaic area emerged from the contribution of the dye sensitized solar cell (DSSC). One major area of research in this field was the assembly of a fully solid state device to eliminate the leakage due to the liquid electrolyte. This

involved the development of new hole transport materials and new dyes that were compatible to build a solar cell. The first cell substituted the liquid electrolyte with spiro-OMeTAD, but the efficiency was still lower than correspondent standard solid-state devices. The evolution of solid-state cells included quantum dots as sensitizers. Due to quantum confinement effects, there is an absorption enhancement of radiation in the visible part of electromagnetic spectra. The first reported hybrid perovskite-based solar cell occurred in 2009-110 when quantum dots of $MAPbI_3$ and $MAPbBr_3$ have been deposited on a mesoporous titanium layer. The efficiency of these cells was as low as below 4%, but the photovoltage of 0.96 V was encouraging. Similar cells have been built with Sb_2S_3 quantum dots, but the efficiency was not significant. In the years that followed, hybrid perovskites were the focus of structural and optical studies, materials for solar cell interfaces, and tunable semiconductors. The second attempt to deploy $MAPbI_3$ quantum-dot-sensitized solar cells resulted in a photovoltaic conversion enhancement of up to 6.54 percent. Different research groups utilized hybrid perovskite or similar materials in solar cells with distinct topologies as a result of this study. This considerable interest was warranted by the possibility of building new solid-state solar cells to improve the DSSC, whose instability was mostly attributable to the presence of liquid electrolyte. The first wave of research was primarily device-driven, with new efficiency records being set almost with each new use of the material. This remarkable achievement was made possible since the design of hybrid perovskite solar cells incorporated the DSSC methodologies and know-how acquired over the past few decades. The breakthrough in the field happened when Snaith's team achieved a 10.9% power conversion efficiency. On top of an aluminium dioxide (Al_2O_3) framework, perovskite was placed to distinguish this accomplishment. All previous devices were based on the assumption that the mechanism behind the cell was similar to that observed in DSSC. The perovskite was believed to be responsible for the generation of electron-hole pairs upon light absorption, followed by the injection of

electrons into the titanium oxide layer.

If TiO_2 is replaced with Al_2O_3, there will be a misalignment of energy levels between the hybrid material and the semiconductor, making charge injection impossible if the DSSC mechanism is utilized. This proved that such cells function, or can function, by a mechanism substantially distinct from that of a DSSC, with the perovskite being able to create the electron-hole pair and transport it. This discovery multiplied the scope of perovskite's application in solar cells. Specifically, the research focuses on mesoscopic semiconductor solar cells, thin film solar cells, and p-n heterojunction cells. Snaith provided a panorama of current technology and future improvements in solar cells, ranging from DSSC to various hybrid perovskite structures, as depicted in Fig. 1.9 The composition of the most efficient solar cells is a mixture of halides and a mesoscopic architecture. Even while productivity has increased dramatically over the past three years and the subject is oversaturated with papers, a clear, comprehensive understanding of the material's behavior is lacking.

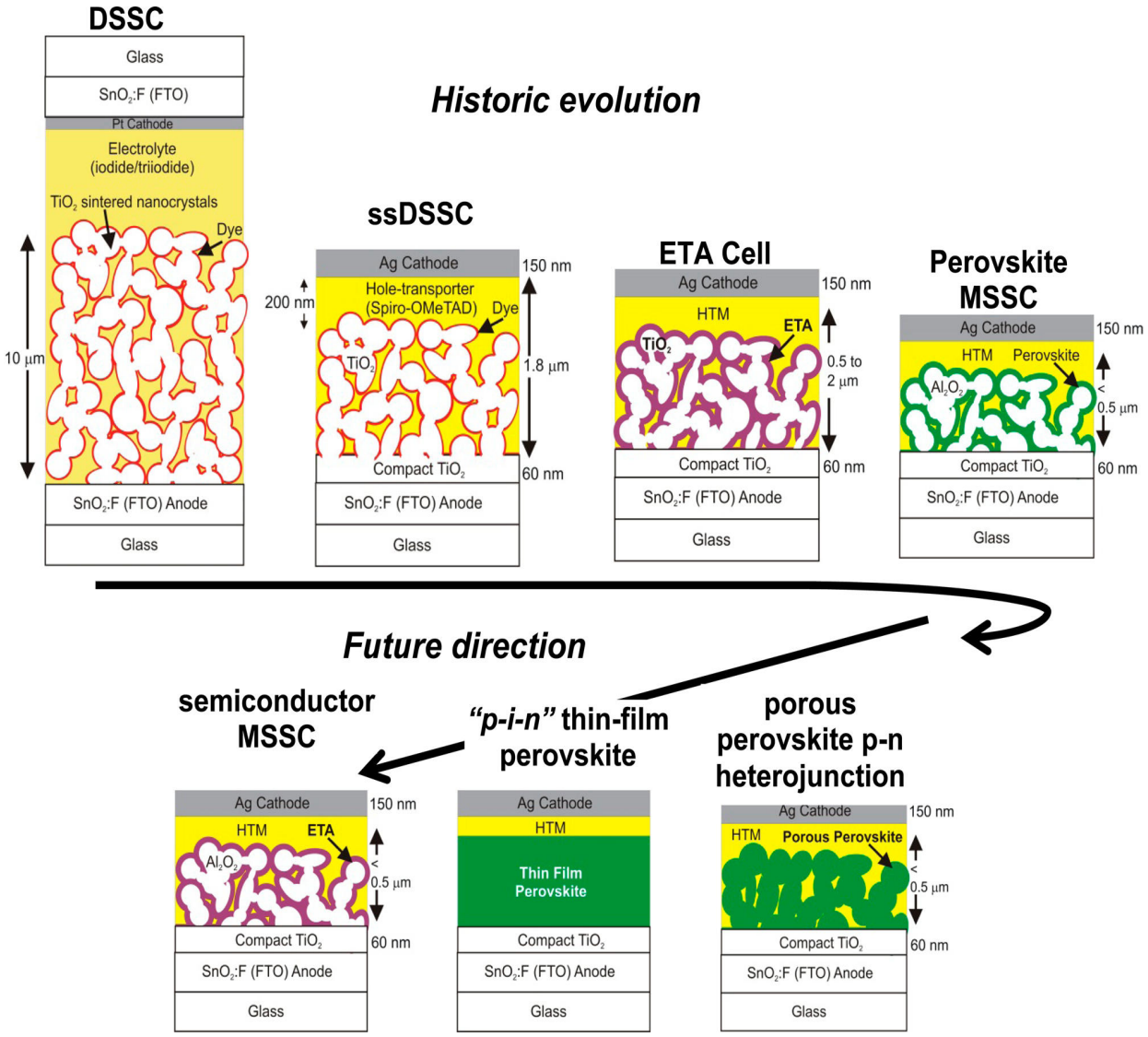

Figure 1.9: Schematic of the evolution from DSSC toward different designs of hybrid perovskite solar cells. The first row reports in order the evolution from regular DSSC to mesoporous perovskite solar cells. The cartoons reports: DSSC with liquid electrolyte, solid-state DSSC, extremely thin absorber (ETA) solar cell, and mesoporous solar cell, where the perovskite is adsorbed on an alumina scaffolding. The second row reports future development at the time. From left to right: semiconductor mesoporous solar cells, "p-i-n" solar cell (a p-n junction with an insulator layer at the interface, and porous perovskite heterojunction [4].

CHAPTER 2

Theory and Computational Methods

In this chapter, we concentrate on the underlying theory and theoretical simulation techniques applied in projects. Firstly, the quantum-chemical theories, especially density functional theory (DFT) and molecular dynamic (MD), are introduced with their history and development. The main approaches of DFT are discussed to explain how to make our model simple and calculation efficient. The supercell approach and k-points sampling are introduced as good approximations, which help us to establish the solid surface model. Secondly, other approximations, such as pseudopotential approximation and the projector augmented wave (PAW) method, are also described in this chapter, which helps to choose a better method before simulations. In the third part, ab initio MD and other advanced MD approaches, such as umbrella sampling approaches, slow-growth methods and constrained molecular dynamics (CMD), are presented withtheir advantages and disadvantages mentioned. In the final section, several technique issues of simulations are discussed.

2.1 Early Theories of Quantum Chemistry

From the microscopic point of view, a solid state can be seen as a collection of heavy, positively charged nuclei (n) and lighter, negatively charged electrons (e). The nuclei and electrons are treated as electromagnetically interacting point charges and the exact non-relativistic many-body Hamiltonian for this system becomes:

$$\widehat{H}_{Total} = \widehat{T}_N + \widehat{T} + \widehat{V}_{ext} + \widehat{V} + \widehat{V}_{NN} \tag{2.1}$$

$\widehat{T}_N = -\frac{\hbar^2}{2}\sum_i \frac{\nabla^2_{\vec{R}_i}}{M_i}$ *kinetic energy of the nucleus*

$\widehat{T} \ = -\frac{\hbar^2}{2}\sum_i \frac{\nabla^2_{\vec{r}_i}}{m_e}$ *kinetic energy of the electrons*

$\widehat{V}_{ext} = -\frac{1}{4\pi\varepsilon_0}\sum_{i,j} \frac{e^2 Z_i}{|\vec{R}_i - \vec{r}_j|}$ *the electron-nucleus interaction*

$\widehat{V} \ = -\frac{1}{8\pi\varepsilon_0}\sum_{i\neq j} \frac{e^2}{|\vec{r}_i - \vec{r}_j|}$ *the electron-electron interaction*

$\widehat{V}_{NN} = -\frac{1}{8\pi\varepsilon_0}\sum_{i\neq j} \frac{e^2 Z_i Z_j}{|\vec{R}_i - \vec{R}_j|}$ *the nucleus-nucleus interaction*

M_i is the mass of the nucleus at R_i. The electrons have mass m_e and are positioned at r_i. The first and second term correspond to the kinetic energy operator of the nuclei and of the electrons respectively. The remaining terms describe the Coulomb interaction between electrons and nuclei, among electrons and among nuclei respectively. To know the state (wave functions $\Psi(\vec{R}, \vec{r})$, with $\vec{R} = \vec{R}_i | i = 1, ..., N_n$ and $\vec{r} = \vec{r}_i | i = 1, ..., N_e$) of this system the corresponding Schrödinger equation has to be solved:

$$\widehat{H}\Psi(\vec{R}, \vec{r}) = E\Psi(\vec{R}, \vec{r}) \tag{2.2}$$

Unfortunately, due to the high degree of complexity it is impossible to solve this equation without introducing some approximations.

2.1.1 The Schrödinger equation

2.1.1.1 Basic knowledge

In this part, we consider the $\mathbb{R}^3 \times \mathbb{R}^+$ space, i.e. the three coordinates of space, and time. We denote by $\mathbf{q}$ the coordinates of a quantum system. $\mathbf{q}$ belongs to a space called the configuration space, composed of the spatial and temporal coordinates of the A nuclei and N electrons of the system ($\mathbb{R}^{3(K+N)} \times \mathbb{R}^+$). The state of a system is completely determined by its $\bar{\Psi}$ wave function, with values in $\mathbb{C}$ [33]. By definition, the data of this function, at a given time, not only describes all the properties of the system at this moment, but also determines its behavior in all subsequent states. Mathematically, this translates into the fact that the value of the derivative $\frac{\partial}{\partial t}\bar{\Psi}$ of the wave function with respect to time must, at every moment, be determined by the value of the wave function $\bar{\Psi}$ itself at this instant. In the most general form, the Schrodinger equation, which describes the evolution of the function is given by [34]:

$$i\hbar\frac{\partial}{\partial t}\bar{\Psi} = \mathcal{H}\bar{\Psi} \tag{2.3}$$

where the Hamiltonian $\mathcal{H}$ is an hermitian linear operator, independent of time, $\hbar = \frac{h}{2\pi}$, h being the Planck constant ($h = 6.6260610^{-34}m^2kgs^{-1}$). At the stationary state the energy of the system is constant over time. Thus, the Schrodinger equation that depends on the time may be reduced to stationnary state Schrondinger equation:

$$\mathcal{H}\bar{\Psi}_n = \varepsilon_n\bar{\Psi}_n \tag{2.4}$$

ϵ_n being the eigenvalue or energy associated with the steady state $\bar{\Psi}_n$. It's an eigenvalue equation where the eigenvalue of the Hamiltonian en is none other than the energy associated to the steady state psin that is independent of time. For many body systems, the information

of all particles is contained in the wave function. Thus, the Schrodinger equation becomes complicated to solve in its standard form. In what follows, we will present the theory and the different approximations that simplify the problem. Considering a system of A nuclei and N electrons,the stationary state $|\Psi\rangle$ of this system can be described by a wave function:

$$\Psi\left(R_I, \vec{r_i}\right) = \left\langle \vec{R}_I, \vec{r_i} | \Psi \right\rangle = \Psi\left(\vec{R}_1, \vec{R}_2, \ldots, \vec{R}_N, \vec{r}_1, \vec{r}_2, \ldots, \vec{r}_n\right), \tag{2.5}$$

satisfying the equation of Schrödinger independent of the time [**?**]:

$$\widehat{\boldsymbol{H}}_{tot}\Psi\left(\vec{R}_I, \vec{r_i}\right) = E_{tot}\Psi\left(\vec{R}_I, \vec{r_i}\right) \tag{2.6}$$

where E_{tot} is the total energy of the system. The total Hamiltonian operator is given by:

$$\hat{H}_T = \hat{T}_n + \hat{T}_e + \hat{V}_{ne} + \hat{V}_{ee} + \hat{V}_{nn} \tag{2.7}$$

The first terms $\hat{T}_n$ and $\hat{T}_e$ designate the kinetic energy of A nuclei and N electrons respectively. while the terms $\hat{V}_{n-e}$, $\hat{V}_{e-e}$, and $\hat{V}_{n-n}$ describe Colombian interaction electron-nuclei, electron-electron and nuclei-nuclei respectively. Its explicit expression can be written as follow:

$$\Psi = -\sum_{i}^{N}\frac{\hbar^2}{2m}\nabla_i^2 - \sum_{I}^{A}\frac{\hbar^2}{2M}\nabla_I^2 - \sum_{i,I}\frac{Z_I e^2}{\left|\vec{r_i} - \vec{R}_I\right|} + \sum_{i<j}\frac{e^2}{|\vec{r_i} - \vec{r_j}|} + \sum_{I<J}\frac{Z_I Z_J e^2}{\left|\vec{R}_I - \vec{R}_J\right|} \tag{2.8}$$

The first two terms of the Hamiltonian are the kinetic energy operators of N electrons (indexed i, j) and Atomic nuclei (indexed I, J) respectively. The other three terms represent the different electron-nucleus,electron-electron, and nucleus-nucleus interaction potentials. As an example of a many-body system, we may quote the case of a regular crystal. The electrons are not only affected by the nuclei in their lattice sites, but also by the other electrons. An exact solution of the Schrodinger equation is impossible in the case of poly-electronic systems. It is therefore necessary to implement simplifying procedures associated with some mathematical tricks in order to make possible the obtaining of an approximate solution.

2.1.1.2 The Born-Oppenheimer Approximation

The mass of the electrons is much smaller than the one of the nuclei while the electromagnetic forces acting on them are of comparable magnitude. Consequently, the electronic motion ($\approx 106m/s$) is considerably faster than the nuclear motion ($\approx 103m/s$). Because the nuclei move so slowly on the scale of velocities of relevance to the electrons, it is justified to assume that at any moment the electrons will be in their ground state with respect to the instantaneous nuclear configuration. The assumption of instantaneous electronic equilibrium for every nuclear configuration implies that the electron wave function is a solution of the Schrödinger equation for Hamiltonian 3.1 with fixed nuclear positions:

$$\widehat{H} = \underbrace{-\frac{\hbar^2}{2}\sum_i \frac{\nabla^2_{\vec{r_i}}}{m_e}}_{\widehat{T}} \underbrace{-\frac{1}{4\pi\varepsilon_0}\sum_{i,j}\frac{e^2 Z_i}{|\vec{R_i}-\vec{r_j}|}}_{\widehat{V}_{ext}} \underbrace{-\frac{1}{8\pi\varepsilon_0}\sum_{i\neq j}\frac{e^2}{|\vec{r_i}-\vec{r_j}|}}_{\widehat{V}} \underbrace{-\frac{1}{8\pi\varepsilon_0}\sum_{i\neq j}\frac{e^2 Z_i Z_j}{|\vec{R_i}-\vec{R_j}|}}_{\widehat{V}_{NN}} \tag{2.9}$$

This Hamiltonian corresponds to the electronic motion in the external potential produced by the nuclei. Important to note here is that the nuclear repulsion ($\widehat{V}_{NN}$) contributes to the total energy by augmenting it with a constant amount. As a consequence, removing this term from the hamiltonian will not affect the corresponding wave function. The resulting hamiltonian can be written as:

$$\widehat{H}_e = \underbrace{-\frac{\hbar^2}{2}\sum_i \frac{\nabla^2_{\vec{r_i}}}{m_e}}_{\widehat{T}} \underbrace{-\frac{1}{4\pi\varepsilon_0}\sum_{i,j}\frac{e^2 Z_i}{|\vec{R_i}-\vec{r_j}|}}_{\widehat{V}_{ext}} \underbrace{-\frac{1}{8\pi\varepsilon_0}\sum_{i\neq j}\frac{e^2}{|\vec{r_i}-\vec{r_j}|}}_{\widehat{V}} \tag{2.10}$$

$$\widehat{H} = \widehat{H}_e + \widehat{V}_{NN} \tag{2.11}$$

Equation 3.4 is called the electron Hamiltonian, $\widehat{T}$ represents the kinetic energy of the electrons, $\widehat{V}$ the electronic repulsion and $\widehat{V}_{ext}$ the electron-nucleus interaction. From now on, electrons and nuclei can be treated separately. This decoupling of the electronic and nuclear motion is known as the Born-Oppenheimer or adiabatic approximation [35].

2.1.1.3 One-electron approximation

The electronic wave function depends on the position of every single electron:

$$\psi = \psi(X_1, X_1, X_1.....X_N) \tag{2.12}$$

where X_i represents both the position and the spin of the i-electron. If the interaction between electrons, $\widehat{V}_{e-e}(\mathbf{r})$, is assumed constant, the Hamiltonian can be expressed as a sum of independent one-particle Hamiltonians, one for every single electron. Consequently, the electronic wave function can be further factorized:

$$\widehat{H}_e = \sum_{n=1}^{N} \widehat{h}_{e,i} \tag{2.13}$$

$$\psi_i(X_1, X_1, X_1.....X_N) = \prod_{n=1}^{N} \chi_i(X_i) \tag{2.14}$$

Equation 3.8 is called Hartree function, but it is not enough to describe a multielectron system. Electrons are Fermions and therefore are described by an antisymmetric wave function:

$$\psi_e(X_1, X_1, ..., X_i, X_j, ...X_N) = -\psi_e(X_1, X_1, ..., X_j, X_i, ...X_N) \tag{2.15}$$

To avoid this issue it is possible to build a specific function called Hartree-Fock equation or Slater determinant:

$$\psi_e(X_1, X_1, ..., X_i, X_j, ...X_N) = \frac{1}{\sqrt{N!}} \begin{vmatrix} \chi_1(X_1) & \chi_2(X_1) & .... & \chi_N(X_1) \\ \chi_1(X_2) & \chi_2(X_2) & .... & \chi_N(X_2) \\ : & : & \ddots & : \\ \chi_1(X_N) & \chi_2(X_N) & .... & \chi_N(X_N) \end{vmatrix} \tag{2.16}$$

Due to matrix determinant properties [36] the Slater determinant will respect prerequisite anti-symmetric property. The problem is then to reduce the resolution of the single electron wave functions. When all the solutions are computed, it is then possible to calculate the energy or other properties of the system [37].

2.1.1.4 Hartree-Fock method (HF)

The HF methods allows the calculation of the ground state of a system in an iterative way. In order to achieve this equation, 3.4 have to be rearranged in such a way to define a special operator called Fock operator. This new operator is defined using the function itself and for this reason, an iterative approach is needed to solve this equation. This particular iterative operation is called Self-Consistent Field (SCF) and if the energy is minimized it can be demonstrated that (ideally) it is possible to obtain convergence to the ground-state of a system. Nonetheless, it must be kept in mind that some approximations are present:

• Born-Oppenheimer approximation.

• no relativistic effects.

• mean and constant electron-electron interaction.

• omission f electronic correlation.

The HF method describes a single-determinant wave function. For this reason, it can not take in account the interaction between electrons with opposite spins, but it fully accounts for the exchange interaction that arises from the anti-symmetry of the wave function. Correlation and exchange are crucial aspects of related Density Functional Theory (DFT) calculations and we will discussed it in the next sections. The dimension of the system affects the complexity of the calculation which becomes impracticable for large system. Formally the cost to solve the HF equations scales as the fourth power of the number of elements in the basis

set. The complexity for large systems can be reduced by a range of approximations and thus the actual scaling will be close to the square of the number of the basis set.128 This problem has been the starting point to develop methods that allowed the description of larger systems

2.1.1.5 The theorems of Hohenberg and Kohn

In 1964 Hohenberg and Kohn stated two theorems on which DFT has been built:

Theorem 1 *: There is a **one-to-one** correspondence between the ground state density $\rho(\vec{r})$ of a many-electron system (atom, molecule, solid) and the external potential V_{ext}. An immediate consequence is that the ground state expectation value of any observable$\vec{O}$ is a unique functional of the exact ground state electron density:*

$$\langle\Psi|\widehat{O}|\Psi\rangle = O[\rho] \tag{2.17}$$

Theorem 2 *: For $\widehat{O}$ being the Hamiltonian $\widehat{H}$, the ground state total energy functional $H[\rho] \equiv E_{v_{ext}}[\rho]$ is of the form*

$$E_{v_{ext}}[\rho] = \langle\Psi|\widehat{T} + \widehat{V}|\Psi\rangle + \langle\Psi|\widehat{V}_{ext}|\Psi\rangle \tag{2.18}$$

$$= \mathrm{F_{HK}}[\rho] + \int \rho(\vec{r})V_{ext}(\vec{r})d\vec{r} \tag{2.19}$$

where the Hohenberg-Kohn density functional $\mathrm{F_{HK}}[\rho]$ is universal for anynmany-electron system. $E_{Vext}[\rho]$ reaches its minimal value (equal to the ground state total energy) for the ground state density corresponding to V_{ext}

We will not prove the theorems here [1], but we will clarify their meaning. The **one-to-one** correspondence between the ground state density and the external potential has some

important implications. It is obvious that, given the external potential of the system, it is possible to find a unique ground state density for the system. Solving the Schr¨odinger equation yields the ground state wave function out of which the ground state density can be calculated. Intuitively, the ground state density seems to contain less information than the ground state wave function. If this were true, the inverse correspondence (from ground state density to external potential) would not hold. The first theorem of Hohenberg and Kohn, however, states that this correspondence holds as well. In other words: the density contains as much information as the wave function. As a consequence of the second theorem, and more precisely of the fact that the ground state density minimizes $E_{Vext}[\rho]$, the Rayleigh-Ritz variational method can be used to obtain the ground state density. Important to note is that $E_{Vext}[\rho]$ evaluated for the ground state density corresponding to Vext equals the ground state energy. Only this value of $E_{Vext}[\rho]$ has a physical meaning. And finally, in the second theorem the Hohenberg-Kohn-functional $\mathrm{F_{HK}}$ contains no information on the nuclei and the nuclear positions. Consequently, the functional is the same for all many-electron systems (universal). Unfortunately $\mathrm{F_{HK}}$ is not known and, at this level, the DFT remains a formally exact but useless theory. The second term in equation 3.8 is trivial.

2.1.2 Density Functional Theory

In the HF approach the dimension of the system directly affects the number of variables, i.e. electrons coordinates, needed to describe properly the system. Hohenberg and Kohn in 1964 and 1965 [38, 39], demonstrated two theorems that allowed the replacement of the HF function and its large number of the variables, with a single function that depends only on the three spacial coordinates $(n(x; y; z))$. The two theorems stated that:

◦ The ground state of a multi electronic system is a functional4 of the electronic density $n(\mathbf{r})$.

∘ This functional exists and it is unique (universal functional)

It follows then:

$$E_0 = E_0[n(\mathbf{R})] \tag{2.20}$$

It is possible to decompose the total energy into different parts. This operation is similar to what can be done in the HF method and, for this reason, it had been previously omitted. In 1965, in fact, the work of Kohn and Sham proved that the ground-state energy could be rewritten as:

$$E_0 = E_T + E_V[n] + E_j[n] + E_{XC}[n] \tag{2.21}$$

where

$$E_T = 2\sum_i^n \int_{vol} \chi_i^*(j)[-\frac{1}{2}\sum \bigtriangledown_j^2]\chi_i(j)d\tau_j \tag{2.22}$$

represents the Kinetic energy of the electrons. $d\tau_j$ is the infinitesimal volume occupied by the j electron for all the considered χ_i orbitals.

$$E_V = -\sum_\alpha^n \int_{vol} \frac{Z_\alpha n(\mathbf{r}_j)}{|\mathbf{R}_\alpha - \mathbf{r}_j|} d\tau_j \tag{2.23}$$

is the electron-nuclei interaction potential,

$$E_j = \sum_\alpha^n \int_{vol} \frac{n(\mathbf{r}_i)n(\mathbf{r}_j)}{|\mathbf{r}_i - \mathbf{r}_j|} d\tau_i d\tau_j \tag{2.24}$$

is the term related to the Coulomb electron-electron interaction. The first three terms are the quantum correspondent to the classic mechanics quantities. The last term, $E_{XC}[n]$, on the other hand, is a peculiar quantity present only in a quantum interpretation of reality and it is impossible to describe it with a classic-physics analogy. This quantity takes into account the interaction between two electrons in the same spacial position with the same spin (*exchange*), and also with opposite spins (*correlation*). This interaction arises from the anti-symmetry of the wave-function and is a purely quantum effect. Even if, in principle, the problem is reduced to find a 3-variable function, operatively this is not possible. It is necessary to

decompose the whole density in a sum of single-electronic contributions as in the HF theory. Since the density of a function is the square module of the wave-function, this can be written as:

$$n(\mathbf{r}) = |\Psi(x)|^2 = 2\sum_{i}^{n} |\chi_i(\mathbf{r})|^2 \tag{2.25}$$

where the factor of 2 takes into account the spin degeneracy and the $\chi_i(\mathbf{r})$ functions, which are known as the Kohn-Sham orbitals and are solutions of the following equation :

$$F_{KS}(i)\chi_i(i) = \epsilon_{i,KS}\chi_i(i) \tag{2.26}$$

where

$$F_{KS} = -\frac{1}{2}\bigtriangledown_i^2 - \sum_{\alpha}\frac{Z_\alpha}{|\mathbf{R}_\alpha - \mathbf{r}_i|} + \int_{vol}\frac{n(\mathbf{r}_i)}{|\mathbf{r}_i - \mathbf{r}_j|}d\tau_i + V_{XC}(i) \tag{2.27}$$

and it is called the Kohn-Sham operator. It is important to underline how the Kohn-Sham orbitals are a purely mathematical object and they do not have necessarily any physical meaning, if not to reproduce the total charge density. Differently from HF, DFT includes both the correlation and the exchange effects. They are described in 3.28 by the $V_{XC}(i)$ term, which is the exchange-correlation potential, and of which the exact form is not explicitly known:

$$V_{XC} = \frac{\partial E_{XC}[n]}{\partial n} \tag{2.28}$$

Therefore to solve the problem it is necessary to define a V_{XC} that effectively approximates the real potential. Once the exchange-correlation potential is defined, equation 3.27 is solved using some trial Kohn-Sham orbitals which, accordingly to 3.26, determine the initial electronic density. Since the density appears also in the operator, a SCF approach is needed. However, there are some differences with the HF method. In fact, as previously said, the Kohn-Sham orbitals don't necessarily have a physical meaning and the self-consistent procedure returns only the electronic density, and no direct information on the wave-function is provided. Besides it must be pointed out that since the V_{XC} is not exactly known, the DFT

energy can not be considered an upper bound of the true value.131,132 This implies that contrary to the HF, the SCF procedure can not be improved in a consistent manner.

2.1.2.1 The Kohn-Sham equations

An important step towards applicability of DFT has been made by Kohn and Sham [2]. They proposed to rewrite $\mathrm{F_{HK}}$ as follows:

$$\mathrm{F_{HK}}[\rho] = T_0[\rho] + V_H[\rho] + \underbrace{(V_x[\rho] + V_c[\rho])}_{V_{xc}[\rho]} \tag{2.29}$$

where $T_0[\rho]$ is the kinetic energy functional for noninteracting electrons and $V_H[\rho]$is the Hartree contribution, which describes the interaction with the field obtained by averaging over the positions of the remaining electrons. Although no on-site electron-electron interaction is taken into account, $V_H[\rho]$ is already a good approximation for the electron interaction. Assuming we know the exchange-correlation functional $V_{xc}[\rho]$, we can now write:

$$E_{V_{ext}}[\rho] = T_0[\rho] + V_H[\rho] + V_{xc}[\rho] + V_{ext}[\rho] \tag{2.30}$$

Equation 3.10 can be interpreted as the energy functional of noninteracting particles submitted to two external potentials $V_{ext}[\rho]$ and $V_{xc}[\rho]$, with corresponding Kohn-Sham Hamiltonian:

$$\widehat{H}_{KH} = \widehat{T}_0 + \widehat{V}_H + \widehat{V}_{xc} + \widehat{V}_{ext} \tag{2.31}$$

$$= -\frac{\hbar^2}{2m_e}\nabla_i^2 + \frac{e^2}{4\pi\varepsilon_0}\int \frac{\rho(\vec{r})}{|\vec{r} - \vec{r'}|} + \widehat{V}_{xc} + \widehat{V}_{ext} \tag{2.32}$$

with the exchange-correlation operator given by the functional derivative:

$$\widehat{V}_{xc} = \frac{\partial V_{xc}[\rho]}{\partial \rho} \tag{2.33}$$

The Kohn-Sham theorem can now be stated as follows:

The exact ground state density $\rho(\vec{r})$of an N-electron system is

$$\rho(\vec{r}) = \sum_{i=1}^{N} \psi_i^* \psi_i(\vec{r}) \tag{2.34}$$

where the single-particle wave functions $\psi_i(\vec{r})$ are the N lowest-energy solutions of the Kohn-Sham equation

$$\widehat{H}_{KS}\psi = \epsilon_i \psi_i \tag{2.35}$$

To obtain the ground state density of the many-body system the Schroedinger single-particle equation must be solved. The only unknown contributor to this problem is the exchange-correlation functional. Available approximations for this functional will be treated in the next section.

Two additional remarks have to be made. First, one has to realize that the single-particle wave functions $\psi_i(\vec{r})$ as well as the single-particle energies ϵ_i are no electron wave functions or electron energies. They are merely mathematical functions without a physical meaning. Only the total ground state density calculated from these "quasi-particles" equals the true ground state density. And second, the Kohn-Sham Hamiltonian depends on the electron density through the Hartree and the exchange-correlation term, while the electron density depends on the ψ_i to be calculated. This means that we are actually dealing with a self-consistency problem: the solutions determine the original equation. An iterative procedure is thus needed to solve the problem. In the first iteration a pondered guess is made for the starting density. The latter allows for the construction of the initial Kohn-Sham Hamiltonian. Solving the equation results in a new set of ψ_i and a new electron density. The new density will differ strongly from the previous one. With this density a new $\widehat{H}_{KS}$ can be produced etc. In the end succeeding densities will converge, as will the Hamiltonians. A solution consistent with the Hamiltonian has been reached.

The Kohn-Sham equation proves to be a practical tool to solve many-body problems.

2.1.2.2 The exchange-correlation functional

The third term in the effective potential (2.63) is the $exchange - correlation$ potential. This is of central importance in the accuracy of DFT calculations, and there has been much work finding accurate forms of v_{xc} [5].

2.1.2.3 Local Density Approximation LDA

The simplest approximation is to assume that the density can be treated locally as an uniform electron gas; the exchange correlation energy at each point in the system is the same as that of an uniform electron gas of the same density. This approximation was originally introduced by Kohn and Sham [22]. and holds for a slowly varying density. Using this approximation the exchange-correlation energy for a density $\rho(\mathbf{r})$ is given by ,

$$E_{xc}^{LDA} = \int \rho(\mathbf{r})\epsilon_x c\rho(\mathbf{r})d\mathbf{r} \tag{2.36}$$

$$v_{eff}(\mathbf{r}) = v(\mathbf{r}) + \int \frac{\rho(\mathbf{r}')}{|\mathbf{r} - \mathbf{r}'|}d\mathbf{r}' + v_{xc}(\mathbf{r}), \tag{2.37}$$

where $v_{xc}(\mathbf{r})$ is the exchange-correlation potential given by

$$v_{xc}(\mathbf{r}) = \frac{\delta E_{xc}}{\delta\rho(\mathbf{r})}. \tag{2.38}$$

where $\epsilon_{xc}(\rho)$ is the exchange-correlation energy per particle of an uniform electron gas of density ρ. The exchange-correlation potential is then given by [40] This can then be inserted

into (2.38) for use in calculations.

$$v_{xc}^{LDA}[\rho(\mathbf{r})] = \frac{\delta E_{xc}^{LDA}}{\delta\rho(\mathbf{r})} = \epsilon_{xc}(\rho) + \rho(\mathbf{r})\frac{\partial\epsilon_{xc}(\rho)}{\partial\rho}.$$

For practical use of the LDA in calculations it is necessary to determine the exchange-correlation energy for an uniform electron gas of a given density. It is common to split $\epsilon_{xc}(\rho)$ into exchange and correlation potentials $\epsilon_{xc}(\rho) = \epsilon_x(\rho) + \epsilon_c(\rho)$. The exchange potential is given by the Dirac functional [5]

$$\epsilon_x[\rho(\mathbf{r})] = -\frac{3}{4}\left(\frac{3}{\pi}\right)^{\frac{1}{3}}\rho(\mathbf{r}).$$

Accurate values for $\epsilon_c(\rho)$ have been determined from Quantum Monte Carlo (QMC) calculations [41]. These have then been interpolated to provide an analytic form for $\epsilon_c(\rho)$ [42]

2.1.2.4 Generalized Gradient Approximations GGA

As the LDA approximates the energy of the true density by the energy of a local constant density, it fails in situations where the density undergoes rapid changes such as in molecules. An improvement to this can be made by considering the gradient of the electron density, the so-called Generalized Gradient Approximation (GGA). Symbolically this can be written as

$$E_{xc} = E_{xc}[\rho(\mathbf{r}), \nabla\rho(\mathbf{r})].$$

This can lead to a large improvement over LDA results with accuracy approaching that of correlated wavefunction methods such as MP2 and in some cases surpassing these [43].

While there is only one LDA there are several different parameterizations of the GGA.

Some of these are semi-empirical, in that experimental data (e.g. atomization energies) is used in their derivation. Others are found entirely from first principles. A commonly used functional is the PW91 functional, due to Perdew and Yang [44, 45].

2.1.2.5 van der Waals

Van der Waals forces are driven by induced electrical interactions between two or more atoms or molecules that are very close to each other. Van der Waals interaction is the weakest of all intermolecular attractions between molecules. However, with a lot of Van der Waals forces interacting between two objects, the interaction can be very strong. Density functional theory (DFT) for molecules and materials is widely applied with approximate local and semi-local density functionals for the interaction effects. For largely homogeneous systems, for example, simple metals and semiconductors, the local-density approximation (LDA) for these effects is appropriate. For inhomogeneous systems, for example, transition metals, ionic crystals, compound metals, surfaces, interfaces, and some chemical systems, semi-local-density approximations, such as members of the family of generalized gradient approximations (GGA), work well. Today DFT describes cohesion, bonds, structures, and other properties very well for dense molecules and materials, as shown by recent studies for both single molecules [46] and dense solid-state [47] systems. However, sparse systems, including soft matter, van der Waals complexes, and biomolecules, are at least as abundant. They have inter particle separations, for which nonlocal, long-ranged interactions, such as van der Waals (vdW) forces, are influential. The aim of this Letter is to develop and apply a van der Waals density functional (vdW-DF) for general geometries to supplement the planar vdW-DF that we recently, applied with some success [48] to several layered materials.

We considered various approximations to the exchange andcorrelation functionals. Initially,

we tested two functionals constructed in the generalized gradient approximation (GGA): the Perdew, Burke, and Ernzerhof (PBE) [37, 48] and its revised version (revPBE). [37] These functionals differ only in one parameter of the exchange term, k, changed from 0.804 in PBE to 1.245 in revPBE, and both have been extensively applied in physics and chemistry. In a second step, we employed the vdW density functional (vdW-DF) by Dion et al., [37]

$$E_{xc}^{vdW-DF}[n] = E_{revPBE(x)}[n] + E_{LDA(c)}[n] + E_{nl(c)}[n] \tag{2.39}$$

where $E_{revPBE(x)}[n]$ is the exchange energy obtained with the revPBE functional, $E_{LDA(c)}[n]$ is an LDA correlation and $E_{nl(c)}[n]$ is a nonlocal correlation term that approximates the vdW interactions. We also considered the optimized Becke86 van der Waals (optB86b-vdW) functional introduced by$Klime\check{s}etal$

$$E_{xc}^{optB86b-vdw}[n] = E_{optB86b(x)}[n] + E_{LDA(c)}[n] + E_{nl(c)}[n] \tag{2.40}$$

where a reparametrized version of the Becke86 exchange functional replaces the revPBE exchange used in equation 2.39. Among the two functionals described in equations 2.39 and equation 2.40, the optB86b-vdW is generally more accurate, [49] and the results obtained with it should be preferred as reference.However, we apply the vdW-DF to analyze the effects of nonlocal correlation, since we can subtract the contributions of the other terms by introducing a revPBE+LDA functional,

$$E_{xc}^{optB86b-LDA}[n] = E_{revPBE(x)}[n] + E_{LDA(c)}[n] \tag{2.41}$$

which involves terms that have been tested and applied in a wide range of materials and whose behavior, in contrast to the exchange term in equation 2.40, is well-known.

2.1.2.6 Methods for electronic structure calculations

The Kohn-sham equation is solved self-consistent according to Figure 2.1. This figure includes the following steps:

1. The first step consists in choosing an initial density in $n(r)$ based on the eigen densities of the free atoms of the solid

2. We then calculate the effective Kohn-Sham potential using the density defined in first step.

3. We solve the Schrodinger equation in order to obtain the wave functions of the system.

4. We recalculate the density

In the next sections we will briefly discuss themost popular methods that are used to calculate the electronic structure of materials.

2.2 Crystal structure and Bloch Theorem

In the case of solids, the situation is more complicated than that of a single atom or molecule, because the properties of the solid can depend on a very large number of electrons, since there are a large number of atoms distributed in a macroscopic volume. For standard calculation methods, that would be a huge cost in time, even for powerful computers if we were to try to calculate the electronic structure of the whole system. In the case of crystal structures, this process is greatly simplified because the network is periodic. Since the same structure, or supercell is generally small, and has just repeated a large number of times, which allows

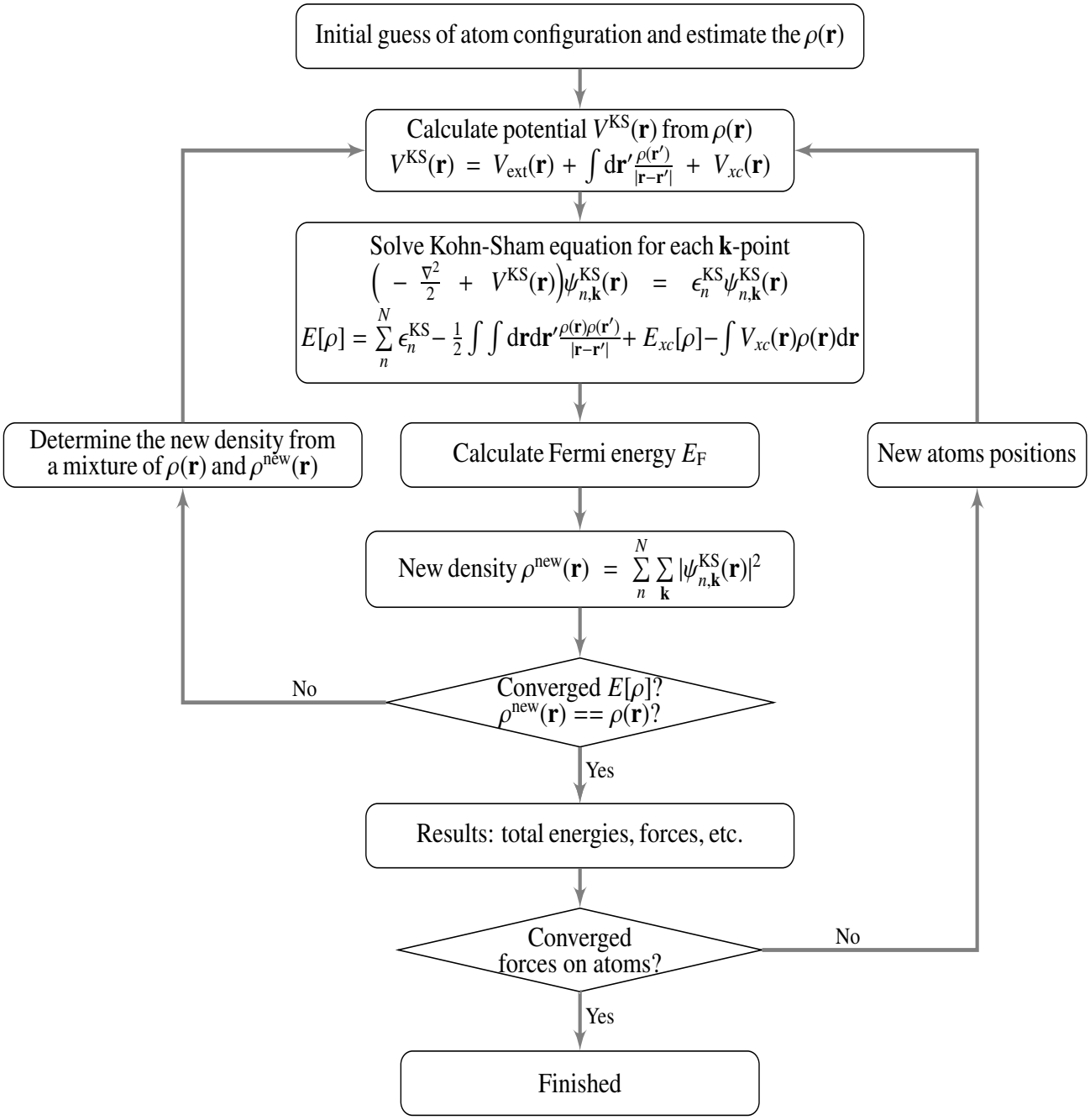

Figure 2.1: e-k relation of valence and conduction bands in an intrinsic semiconductor. Upward and right directions are taken as positive directions of the energy and wave vector in coordinates (A), whereas downward and left directions as positive directions in coordinates (B), respectively. Coordinates (A) arc used to describe the motion of an electron near the bottom of the conduction band. Coordinates (B) are used to describe that of a hole near the top of the valence band.

to consider just this cell for the purpose of calculations (something that cannot be done in a non-crystalline structure). This is done in the calculation using periodic boundary conditions, which comes from the cell which are repeated again and again in the simulation, just like in a real solid. Another theorem useful for these solid state calculations is called Bloch's theorem. A Bloch wave is defined as the wave function of a particle (in terms of interest here an electron) inside a periodic potential. The definition of this theorem is given below;

2.2.0.0.1 Bloch theorem : The proper function of such a system can be written as the product of a plane wave envelope function and a periodic function (of periodic function Bloch) $\mu_{nk}(r)$ which has the same periodicity as the potential:

$$\Psi_{nk}(r) = e^{ikr}\mu_{nk}(r) \tag{2.42}$$

The importance of this theorem is that the part of the envelope of the plane wave can be extended as a series of plane waves, allowing all functions of electrons to be expressed by plane-wave. It will become important and is discussed further in the following sections [50].

2.2.1 Plane-Waves

One of the most common methods for DFT when working in solids is the pseudopotential plane wave method [51]. It basically works out of a set of approximations and symmetries that work well in periodic boundary conditions of a crystal lattice. It is based on the theorem of Bloch identified as periodic boundary conditions as well as to create a set of basic wave plane. Returning to the previous section, it has shown that the electronic wave functions can be expressed as plane-waves. Another approximation, known as pseudopotential is also integrated to simplify the basic set plane wave and is discussed in the next section. The basis

of the theory is that it could go to infinity, that the great values of k will result in electrons with high kinetic energy. Since the DFT calculations are for the ground state, we can reasonably suppose that the wave functions of electrons can be given with a reduced basic set which will contain only the plane waves lower than the cutting energy (denoted E_{cut}). Basically after a certain value of k (denoted k_{cut}), the coefficients for the plane-waves will become very low, and can be overlooked because they are higher than the energy of electrons. However, we must be careful to choose the right value of the cut-off energy, because a too low a value can lead to inaccurate results.

2.2.2 Plane wave pseudopotential method

Plane waves offer a natural choice as a basis set to expand the periodic functions $u_{nk}(\mathrm{r})$ as:

$$u_{nk}(\mathrm{r}) = \sum_{\mathrm{G}} c_{\mathrm{nk,G}} e^{i\mathrm{G}\cdot\mathrm{r}} \tag{2.43}$$

where the summation is over all the reciprocal lattice vectors G of the system under study. Thus, the electronic wave functions can be written as:

$$\phi_{nk}(\mathrm{r}) = \sum_{G} c_{nk,G} e^{i(k+G)\cdot r} \tag{2.44}$$

The electronic wave functions at each k-point are now expressed in terms of a discrete plane wave basis set. In principle this Fourier series is infinite. However, in practice we cannot work with an infinite basis set, it has to be truncated. The number of plane waves can be restricted by placing an upper boundary to the kinetic energy of the plane waves. This boundary is called energy cut-off Ecut and only plane-waves satisfying the condition:

$$\frac{|\mathrm{k}+\mathrm{G}|^2}{2} < E_{\mathrm{cut}} \tag{2.45}$$

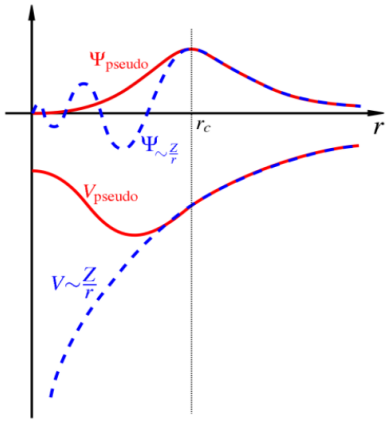

Figure 2.2: Schematic representation of pseudopotential and the pseudo wave function

are considered in the computation. With DFT, the complexity of the problem has reduced appreciably. However, for systems with a large number of electrons still remains computationally very expensive. Pseudopotentials helped in a crucial way to make the calculations tractable. Using the fact that the physical properties of solids depend mainly on valence electrons, the computational effort can be minimized considerably. In the pseudopotential approximation, the core electrons are removed and the strong ionic potential is replaced by the weaker pseudo potential V_{pseudo} that acts on a set of pseudo wave functions Ψ_{pseudo} rather than the true valence wave functions (Ψ). The pseudopotential and pseudo wave functions are generated in such a way that they are identical to the true potential and wave function beyond a certain radius known as cut-off radius r_c. In the core region the pseudo wave function is constructed such that all the nodes are removed but the norm is conserved. Also, since the nodes of the core states are removed, the number of plane-wave basis functions required to describe this wave function in the core region is much less resulting in reduced computational effort. This leads to a popular plane wave pseudopotential method for electronic structure calculations. In this thesis, we use this method to calculate the DFT band structure within the GGA approximation. These calculations are performed using the Quantum espresso code.

2.2.3 Projector augmented wave method (PAW)

An approach that lies half-way between the LAPW and the pseudopotential methods has been introduced by Bloch 2.2 known as the projector augmented waves (PAW) method. This approach retains the all-electron character, but it uses a decomposition of the all-electron wave function in terms of a smooth pseudo-wave function, and a rapidly varying contribution localized within the core region. The true and pseudo-wave functions are related by a linear transformation:

$$\left|\Psi_n^{AE}\right\rangle = \left|\Psi_n^{PS}\right\rangle + \sum_i \left(\left|\phi_i^{AE}\right\rangle - \left|\phi_i^{PS}\right\rangle\right) \left\langle p_i^{PS} \mid \Psi_n^{PS}\right\rangle \tag{2.46}$$

The pseudo-wave functions Ψ_n^{PS}, where n is the band index, are the variational quantities and are expanded in plane waves. In the regions between the PAW spheres surrounding the atoms, the Ψ^{PS}, n are identical to the all-electron wave functions Ψ_n^{AE} , but inside the spheres Ψ^{PS} are only a bad approximation to the exact wave functions, they are used only as a computational tool. The all-electron partial waves ϕ_i^{AE} are solutions of the spherical scalar-relativistic Schrödinger equation for a non-spin-polarized atom at a reference energy E_i in the valence regime and for an angular momentum I_i,

$$\left(-\frac{1}{2}\nabla^2 + \nu_{eff}^{AE}\right)\left|\phi_i^{AE}\right\rangle = \varepsilon_i \left|\phi_i^{AE}\right\rangle \tag{2.47}$$

where V_{eff}^{AE} is the spherical component of the AE potential. The index i contains the reference energy ε_i the angular momentum quantum numbers (I_i, m_i), and the atomic coordinates R_i. The PS partial waves ϕ_i^{PS} are nodeless and identical to the AE partial wave outside a core radius r_c (approximately equal to half the nearest-neighbor distance) and match continuously to ϕ_i^{AE} inside these spheres. The projector functions p_i^{PS} are constrained to be dual to the partial waves, they are constructed by two-step procedure: First, intermediate functions χ_i

are computed via

$$|\chi_i\rangle = \left(\varepsilon_i + \frac{1}{2}\nabla^2 - \nu_{eff}^{PS}\right)|\phi_i^{PS}\rangle \tag{2.48}$$

where V_{eff}^{PS} is the spherical component of the effective pseudopotential, which can be chosen arbitrarily inside the radius r_c but must match V_{eff}^{PS} for $r \geq r_c$. The projector functions are linear combinations of the χ_i with

$$\left|\phi_i^{PS}\right\rangle = \sum_j \left(B^{-1}\right)_{ji} |\chi_j\rangle \, , B_{ij} = \left\langle \phi_i^{PS} \mid \chi_j \right\rangle \tag{2.49}$$

such that the ϕ_i^{PS} and p_i^{PS} are dual, $\left\langle p_i^{PS} \mid \phi_j^{PS} \right\rangle = \delta_{ij}$ and $\left\langle r \mid p_i^{PS} \right\rangle = 0$ for $r \geq r_c$

2.2.4 Molecular Dynamics calculation

2.2.4.1 Classical Molecular Dynamics

Molecular Dynamic (MD) is a microscopic form of computer simulation where the time evolution of a system of atoms is gouverned by Newton's laws of motion. Due to a lack of computational power, it was not until digital computers were invented that MD became a viable method of simulation. With the aid of modern computing, it is possible to numerically solve the equations of motion and use statistical mechanical theory to measure quantities of interest, such as temperature, pressure, and density. Thought the theory remains the same, MD simulations can be used for a variety of applications such as phase transition, polymers, biomolecules, and fluid dynamics. Numerical simulation consisting in calculating the temporal evolution of positions r_i and velocities v_i of a system composed of N interacting atoms, by numerically integrating the equations of classical Newtonian mechanics; $F = ma$; where F is the force exerted on the particle, m is its mass and a is its acceleration. The most computationally intensive part of an MD simulation is calculating the forces between pairs of

particles. For a potential function without a cutoff radius, it is necessary to evaluate forces for every pair within the simulation region. However, the use of a truncated potential function greatly reduces the number of interaction pairs, and subsequently the number of pairs worth investigating. Different numerical methods are used in MD simulations to find the trajectories of the particles. Besides, the size of the system should be set reasonably so the atoms in the system can perform desired motions without any additional constraints. The initial settings of a simulation also include the dimension of simulation, boundary conditions, and the units of the parameters. In a soft sphere MD simulation, atomic interaction is calculated based on the potential energy between individual particles. The ineteractions are, in general, described by interatomic forces between particles . In the nature , these forces are :

$$f = -\nabla U(r) \tag{2.50}$$

Where U(r) is a potential energy function. The behavior of a simulation is largely based on the choice of potential function(s). Potential function of interest are largely based on the Born-Oppenhiemer approximation that electrons adjust to movement faster than the nuclei. Therefore, particle interaction based on the movement of nuclei is valid

2.2.4.2 Ab initio Molecular Dynamics

Since the founding article by Car and Parrinello [52], ab initio molecular dynamics (AIMD) has emerged from all of the atomic-scale simulation methods. Its success is intimately linked to its capacity to describe the temporal evolution of the nuclear but also electronic degrees of freedom of a system, including the rupture or the formation of covalent bonds. Another crucial aspect is the moderate computational cost of the method (compared to Born-Oppenheimer type molecular dynamics), an essential element for the study of biochemical

systems. AIMD simulations thus provide reliable information on the structural, thermodynamic and dynamic properties of these systems, opening the door to a wide range of applications. We have applied this simulation technique to various solid-state hadrogen storage materials such as metal borohydride systems and their derivative. The difference betewen the Ab initio molecular dynamics and classical molecular dynamics is that the AIMD uses forces obtained from electronic structure theory calculations (typically density functional theory) to evolve the system's dynamics in time, while classical molecular dynamics uses forces obtained from (semi)empirical force fields. Ab initio molecular dynamics calculations are typically more accurate than classical MD calculations, especially for systems where there is charge transfer, many body van der Waals, relativistic effects, strong spin orbit coupling, or strong electron correlation (note there are many materials and molecules where these effects are critical to include). Ab initio MD, however, is often limited to systems of much smaller size and shorter time scales than classical MD due to the computational expense. Note, classical force fields or machine learned potentials can be parameterized to highly accurate reference data, thus in some instances they can be very accurate.

2.3 Software and Modeling

2.3.1 Quantum Espresso

In this thesis, all calculations were performed using the Quantum Espresso (PWSCF) code [52]. Quantum ESPRESSO stands for op**E**n **S**ource **P**ackage for **R**esearch in **E**lectronic **S**tructure, **S**imulation and **O**ptimization. It is a free software, released under the GNU General Public License. The code is designed to perform density functional theory calculations

of the electronic structure. It uses plane wave basis sets and pseudopotential in its applications. Its features range from the calculation of ground-state energy and Kohn-Sham orbitals to the calculation of atomic forces, stresses, and structural optimization, molecular dynamics on the ground state Born-Oppenheimer surface, Nudged Elastic Band (NEB) and Fourier String Method Dynamics. Quantum ESPRESSO is also able to perform other calculations such as; phonon frequencies and eigenvectors at a generic wave vector, effective charges and dielectric tensors, electron-phonon interaction coefficients for metals, Infrared and Raman (non-resonant) crosssection etc. [52, 53]. The main advantages of QE over VASP in the context of this work are as follows: first, QE is able to characterize the vibrational frequencies into either Raman or infrared active modes. Secondly, QE assigns modes on the basis of the degeneracy of the vibrational frequencies (single, double or triple). In addition, QE tells you to which irreducible representation a mode belongs. This makes it easy to interpret the results of Raman and infrared spectra. Quantum Espresso is presently divided into several executable, performing different types of calculations, although some of them have overlapping functionalities. Typically, there is single set of functions or a single Fortran 90 module that perform each specific task, but there are still important exceptions to this rule, reflecting the different origin and different styles of the original components. Quantum Espresso has in fact built out of the merging and re-engineering of different packages.

2.3.2 BoltzTraP Code

A program for calculating the semi-classic transport coefficients is described. It is based on a smoothed Fourier interpolation of the bands. From this analytical representation we calculate the derivatives necessary for the transport distributions. This method is compared to earlier calculations, which in principle should be exact within Boltzmann theory, and a very

convincing agreement is found. [54]. The BOLTZTRAP code allows the calculation of semi-classical transport coefficients through the use of Fourier expansions to solve Boltzmann equations. In the absence of fields, the stationary solution of the Boltzmann equation is the Fermi distribution function $f_0(\epsilon_k)$. The fact that the population in k and $-k$is the same makes $J = 0$. In absence of magnetic field and temperature gradients, it is possible to linearize, within the relaxation time approximation and we obtain the following solution for the population:

$$f_k = f_0(\epsilon_k) + (-\frac{\partial f_0}{\partial \epsilon})\tau_k v_k.E \tag{2.51}$$

Now that we obtained the population of states thanks to BTE within the RTA, we substitute equation (3.17) into (3.14) to get:

$$J = e\sum_k f_k v_k \tag{2.52}$$

It is easy to see that in the absence of a gradient of temperature, the macroscopic electrical current is $J = \sigma.E$, therefore:

$$\sigma = \sum_k (-\frac{\partial f_0}{\partial \epsilon})\sigma(k) \tag{2.53}$$

In the same way as for the density of states, the energy dependence of the conductivity tensor can be obtained by:

$$\Xi(\epsilon) = \frac{1}{N}\sum_k \sigma(k)\frac{\delta(\epsilon - \epsilon_k)}{d\epsilon} \tag{2.54}$$

With this, the transport tensors that depend on the chemical potential (μ) and temperature (T) can be obtained through:

$$\sigma(T,\mu) = \frac{1}{\Omega}\int \Xi(\epsilon)[-\frac{\partial f_\mu(T,\mu)}{\partial \epsilon}]d\epsilon \tag{2.55}$$

$$S(T,\mu) = \frac{1}{\Omega e T\sigma(T,\mu)}\int \Xi(\epsilon)(\epsilon - \mu)[-\frac{\partial f_\mu(T,\mu)}{\partial \epsilon}]d\epsilon \tag{2.56}$$

where the electrical conductivity still depends on the relaxation time τ, but not the Seebeck coefficient. τ is considered constant (no longer k dependent) and can be taken out of the

integral in equation (2.56).

2.4 COMPUTATIONAL METHODS

The results presented in this study were obtained from density functional theory (DFT) calculations using Quantum-ESPRESSO code [52] with the projector augmented-wave (PAW) method [50, 55]. Since van der Waals (vdW) interactions are a key factor in HER [56], the exchange-correlation (XC) functional $vdW - optB86b$ was employed for all DFT computations [46]. A kinetic-energy cutoff of 40 Ry was selected for the plane-wave basis set. All the structural models were fully optimized until the forces were less than 10-2 eV/Å with an energy convergence of 10-6 eV between two consecutive self-consistent steps. A vacuum space of 20 Å was applied perpendicularly to the slab to avert the interactions caused by periodic images. Due to the weak interaction between $MAPbI_3$ coupled with Fe_2O_3 and $ZnO : Al$, the vdW forces in the heterostructure interface are simulated by $vdW - optB86b$ method of Grimme [46, 47, 57]. We also performed molecular dynamics simulations of the bare slabs, i.e., without any water molecules, using the same a = b cell dimensions but leaving 10 Å of vacuum along the non-periodic direction orthogonal to the perovskite surface. In this sense, Car-Parrinello molecular dynamics (CPMD) simulations have been carried out within the Quantum Espresso package along with the GGA-PBE functional. For all calculations, electron-ion interactions were described by scalar relativistic ultrasoft pseudopotentials with electrons from $O, NandC : 2s, 2p; H : 1s; I : 5s, 5p; Pb : 6s, 6p, 5d; Zn, Fe : 3s, 3p, 3d, 4s, andAl : 3s, 3p$ shells explicitly included in the calculations. CPMD simulations have been performed with an integration time step of 10 au. For a total simulation time of ca. 50 ps. Initial randomization of the atomic positions has been used to reach temperature

of 300 ± 30 K. Variable cell geometry optimization of the $ZnO:Al$, $MAPbI_3$ and Fe_2O_3 systems was carried out using the QE code with plane-wave basis set cutoffs for the smooth part of the wave functions and the augmented density was 40 Ry, respectively and including dispersion contributions as reported elsewhere [58–60].

2.4.1 Power Conversion Efficiency

In an ideal perovskite of ABX_3, the radii of all these cations and anions should meet the tolerance factor:

$$t = \frac{(r_A + r_X)}{\sqrt{2}(r_B + r_X)} \tag{2.57}$$

and octahedral factor:

$$\mu = \frac{r_B}{r_X} \tag{2.58}$$

where RA, RB, and RX refer to the ionic radii of A, B and X, respectively [30]. Finally, the J_{SC} can be calculated by the equation (2.60):

$$P_S = \frac{2\pi f}{c^2 h^3} \int_{E_g}^{\infty} \frac{\epsilon^2}{(e^{(\frac{\epsilon}{K_B T_S})} - 1)} d\epsilon \tag{2.59}$$

The short-circuit current and open-circuit voltage can be calculated by Eq (2.60)

$$J_{SC} = e \times (F_{cell} - F_0) \tag{2.60}$$

where F_{cell} and F_0 are photon flux emitted by the solar and the photon flux at zero applied voltage, respectively.

$$J_{SC} = \frac{2\pi f}{c^2 h^3}(1 - e^{-\alpha(\epsilon)L})(\int_{E_g}^{\infty}(\frac{\epsilon^2}{(e^{(\frac{\epsilon}{K_B T_S})} - 1)})d\epsilon - \int_{E_g}^{\infty}(\frac{\epsilon^2}{(e^{(\frac{\epsilon}{K_B T})} - 1)})d\epsilon) \tag{2.61}$$

The open-circuit voltage according to the Shockley-Queisser limit can be calculated by Eq.(2.67)

$$V_{OC} = \frac{KT_{cell}}{e} ln(\frac{F_{cell}}{F_0}) \tag{2.62}$$

The fill factor and energy conversion efficiency of the solar cell are given by Eq.(2.63):

$$FF = \frac{max[J(V) \times V]}{J_{SC} \times V_{OC}} \tag{2.63}$$

$$\eta = \frac{max[J(V) \times V]}{P_S} \tag{2.64}$$

where e, E, and P_S are the charge of an electron, the incident photon energy, and the power radiated by the sun on earth per unit area, respectively[6,32,33].

2.4.2 Stain effect and Transport

2.4.2.1 Stain effect

Once the properties of unit cell of OHP-$CH_3NH_3PbI_3$ were obtained, the mechanical biaxial strain is imposed on the relaxed unit cell along x (100), and y (010) directions according to Eq. ((2.65)) as shown in Figure. 4.7:

$$\epsilon_{xx}(\%) = \frac{a - a_0}{a_0} \times 100\% \tag{2.65}$$

2.4.2.2 Electron Relaxation Time:

Since the electrical conductivity (σ) obtained from BoltzTraP is a quantity scaled by the constant relaxation time of unity (1 fs), the actual value of σ should be estimated using an appropriate relaxation time, giving the temperature and carrier concentration.

In this work, we adopted the **self-consistent single parabolic band model** to evaluate the electron relaxation time.

In the approach, we first determined the Fermi energy in the Fermi integral self consis-

tently from eq 3 for the given T and q concentration ($n(T)$).

$$n(T) = \frac{(2m_d^* K_B T)^{\frac{1}{2}}}{2\pi^2 \hbar^3} \tag{2.66}$$

The density of states effective mass is $m_d^* = {N_V}^{\frac{3}{2}} m^*$, where m^* is the effective mass at the band valley and the degeneracy of the band valley is given by N_V, which is related to the symmetry of the k-point in the Brillouin zone. The Fermi integral is given by eq**.

$$\tau = \frac{2^{\frac{1}{2}} \pi \hbar^4 \rho \nu_l^2}{3E_d^3 (m^* K_B T)^{\frac{3}{2}}} \frac{F_0(\eta)}{F_{\frac{1}{2}}(\eta)} \tag{2.67}$$

Here $\eta = \frac{E_f}{K_{BT}}$, where E_f is the Fermi energy. Using the E_f determined from eq **, the electron relaxation time can be obtained from eq **.

$$F_x(\eta) = \int_0^\infty \frac{\epsilon^2}{(1 + e^{\epsilon - \eta})} d\epsilon \tag{2.68}$$

In the above equation, ρ refers to the mass density, and the longitudinal sound velocity is given by ν_l. In our calculations, the longitudinal sound velocities in the a and c directions were computed as $(C_{11}/\rho)^{1/2}$ and $(C_{33}/\rho)^{1/2}$, respectively.

The deformation potential (E_d) at the band valley was obtained by $E_d = \frac{\partial E_V}{\partial (V/V_0)}$, where V and V_0 denote the cell volumes.

2.4.3 Heterostructure Photocatalysis

2.4.3.1 Band-edge positions

In any of the photocatalytic processes, the position of band edges determines the redox behavior of the charge carriers. Calculation of band edge position has a significant role in

determining the extent and feasibility of a particular photo-catalytic reaction. In this section, we are describing the conventional ways of determining the band positions of a semiconductor material. Manually one can arrive at the flat band potential of the semiconductors from the equation connecting electronegativity of the semiconductor (χ), energy of free electron on hydrogen scale ($E^e = 4.5eV$), conduction band position (E_{CB}) and bandgap(E_g)[37].

$$\chi(S) = \sqrt[N]{\chi_1^{Z_1}\chi_2^{Z_2}\chi_3^{Z_3}.....\chi_{n-1}^{Z_{n-1}}\chi_N^{Z_N}} \tag{2.69}$$

where $\chi(S)$ is Elements Electronegativity from $\chi_1^{Z_1}$ to $\chi_N^{Z_N}$.

$$\chi_i(S) = \frac{E_i^{IE} - E_i^{EA}}{2} \tag{2.70}$$

where IE and EA are Ionisation Energy Electron Affinity respectively

$$E_{CB} = \chi_i(S) - E^e - 0.5E_g \tag{2.71}$$

$$E_{VB}^0 = E_{CB}^0 + E_g \tag{2.72}$$

The geometric mean of the individual electronegativities of constituent atoms in a semiconductor would give the electronegativity of a particular semiconductor.

2.4.3.2 production yield of H_2

The calculated production yield of H_2 we have used the Rate of generation of excess carriers ΔG_L (unit volume/time):

$$\Delta I_{ph} = V\Delta G_L \tag{2.73}$$

$$\Delta G_L = \frac{\eta\Delta P}{h\nu AW} \tag{2.74}$$

where P is solar power ($\eta = (1-R)(1-e^{-\alpha w}) < 1$) is the quantum efficiency, A is the surface of device, R is refractive index, α is absorption coefficient, and W is the width the

device Figure 5.6.

$$n_e = \frac{\eta \Delta P}{h\nu} \frac{\tau_n}{t} \Delta t \tag{2.75}$$

where τ, t, and Δt are relaxation time of pair electron-hole, time of moving electron between the surface of semiconductor, and time of moving in the circle from the anode to cathode respectively.

Part II

Results and Discussion

CHAPTER 3

Efficiency and Substitution

3.1 Introduction

The perovskites with general formula ABX_3 have a wide range of attractive properties, which include both application-towards phenomena and fundamental physics [10, 61]. One of the main factors that make perovskites so successful is the adaptability of this structure type towards A, B, or X site substitution, which allows for tailoring properties to meet particular requirements. As has attracted a great deal of attention due to an impressive series of light to electricity efficiency conversion improvements. [62–64] Indeed, in just over five years of intense research activity, the efficiency of $(CH_3NH_3)PbI_3$ (from now on referred to as ABX_3 where A=cations, B=Pb, and X=I) is around 25% [65]. In this relatively young family, the perovskite architecture is essentially maintained, while at least one ion - usually A or X is substituted by an organic ion which makes the perovskite a hybrid as A, and B are cations (A has a larger radius than B), and X is a halogen or oxygen anion. The two different anions and various metal cations form halide perovskites and oxide perovskites [66]. These two

types of perovskites have many similar crystal structures, and both of them contain BX6 octahedra in their crystal structures, and A atoms locate in the interstitial void of neighboring octahedra [67]. Bernal et al. from first principles calculations was shown that the introduction substitutional halides [Br, Cl, and F] dopants for I anions in $MAPbI_3$ could facilitate charge transfer from the hybrid perovskite to the electrodes [68]. Whereas, substituting in B-site changes the band gap. In our study, we investigated the possibility of substitution of the cation at the A-site and its effect on perovskite organic properties. The above analysis suggests that substitution the cation A into perovskites may be a possible way to obtain the optimal band gaps (1.1–1.4 eV) and high efficiency. Where Ai (Ai = CH_3NH_3, $CH(NH_2)$, Li_3O, Li_3S, NH_4 [10], Cs, CH_3OH, $CH_3-C-(NH_2)_2$, and C(NH2)3) were substituted into ℵ phase (cubic) CH3NH3PbI3 hybrid perovskites. Ali et al, claim that the halide perovskites can show photovoltaics property by replacing $Pb_2{}^+$ with $Sn_2{}^+$ and $Ge_2{}^+$, while the single replacement of $Pb_2{}^+$ with other $B_2{}^+$ (B = Mg, Mn, Fe, Co, Ni, Cu, Zn, and so on) cation is suitable for other physical properties, such as magnetism, dielectric, ferroelectricity, multiferroicity, and so on [69].

3.1.1 Tolerance factor and octahedral factor:

Recently, Tolerance Factor concept of Goldschmidt's has been a central mantra in the development of perovskites for decades, was extended to the emerging field of organic-inorganic perovskites [70–72]. The t value often varies from 0.8 to 1.11; otherwise, the cubic or cubic-like crystal structure would be distorted, and even destroyed.4 A smaller t value would result in lower-symmetrical tetragonal or orthorhombic structures. The t value of an ideal cubic structure varies in the range from 0.89 to 1.0. The value of μ ranges between 0.44 and 0.90, which determines the stability of the octahedron, and further affects the stability

of the perovskite structure [73]. Among of 2352 calculated TF, 742 show TF between 0.8 and 1.0 that include about 140 known materials [67], such as the well characterized hybrid perovskites Figure.3.1 This work was limited to nine cations (CH_4, Cesium, Li_3O, CH_3OH,

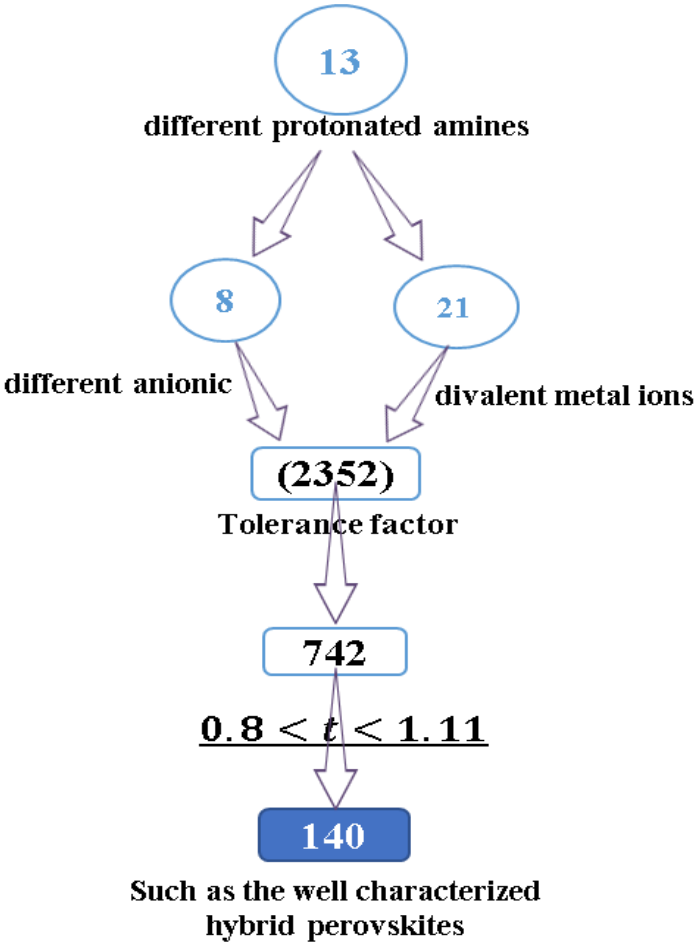

Figure 3.1: A diagram showing a method for selecting organic cations from a protein by machine learning, which fulfills the conditions of tolerance factor and octahedral factor .

Li_3S, CH_3NH_3, $CH(NH_2)_2$, $CH_3C(NH_2)_2$, and $C(NH_2)_3$) Figure 3.23.3, which have ionic radii (146, 167, 170, 216, 220, 222, 253, 277, and 278) respectively [74].

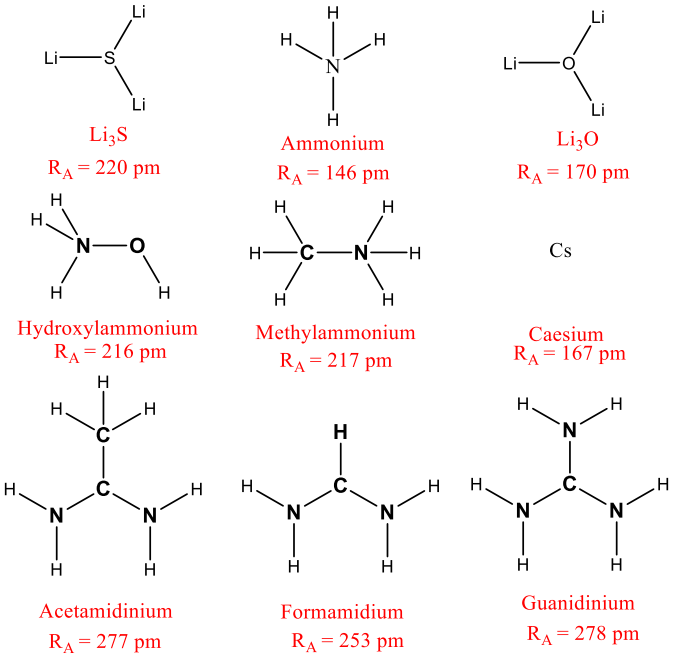

Figure 3.2: The chemical formula and molecular radii of the cation we used in the work.

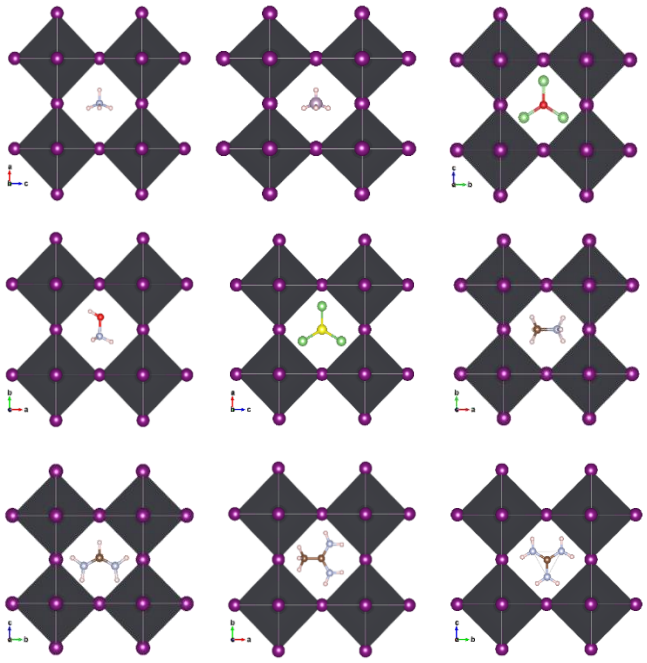

Figure 3.3: Geometric structures of AiPbI3 with different cation before the optimization.

3.1.2 Evaluation of Efficiency:

For all perovskites (except for the perovskites with Li_3O and Li_3S), the short circuit current (J_{SC}), the open-circuit voltage (V_{OC}), and the PCE also calculated for the solar cells based their bandgap (E_g). We assumed that the energy more than E_g, for all photons, are absorbed, and always promote the perovskites to produce electron-hole pairs. In order to consider the effect of the electrodes and interfacial layers, the V_{OS} was calculated by the equation ((2.63)). Finally, by using J_{sc}, V_{oc}, and FF as well as the total incident power density PS, we calculated the maximum theoretical limit of the PCE for all configurations, where the efficiency is regarded as a function of Eg, and P_S is the total incident power, which can be calculated by using solar spectrum data [75–77].

3.2 Results and discussion:

3.2.1 Optimization:

We have used density functional theory (DFT) and molecular dynamics, we theoretically investigated a crystal structure, electronic structure, Thermal and dynamical stability, and the power conversion efficiency of the substituted cubic A_iPbI_3 (A_i = CH_3NH_3+, N, $(NH_2)_2CH^+$, PH_4^+). Optimization: We optimized the structures after replacing the cations while observing the distortions in the nascent crystallites relative to the pristine crystal of $CsPbI_3$. We have noticed the distortion clearly in some structures, especially those that cations large, or (Li_3S^+, Li_3O^+) size cations Figure.3.4. Otherwise, the other structures have not changed significantly. A full list of all calculated parameters is given in table 3.1. Tolerance factor

Parameter	A	B	C	α	β	γ	Space Group:
NH_4PbI_3	6.3079	6.2407	6.3912	90.0000	90.0000	90.0000	P m
PH_4PbI_3	6.5455	6.5486	6.5574	90.0000	90.0000	90.0000	P m -3 m
Li_3OPbI_3	6.8934	6.9410	6.9572	90.0000	90.0000	90.0000	P m m 2
NH_3OHPbI_3	6.3388	6.3572	6.3517	90.0000	90.0000	90.0000	P m
Li_3SPbI_3	6.6913	6.6140	6.5984	90.0000	90.0000	90.0000	P1
$MAPbI_3$	6.4271	6.4006	6.4547	90.0000	90.0000	90.0000	P m
$FAPbI_3$	6.4918	6.5457	6.3295	90.0000	90.0000	90.0000	P m m 2
$AcPbI_3$	7.6505	7.0395	6.2866	90.0000	90.0000	90.0000	P1
$GuPbI_3$	7.2249	6.5031	6.4847	90.0000	90.0000	90.0000	P1

Table 3.1: The theoretical lattice constants A, B, C, α, β, and γ and Space Group of A_iPbI_3 with the different cations .

and octahedral factor and parameters optimization: In our research, we replaced MA with a number of different sized organic cations and their constituent atoms in perovskite in the cube phase, and for a first examination of the stability of the crystal lattice with each cation, we calculated the tolerance factor τ with the octahedral stability factor μ and matched them with the permissible ranges, which were arranged. In ascending order of size as shown in Table 3.1 below. Through the results, it was found that all of them fall within the range of stability [78].

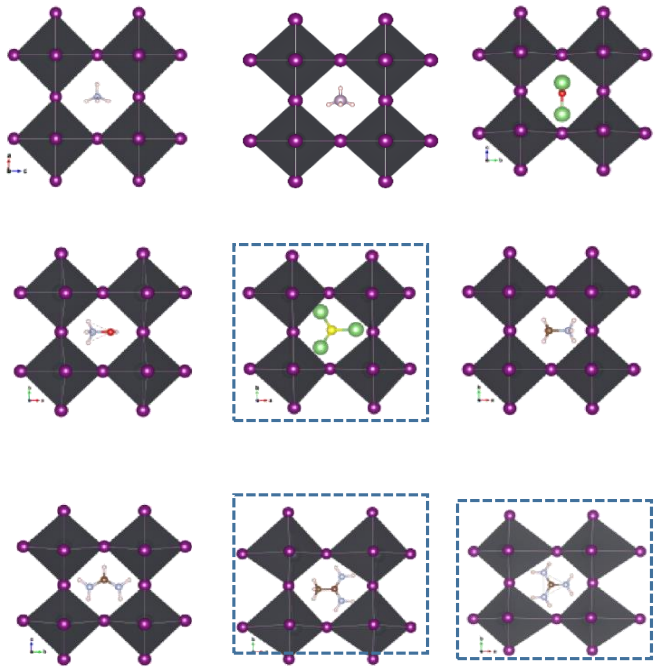

Figure 3.4: Geometric structures of A_iPbI_3 after optimization with $VanderWaals$ correlation.

3.2.2 Electronic properties:

For photovoltaic applications, selection of materials for absorber layer with suitable electronic properties plays a vital role in improving the device performance. In this respect, the nature and magnitude of band gap is extremely important to estimate the number of absorbed photon and rate of photogenerated charge carriers with minimal optical losses. For efficient generation and transport of free charge carriers, low exciton binding energy as well as low effective masses of holes and electrons are also required. Moreover, DFT calculations show that electronic structures of the investigated substituted perovskites were similar with that of $MAPbI_3$, while their bandgaps slightly decrease or increase compared to that of $MAPbI_3$ except LiO_3, LiS_3, and Gu. Our results mean that substitution in halide perovskite is effective technique to improving thermal and dynamical stability and power conversion efficiency

and tune the band gap. For this purpose, we have calculated the band structures of the opti-

Å	R_A (pm)	$E_g(eV)$	$E_f(eV)$	μ	t
Ammonium	146	1.7611	-0.32564	0.468182	0.801242
Phosphonium	167	1.8411	-0.34885	0.468182	0.847215
Li_3OPbI_3	170	0.5932	-0.34170	0.468182	0.853782
Hydroxyl-ammonium	216	1.5348	-0.35955	0.468182	0.954485
Li_3SPbI_3	220	0.4146	-0.34944	0.468182	0.963241
Methylammonium	222	1.5971	-0.36116	0.468182	0.967620
Formamidinium	253	1.4815	-0.36469	0.468182	1.035485
Acetamidinium	277	1.9645	-0.37708	0.468182	1.088025
Guanidinium	278	2.1517	-0.37980	0.468182	1.090214

Table 3.2: The theoretical size R_A (pm), Bandgap E_g, Formation energy E_f, tolerance factor t, and octahedral factor η of A_iPbI_3 with the different cations .

mized (Ai)PbI_3 perovskite structures with GGA-PBE for (Ai = NH_4, Cs, Li_3O, NH_3O, Li_3S, CH_3NH_3, $CH(NH_2)_2$, Ac, and Gu) along the high symmetry points of the Brillouin zone, which has taken three space groups cubic, triclinic, and orthorhombic as shown in Figure 3.5. Here the Fermi level is set to zero. It is clearly observed from the figure that both the valence band maximum (VBM) and conduction band minimum (CBM) for all the computed band structures lie along the points R, Q, and E of the Brillouin zone for ((Cs, Li_3O, $CH(NH_2)_2$); (Li_3S, Ace, Gu - NH_4), (NH_3O, MA)) respectively which represent direct nature of the band gaps, and thus, can be called as good optical absorber materials Figure (4c). The calculated band gaps for NH_4PbI_3, $CsPbI_3$, Li_3OPbI_3, NH_3OPbI_3, Li_3SPbI_3, $CH_3NH_3PbI_3$, $CH(NH_2)_2PbI_3$, $AcPbI_3$, and $GuPbI_3$ are 1.7611, 1.6101, 0.5932, 1.5348, 0.4146, 1.5971,

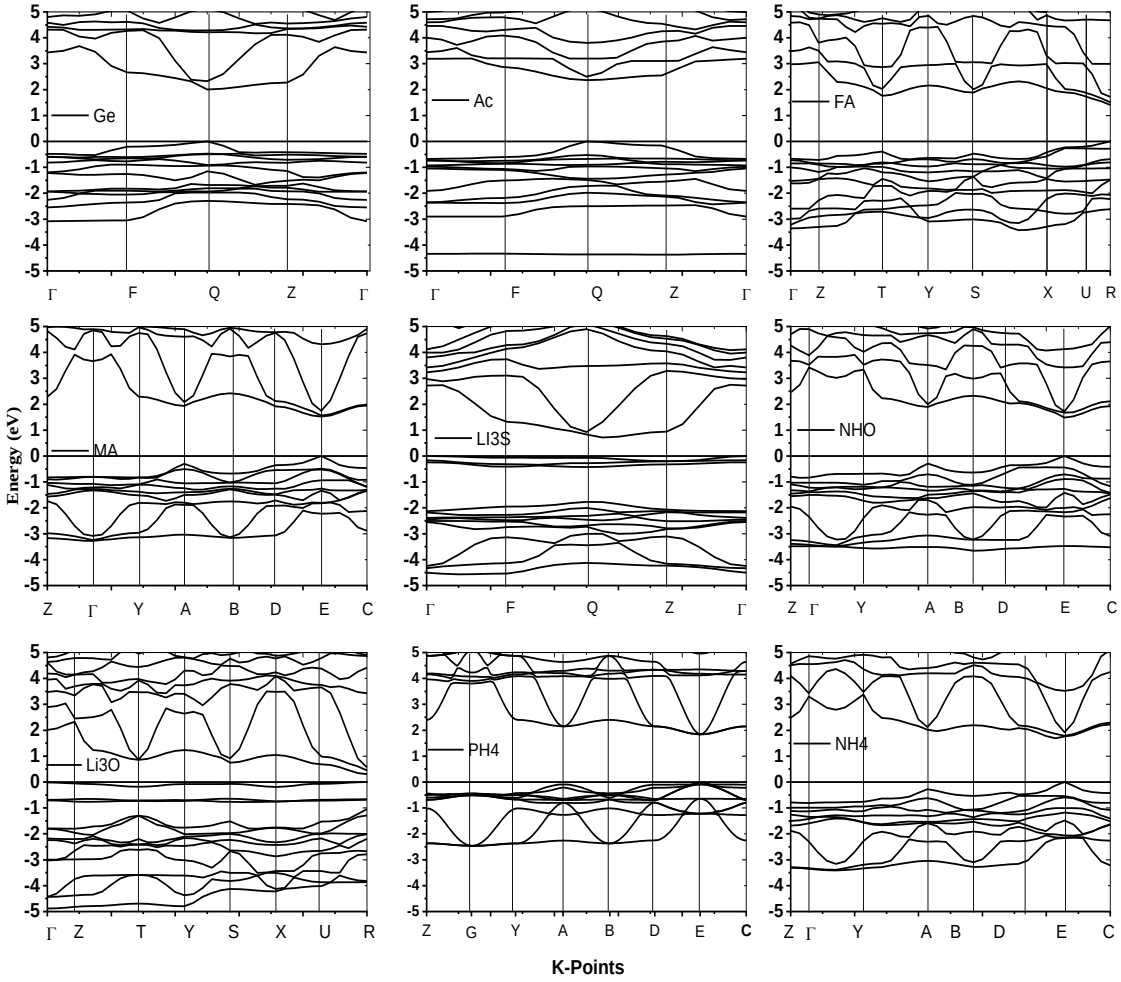

Figure 3.5: a- The variation of formation energy and bandgap function of the different cations b- The potential energy with A_iPbI_3 c- band structure of A_iPbI_3 in comparison with Van der Waals.

1.4815, 1.9645, and 2.1517, eV respectively which is in fairly agreement with the experimental results and other theoretical calculations as given in Table 3.2.

3.2.3 Stability:

3.2.3.1 Formation Energy:

The formation energies of cubic NH_4PbI_3, $CsPbI_3$, Li_3OPbI_3, NH_3OPbI_3, Li_3SPbI_3, $CH_3NH_3PbI_3$, $CH(NH_2)_2PbI_3$, $AcPbI_3$, and $GuPbI_3$ perovskites are -0.32564, -0.34885, -0.34170, -0.35955, -0.34944, -0.36116, -0.36469, -0.37708, and -0.37980 eV per unit-cell (see Table 1), respectively, which reveals that these perovskites can be synthesized in the laboratory. We also observed that the formation energy was increasing with the increase in the cation size in all structures except for the lithium and oxygen structures Figure 3.6. The reason may be attributed to the poor thermal stability. Where the formation energies were calculated by equation (3.1):

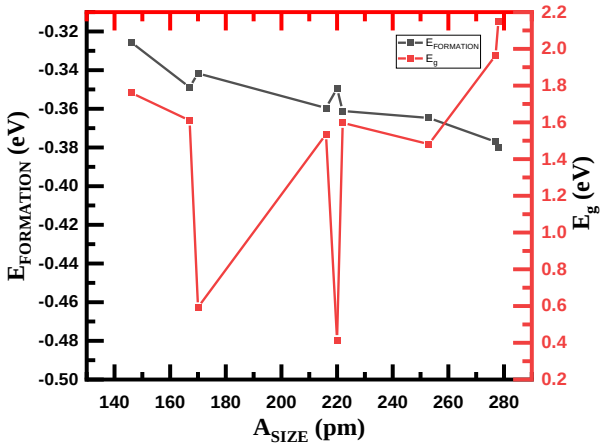

Figure 3.6: The variation of formation energy and bandgap function of the different cations of A_iPbI_3 in comparison with Van der Waals where A_i = PH_4 CH_3NH_3,NH_4, NH_3O, $CH(NH_3)_2$, Li_3O, Li_3S, Aec, and Gu.

$$E_F^{A_i} = \frac{E_{Total}^{A_i BX_3} - yE_{Total}^{BX_3} - xE_{Total}^{A_i}}{x+y} \tag{3.1}$$

where A_i is the different cation, x and y are the numbers of A_i and BX_3 atoms in a unit cell, respectively

3.2.3.2 Dynamical stability:

The total phonon density of states (Ph-DOS) is calculated at the equilibrium volumes for different cations of A_i. For the Ai modifications, the Ph-DOS are calculated both at the equilibrium point. The calculated Ph-DOS of cations are displayed in Figure 3.7. For all

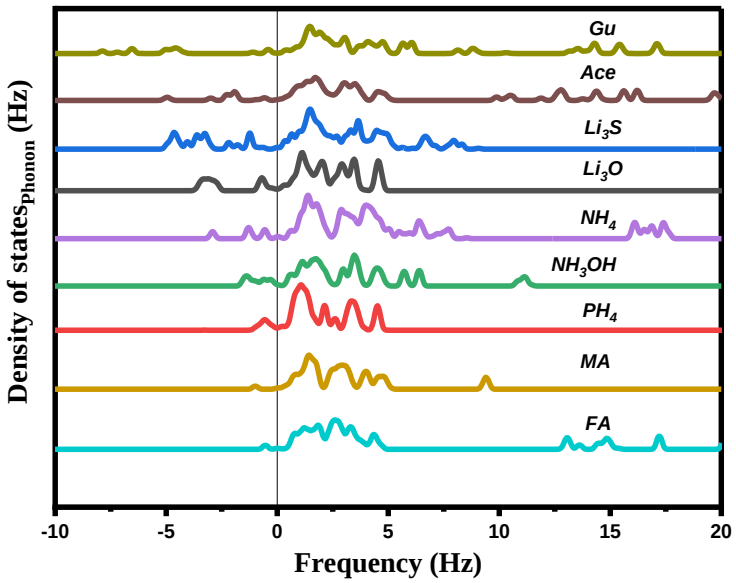

Figure 3.7: The DOSPhonon of AiPbI3 are showing the density of state function frequency with different cations.

these cations, no imaginary frequency was observed (for MA and Cs cations), also a small imaginary frequency was observed in (FA and NH3OH cations), indicating these structures are stable or at least dynamically stable at ambient conditions. Otherwise, the imaginary

frequency was observed in the remaining structures, indicating these structures are unstable at ambient conditions.

3.2.3.3 Thermal stability:

In this work, we used the ab initio molecular dynamics simulation (AMD) of A_iPbI_3 based on forces calculated from density functional theory. The simulations were performed on model systems having 3 × 3 × 3 supercells, and for a total simulation time of 25 ps in each case. Analysis of the finite size effects, in particular the mobility of the organic component, suggests that the smaller system is over correlated through the long-range electrostatic interaction. In the larger system, this finite size artifact is relaxed, producing a more reliable description of the anisotropic rotational behavior of cations. To compare the dynamics performance of the perovskites with the cations, the AMD simulations are carried out for the cubic NH_4PbI_3, $CsPbI_3$, Li_3OPbI_3, NH_3OPbI_3, Li_3SPbI_3, $MAPbI_3$, $AMPbI_3$, $AcPbI_3$, and $GuPbI_3$ perovskites with 3 × 3 × 3 supercell. Their AMD simulation results have illustrated in Figure 3.9 after 25 ps that the cubic Li_3OPbI_3 and Li_3SPbI_3 perovskites with a 3 × 3 × 3 supercell have an unstable dynamics performance, and these perovskites quickly undergo a phase transition to pseudo-perovskite phases. The unstable dynamic performances of these perovskites can be attributed to the strong interaction between these cations LiO_3 and LiS_3 with anion PbI_3. The previous study also showed that A-site cations in $APbI_3$ (Ai = the cation) perovskites have a strong interaction[34]. Otherwise, the $CsPbI_3$, $MAPbI_3$, $AMPbI_3$, $AcPbI_3$, and $GuPbI_3$ perovskites show stable dynamics performances and have no phase transition, during AIMD simulations of 25 ps, which may be attributed to the hydrogen-bonding between the cation and anions (PbI_3 frame). Figure 3.8 shows the fluctuation of the temperature and total energy of $AiPbI_3$ structures at the same time and temperature, where the

average temperature and total energy of $AiPbI_3$ remain constant over time where Ai= PH_4 CH_3NH_3,NH_4, NH_3O, $CH(NH_3)_2$, Li_3O, Li_3S, Aec, and Gu.

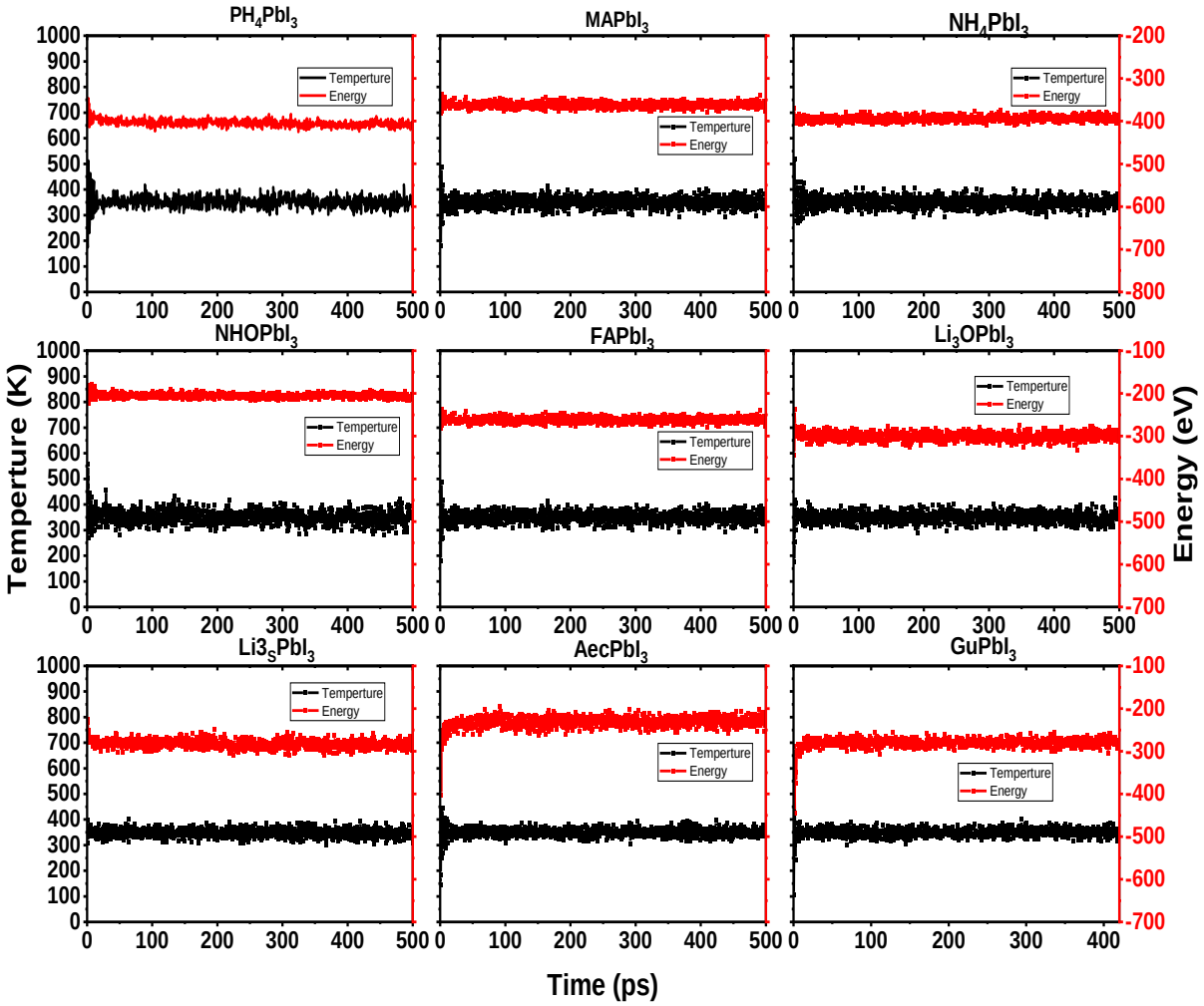

Figure 3.8: Ab initio molecular dynamics simulation: the fluctuation of the total energy and temperature with time (50 pm) at 300 K of $AiPbI_3$ structure where Ai= PH_4 CH_3NH_3,NH_4, NH_3O, $CH(NH_3)_2$, Li_3O, Li_3S, Aec, and Gu .

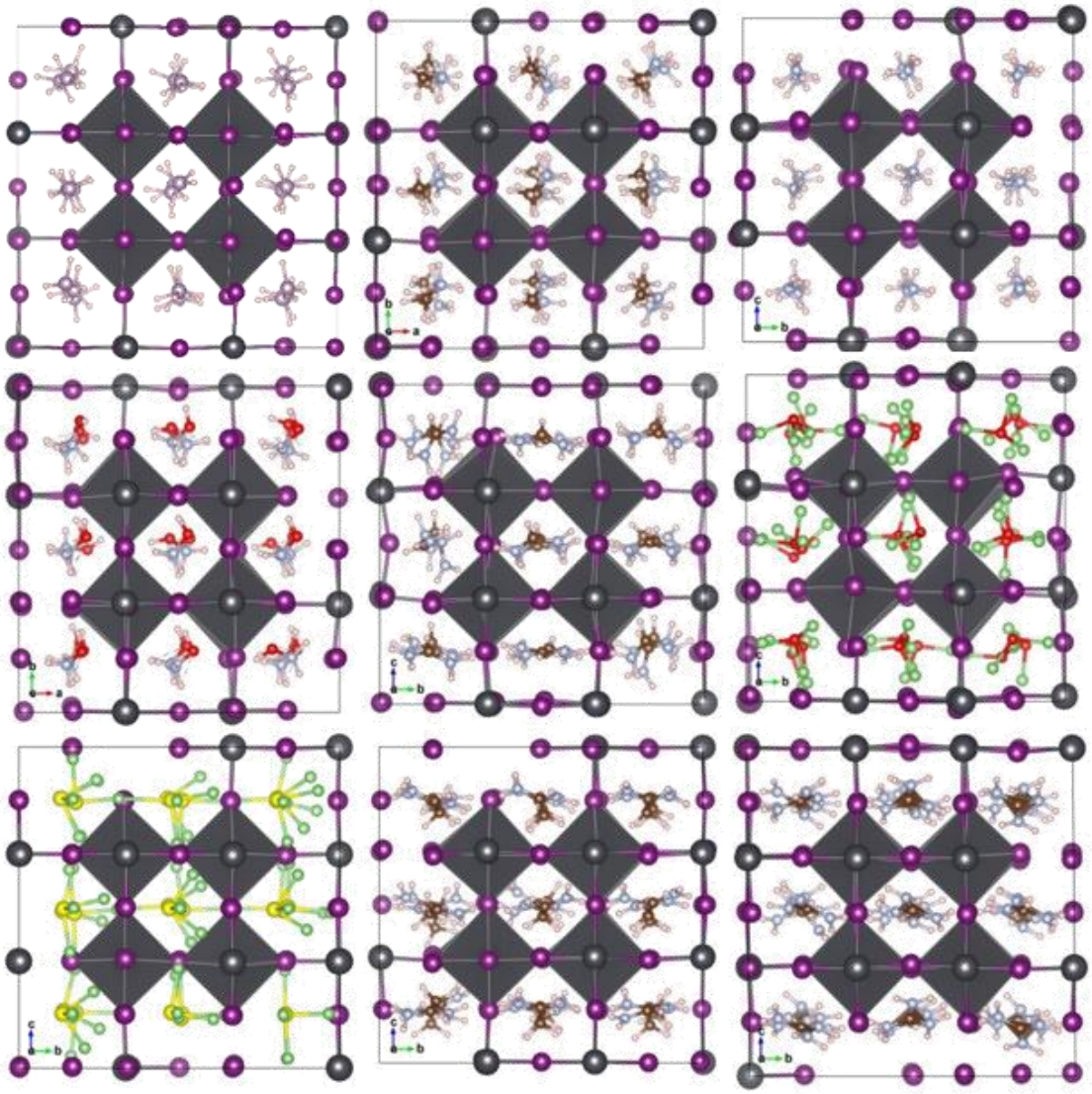

Figure 3.9: Structures of A_iPbI_3 obtained by molecular dynamics (AMD) simulations after 50 ps. For all simulations at 300 K where Ai= PH_4 CH_3NH_3,NH_4, NH_3O, $CH(NH_3)_2$, Li_3O, Li_3S, Aec, and Gu.

3.2.4 Optical properties:

Optical properties viz. absorption edge, strength of absorption at different wavelengths and reflection coefficient are vital and essential in determining the internal and external quantum efficiencies of the solar cell, see eq (5). These optical properties are the outcome of the interactions of light wave with the valence electrons of the material. When electromagnetic radiation such as light wave interacts with a material, the optical response of the material is given by the complex dielectric function $\varepsilon(\omega)$.

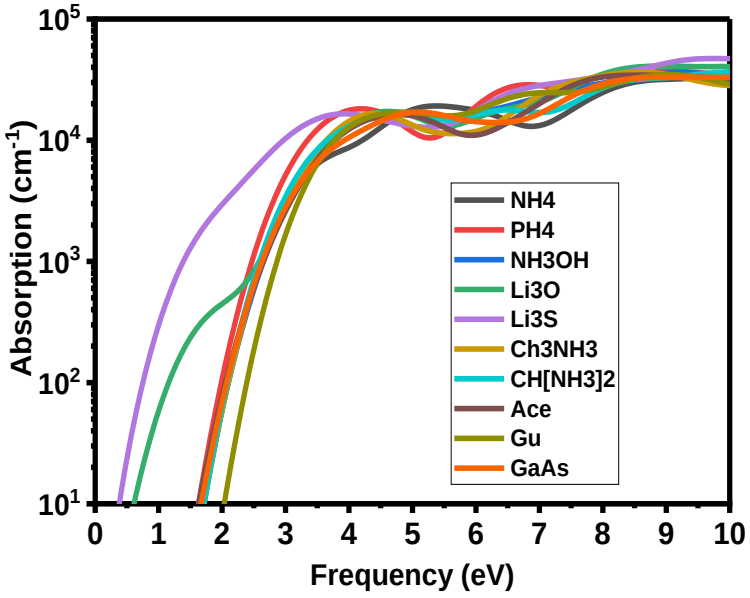

Figure 3.10: Dielectric function, (b) absorption coefficient, and (c) loss function of A_iPbI_3 as a function of energy.

3.2.5 Power conversion efficiency (PCE):

In order to roundly assess the PCE (η) of the single-junction perovskite solar cells based on $MAPbI_3$, and $CsPbI_3$ perovskites, their Voc, Jsc, and η are shown in Table 3. The maximum open-circuit voltage of 1.1 V, the maximum short circuit current density of 26.94 $mAcm^{-2}$, and the maximum PCE of 25.85% are obtained for the single-junction perovskite solar cells based on the cubic NH_4PbI_3, $CsPbI_3$, $HAPbI_3$, $MAPbI_3$, $FAPbI_3$, $AcePbI_3$, and $GuPbI_3$ perovskites, respectively. For each calculation the considered power input is Ps = 100 mW/cm^2,

	J_{CS}	FF	V_{OC}	η (%)	E_g
NH_4PbI_3	24.84	66.4391	1.02	21.39543	1.7611
$CsPbI_3$	25.9	68.3652	1.07	24.08043	1.6101
$HAPbI_3$	26.94	68.6404	1.10	25.85328	1.5348
$MAPbI_3$	26.04	68.2843	1.09	24.63394	1.5971
$FAPbI_3$	27.38	69.4876	1.006	24.32676	1.4815
$AcePbI_3$	23.75	63.1115	1.01	19.24151	1.9645
$GuPbI_3$	20.97	61.6615	1.005	16.51673	2.1517

Table 3.3: The calculation of current J_{CS} $mAcm^{-2}$, the fill factor FF, voltage open circuit V_{OC} eV , and the power conversion efficiency (PCE) η (%) of NH_4PbI_3, $CsPbI_3$, $HAPbI_3$, $MAPbI_3$, $FAPbI_3$, $AcePbI_3$, $GuPbI_3$ respectively .

that is the power under the maximum AM1.5 solar illumination spectrum. The different composition of the charge densities for CBM and VBM states indicates that the electron-hole pairs are easily separated and transported, which suggest that the solar cells based on these perovskites have potential advantages for obtaining high PCE. To further estimate the PCE

of the solar cells based on these perovskites, their PCE as the function of the band gaps is shown in Figure 3.11. The PCE of 25.85% of the single-junction solar cells based the cubic

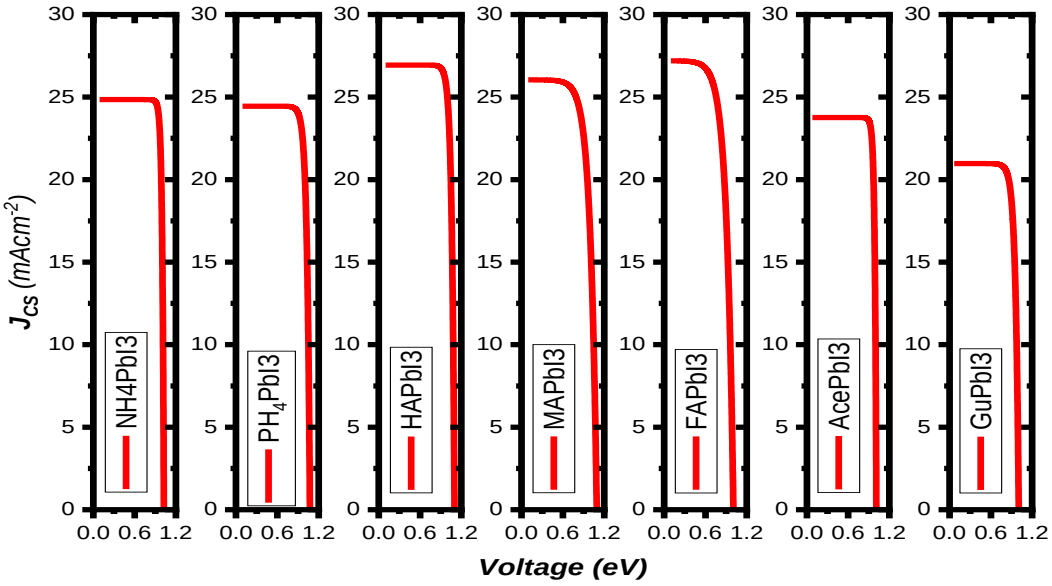

Figure 3.11: The curves of short-circuit current are a function of the open-circuit voltage of $AiPbI_3$ with different cations under AM 1.5 G illumination at 100 mW/cm^2.

$HAPbI_3$ perovskite is the highest, and the PCE of 24.63% of the single-junction solar cells based the cubic $MAPbI_3$ perovskite take second place. Table 3.3

The maximum of the power conversion efficiency is observed for a bandgap of 1.4–1.6 eV. While the cubic $GuPbI_3$ perovskite with the maximum direct band gap of 2.15 eV can also show the PCE of 16.52% in these perovskites. The PCE results of these perovskites suggest that they can be viewed as an excellent light-absorbing material for single-junction solar cells Figure 3.12.

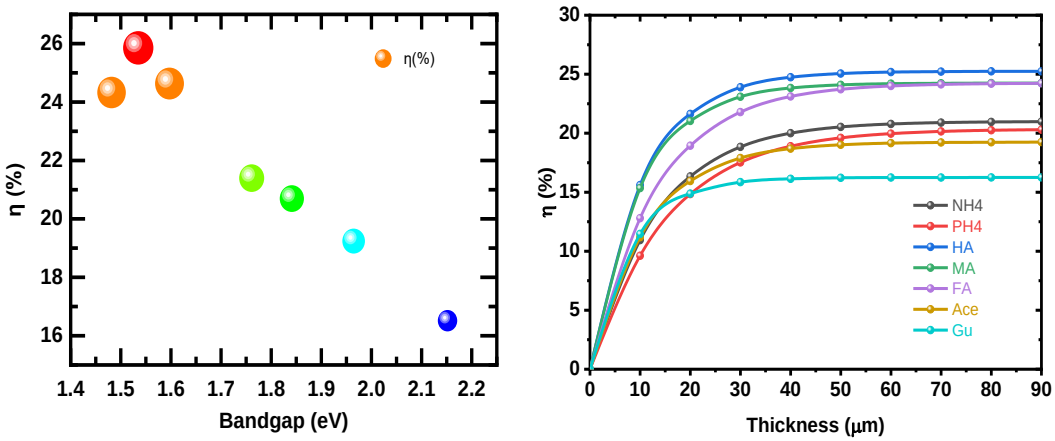

Figure 3.12: a. The variation of theoretical efficiencies under AM1.5 illumination in relation to bandgap energy is due to cation substitution in the A-site b. The efficiency varies according to the thickness of all structures..

3.3 Conclusions

In conclusion, we estimated the possibility of the formation of 3D perovskite structures by calculating tolerance factors t and and octahedral factors μ for 486 permutations of ABX3 organic-inorganic hybrid compounds. 9 organic monoammonium cations were investigated in combination with Pb metal ions and I halide. In order to estimate the steric size of the molecular cations, we considered the simple NH4+ as reference. However, there a lot of hitherto unknown hypothetical compounds can be claimed to build-up stable 3D perovskite phases at ambient conditions. We expect that this study will animate further research activities in designing perovskite structures with defined optoelectronic properties, and that the great constitutional flexibility of perovskites along with their promising physical properties will render them a prominent chemical structure in ferroelectrics and the next generation of photovoltaics.

CHAPTER 4

Electronic and transport properties of $CH_3NH_3PbI_3$

4.1 Introduction

Perovskite is the most recent and promising form of research and represent a real technological breakthrough in photovoltaics (PV) technologies. Especially, the yield of perovskite-hybrid cells increased in last years, from 12% to exceed 20% [4, 79, 80]. This makes perovskite hybrid system a promising one suited to many applications and less expensive than conventional silicon solar cells. Nowadays the best known hybrid perovskite and wish as the origin of the "break through" material in the photovoltaic field is $OHP - \mathrm{MAPbI_3}$. The state of the art on the crystalline, electronic and optical structures of $OHP - \mathrm{MAPbI_3}$, is evolving very quickly due to the enthusiasm of researchers for this material. The spectacular success of this material is primarily due to these different properties: ambipolar transport properties, high charge carrier mobilities, diffusion lengths of carriers and the possibility of changing the optical gap by simple substitution of the halogen. Moreover, the chemical flexibility of these hybrid perovskites and their different shapes give the hope of being able to

work and improve the material in the context of PV applications. The particularly feature of $OHP-\mathrm{MAPbI_3}$ which distinguish it from other materials for photovoltaic applications, is the orientation of $MA^+ = CH_3NH_3^+$ ions that has a critical impact on the optical and electrical properties relevant for photovoltaic applications [81]. The microscopic mechanism of the high photovoltaic performance and these properties is yet to be fully understood. Among proposed microscopic pictures, one scenario is based on presence of nanoscale ferroelectric domains [82] and rearrangement of the inorganic scaffold which is intimately linked with the $MA^+ = CH_3NH_3^+$ ion orientation [83]. In this regard, it will be extremely interesting if manipulations of $MA^+ = CH_3NH_3^+$ ions orientation can be done. Nowadays, various approaches can be applied to engineer electronic structures, optical and electrical properties of materials and nano-materials for PV application [84,85]. In order to use $OHP-\mathrm{MAPbI_3}$ as photovoltaic materials and for other applications, it is interesting to find out a way to ameliorate their physical properties. In this study, the role of biaxial strain on $OHP-\mathrm{MAPbI_3}$ and their effect on the stability, optical and transport properties was investigated. It was obvious to attempt to use strain to control those appealing anisotropies of $OHP-\mathrm{MAPbI_3}$. Our results present an important advancement towards controlling physical properties of $OHP-\mathrm{MAPbI_3}$ via strain engineering, with important implications to create new materials and devices for a wide range of applications. In this study, typical functionals for each approach have been chosen to represent their respective class. The functionals parameterized by (PZ81) [23] and Perdew-Burke-Ernzerhof (PBE) [86] are employed for local LDA and semi-local GGA methods, respectively. Here, we use the non-local vdW-DF method proposed by Dion et al. to describe the vdW interaction as modified by Klimes $etal$ [87], [88] In this approach, the XC energy E_{XC} takes the form:

$$E_{XC} = E_X^{GGA} + E_C^{LDA} + E_C^{nl} \tag{4.1}$$

Here, the exchange energy E_X^{GGA} uses the optimized optB86b GGA functional, [41] and E_C^{LDA} is the LDA functional for correlation energy. E_C^{nl} is obtained using a relatively simple double space integration. Once the properties of unit cell of $OHP-\mathrm{MAPbI_3}$ were obtained, the mechanical biaxial strain is imposed on the relaxed unit cell along x [100], and y[010] directions according to Eq. 4.1 as shown in Fig. 1b:

4.2 Results and discussion

4.2.1 The Optimal Relaxation Parameter for the Organometallic

$Approximation$	$para$	Exp(Å) [89]	Our results (Å)	$V_0(\text{Å}^3)$	$V(\text{Å}^3)$	$\epsilon(\%)$
Van der Waals	a	8.861	8.807	962.543	950.638	1.236%
	b	12.659	12.611			
	c	8.581	8.559			
GGA	a	8.861	8.548	962.543	892.467	7.28%
	b	12.659	12.320			
	c	8.581	8.475			
LDA	a	8.861	8.361	962.543	844.986	12.21%
	b	12.659	12.149			
	c	8.581	8.318			

Table 4.1: The theoretical lattice constants and $\mathrm{Pb-I}$ bond lengths of orthorhombic $\mathrm{CH_3NH_3PbI_3}$ in comparison with the experimental data .

This conclusion is different from the assumption presented in the recent theoretical stud-

ies on organic-inorganic hybrid tetragonal perovskite materials [7]. The optimized atomic structure of the orthorhombic $CH_3NH_3PbI_3$ crystals using the optB86b+ vdWDF functional is shown in Figure 1.6. The structures deduced from the XRD refinement experiments show angular distortions of the $[PbI_6]$ octahedra, [90] such as anions showing a significant transverse displacement from the mid-point of the Pb-Pb distance to which they are constrained in the ideal crystallographic description Figure 1.6.

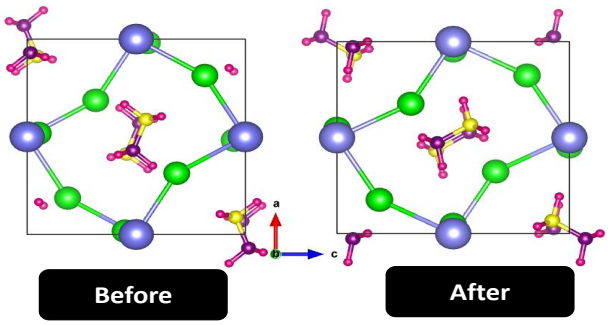

Figure 4.1: The relaxation of lattice orthorhombic $CH_3NH_3PbI_3$ in comparison with Van der Waals.

4.2.2 Structural, Electronic and Thermal Properties:

The displacement of atoms causes a reduction in symmetry of the $CH_3NH_3PbI_3$ crystal from the cubic phase to the orthorhombic phase. These structural differences indicate that I_1 and I_2 atoms are inequivalent atoms. Since the organic-inorganic hybrid perovskite $CH_3NH_3PbI_3$ materials are used as light harvesters in DSCs, [54, 81–83] their electronic structures are crucial factors for sunlight absorption. In this regard, the total density of states (TDOS) is calculated using the various functionals (see Figs 4.2). In our calculations, the bandgap energy with the PZ81/LDA functional is $1.553eV$, which is 8.65% less than that with the PBE/GGA functional. Our bandgap energy of the PBE/GGA functional is $ca.$ 5.88% larger than the previous theoretical value [90]. This is because the lattice constants used in our

study are 7.28% larger than the previous one, in which the experimental lattice constants were used. Our results support the strong relationship between structural properties and bandgap energies, and highlight the importance of using approximations which accurately reproduce the correct geometry [91]. When the optB86b+ vdWDF functional is employed, the theoretical bandgap energy is $1.74eV$, which is $ca.\ 0.1eV$ smaller than that with the PBE functional. This difference can also be ascribed to the different theoretical lattice constants given by various functionals. According to the optical absorption experiments, the electronic bandgap of orthorhombic $\mathrm{CH_3NH_3PbI_3}$ crystals is $1.68 - 1.72eV$ at low temperature. [92] Consequently, the experimental bandgap energies of hybrid $\mathrm{CH_3NH_3PbI_3}$ are surprisingly close to the theoretical predictions at the semi-local and non-local levels. Previous DFT studies demonstrate that the bandgap energies of solid-state semiconductors are seriously underestimated by using pure DFT functionals. In some cases, the deviation is about 30% [93]. This is because good band gaps are not normally to be expected from functionals of the types tested here, which do not have hybrid characters [94]. This successful match is likely to be fortuitous, which is also observed in other Pb-based materials [95]. (see Figure 4.2) also DFT functionals shows that the characteristics of peaks using various functionals in TDOS images are broadly similar, except for the locations of the peaks.

To understand the bonding mechanisms between the atoms, the analysis of partial density of states (PDOS) has been performed. The calculations of TDOS reveal that the functionals have small effects on the main characteristics of peaks. Therefore, only the analysis of PDOS using the optB86b+ vdWDF functional is shown in Figure 4.3. The PDOS images of I_1 and I_2 support the argument that these two kinds of I atoms are chemically inequivalent. The PDOS peaks of I_2 atoms are closer to the Fermi energy and sharper than those of I_1 atoms in the top valence bands.

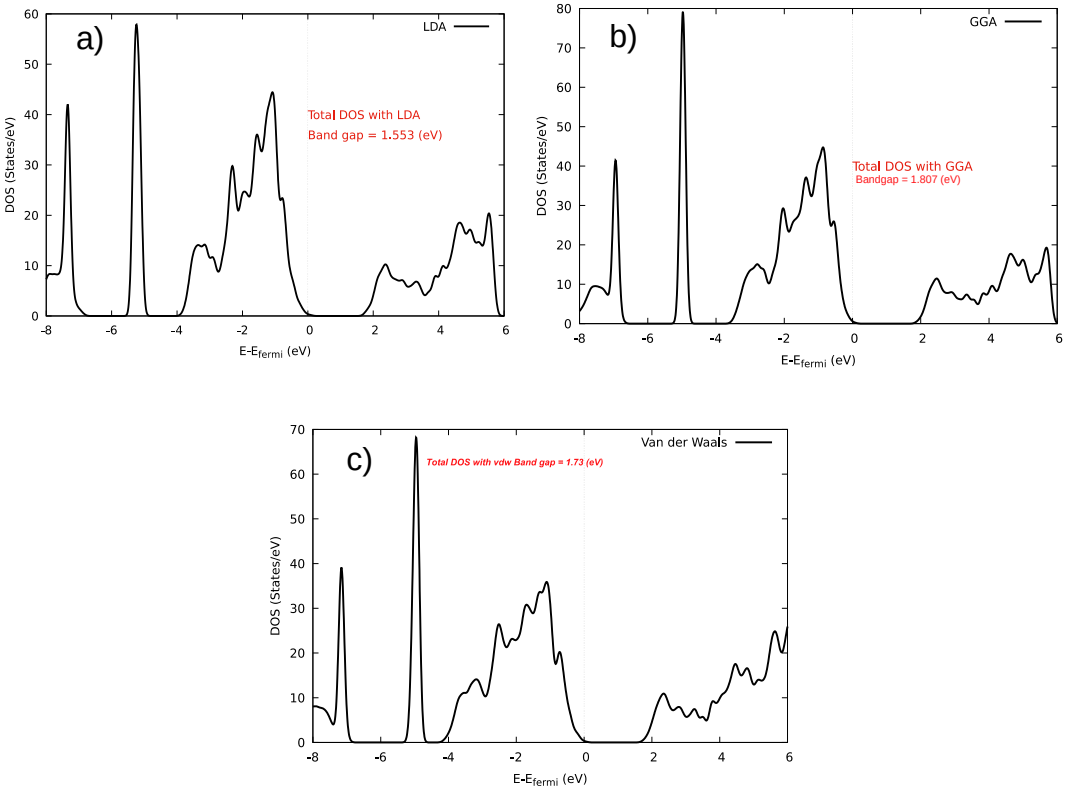

Figure 4.2: Total density of states (TDOS) of orthorhombic $CH_3NH_3PbI_3$ crystals and their band gap energies using different approximations. (a) total DOS by LDA, (b) total DOS by GGA, and (c) total DOS by Van deer Waals .

The stronger hybridization of the orbitals can shift the location of valence bands to the lower energy area with wider peaks. [96] Thus, the different PDOS images of I_1 and I_2 atoms indicate a weaker bonding between Pb and I_2 atoms. From Figure 4.3, it was found that organic $CH_3NH_3{}^+$ cations made little contribution to the top valence and bottom conduction bands around the Fermi energy level (-4.0eV<E-Fermi< 4.0 eV). The main contribution to the top valence band is from the I 5p states with an overlapping of $Pb^-6\,s$ states. In the bottom conduction bands, the main components are $Pb^-6\,p$ states. The PDOS images suggest that $(I-5\,p)$ electrons, especially the $(I_2-5\,p)$ electrons, can be photo-excited to $Pb-6\,p$ empty

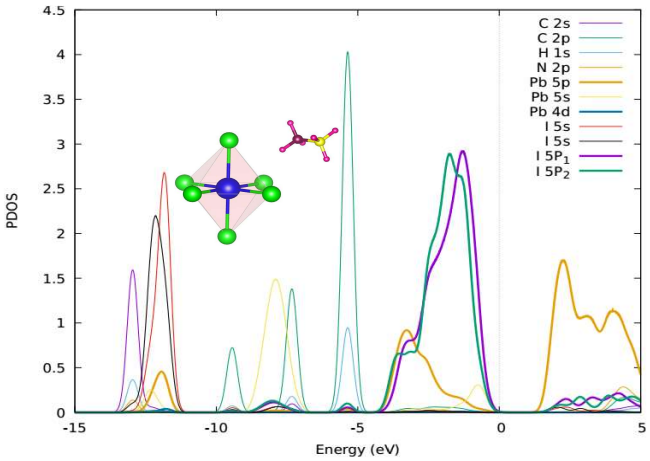

Figure 4.3: TDOS and partial density of states (PDOS) of atoms in orthorhombic $CH_3NH_3PbI_3$ crystals using the optB86b+ vdWDF functional The black and red tines indicate s and p states, respectively. The semicores of Pb atoms are treated as valence electrons i.e. valence electrons for $(Pb-5d^{10},6s^2,6p^2)$. The $(I-5s^2,5p^5)$, $(C-2s^2,2p^2)$, $(N-2s^2,2p^3)$ and $(H-1s^1)$ were considered as valence electrons.

states. Consequently, I atoms change into photo hole sites and Pb atoms hold the photo-electrons after the photo-excitation. From Figure 4.3, we also find that the highest C and N2 p bands and H$-$1 s bands locate at -6.8 and -4.8 eV, which shows little overlap with the Pb and I orbitals. Thus, there is no covalent interaction between the organic cations and the inorganic Pb $-$ I framework.

Approximation	$VanderWaals$	GGA	LDA	Exp [90]	$Calcul$ [92]
$Bandgap$	1.73	1.81	1.553	1.68-1.72	1.74

Table 4.2: The theoretical lattice constants and Pb$-$I bond lengths of orthorhombic $CH_3NH_3PbI_3$ in comparison with the experimental data .

The band structures of orthorhombic $CH_3NH_3PbI_3$ using different functionals are shown in Figure4.4. Our results agree with previous studies in showing that orthorhombic $CH_3NH_3PbI_3$

is a direct-bandgap crystal with the minimum band gap at the Γ symmetry point [97]. The minimum indirect bandgap is from the G point to the X point.

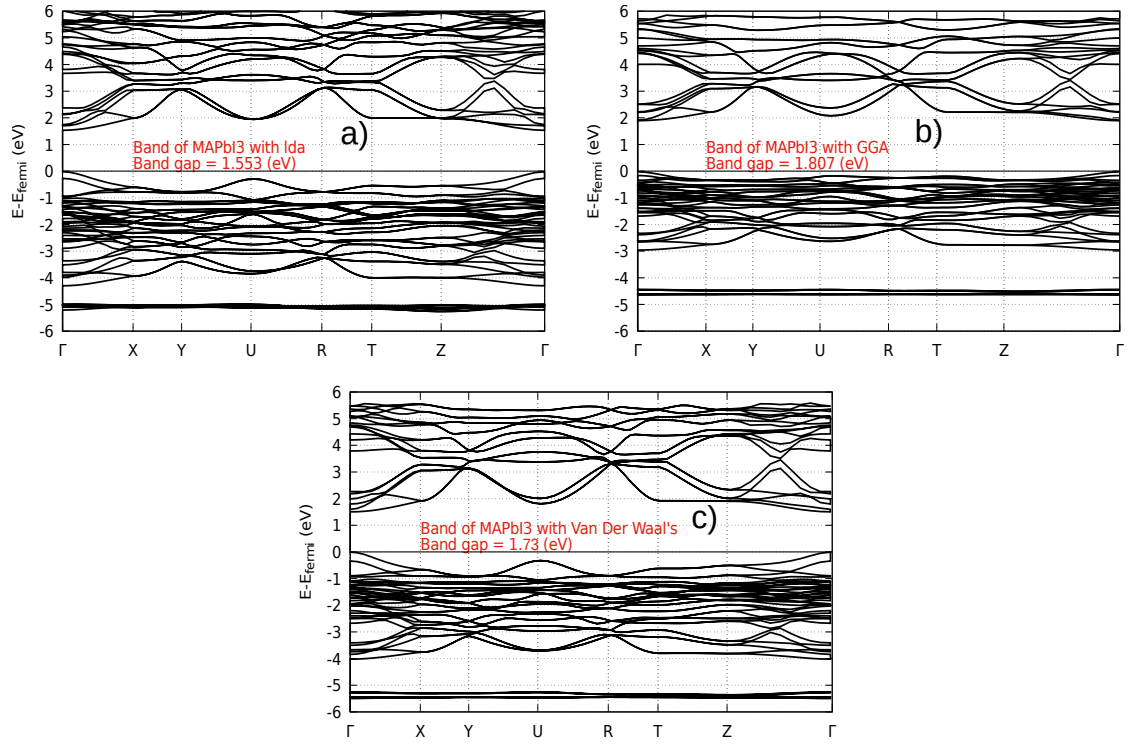

Figure 4.4: Calculated band structure of orthorhombic $CH_3NH_3PbI_3$ crystals along the high-symmetry tines in the first Brittouin zone where (a) bandstructure by LDA, (b) bandstructure by GGA, and (c) bandstructure by Van deer Waals.

For all band structures, several sets of bands can be found. They correspond to $\mathrm{C}-2\,\mathrm{p}$ and $\mathrm{H}-\mathrm{C}$ (the H atoms bonded to C atoms) $1\,\mathrm{s}$ states around -5 eV, mainly $\mathrm{I}-5\,\mathrm{p}$ states below the Fermi level and $\mathrm{Pb}-6\,\mathrm{p}$ states above the Fermi level. Both the top valence band and the bottom conduction band are broad, indicating that these states are non-localized. This explains why the excitons can be trans-ported to a long distance in this material. [98]' [99] Moreover, the fluctuations of the states in the bottom conduction band are stronger, indicating a faster transport of photoelectrons that matches the experimental observations. In contrast,

the band for organic fragments (the band around -5 eV) is flat and narrow, suggesting that the electrons around them are localized. It should also be noted that the band structure of the orthorhombic $CH_3NH_3PbI_3$ crystal is quite different from that of the cubic phase due to the lower symmetry and the bigger primitive cell. The main functional dependent properties are the locations of the bands, which confirm the conclusion from the analysis of DOS images. The Bader charges of Pb, I_1, I_2, N and C atoms in the orthorhombic perovskite $CH_3NH_3PbI_3$ crystals based on the pseudo valence density using different functionals. The $Pb-I$ covalent bonding characteristics can also be supported by the hybridization of the $Pb-6\,s$, $6\,p$ states with the $I-5\,p$ states at the top valence bands shown in Figure 4.3. Within $CH_3NH_3{}^+$ cations, the NH_3 group is almost charge neutral; and most of the positive charge is due to the contribution from the CH_3 group.

This charge distribution matches the chemical instinct because NH_3 is a charge neutral molecule and CH_3 is a positively charged cation in the gas phase. The charge distribution shown in Figure 4.3 indicates that there is a slightly stronger ionic interaction between the CH_3 group and I_1 atoms. From the PDOS analysis, it was found that there is a stronger $Pb-I_1$ covalent bonding. Thus, I_1 atoms have overall stronger interactions with their adjacent atoms, which explains why I_1 and I_2 atoms are chemically inequivalent, as observed in Figure 4.3. In the tetragonal and cubic phases, the symmetries of $Pb-I$ frameworks are improved due to the thermal movement of organic cations. [100] In those cases, the in equivalence of I atoms may be eliminated. A study on the thermal effect on the phase change and properties of $CH_3NH_3PbI_3$ materials is currently underway. Since the charge analysis using the all-electron (AE) reconstructed valence density could give more accurate results, the calculations based on the (AE) data using optB86B + vdWDF are also performed, as listed in Table 4.2. It can be seen that conclusions drawn from both sets of data are almost identical. The main difference is the charge of N atoms and the H atoms bonded with N atoms.

4.2.3 Transport properties:

Theoretical calculations predict very high orthorhombic mobilities: $\mu_e = [3032.7 - 12810.2]$ $cm^2V^{-1}s^{-1}$ and $\mu_h = [5383.01 - 8563.9]cm^2V^{-1}s^{-1}$ for the $MAPbI_3$ perovskites at charge carrier concentrations of $\sim 10^{17}\ cm^{-3}$. These values, very high compared to other hybrid or organic semiconductors, are of the same order of magnitude of crystalline inorganic semiconductors such as silicon or gallium arsenide. Calculations have shown that the large carrier mobilities mainly originate from a combination of two factors. The effective mass and temperature-dependent mobility for two different crystalline phases of $\mathrm{MAPbI_3}$, orthorhombic (below T = 160 K), show slightly better conductivity for electrons than holes, as shown in Figure 4.5 . Low effective masses are predicted, close to the values reported above, with slightly larger values for the orthorhombic phase and overall larger hole effective masses, consistent with lower predicted hole mobilities (orthorhombic: $m_e^* = 0.271m_0$, $m_h^* = 0.3351m_0$). Within the investigated temperature range (80-160 K), electron mobilities exceed hole mobilities by approximately a factor of two, and an increase by nearly one order of magnitude, for both electron and hole mobilities, is predicted below the phase transition temperature ($\mu_e = 6567cm^2V^{-1}s^{-1}$ and $\mu_h = 6837cm^2V^{-1}s^{-1}$ for the $\mathrm{MAPbI_3}$) for the orthorhombic phase. The effective mass and temperature-dependent mobility for two different crystalline phases of $\mathrm{MAPbI_3}$, orthorhombic (below T = 160 K), show slightly better conductivity for electrons than holes,($\sigma_e = 9.6 * 10^2\Omega^{-1}cm^{-1}$ and $\sigma_h = 1.4 * 10^3\Omega^{-1}cm^{-1}$ for the $\mathrm{MAPbI_3}$) as shown in Figure (4.5). The positive Seebeck coefficient argues for holes as the dominant type of charge carriers, but its non-monotonic temperature dependency indicates that electrons, whose temperature-dependent mobility differs from the one of holes, also participate in the charge transport.

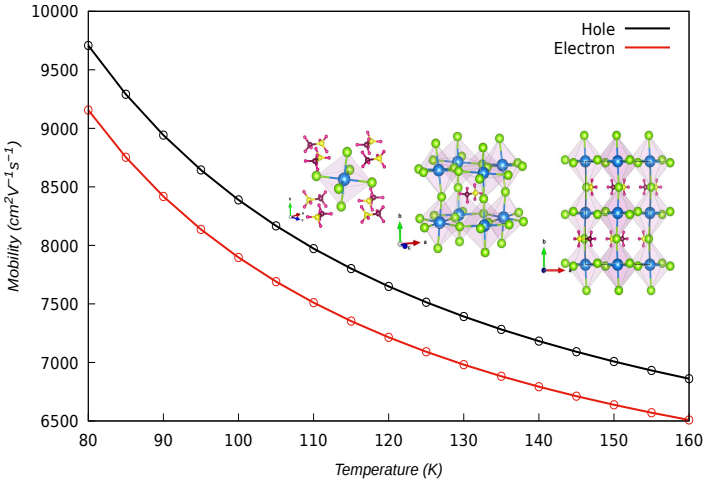

Figure 4.5: Calculated temperature dependence hole (black curves) and electron (red curves) mobility orthorhombic (T = 80-160 K) phases of $CH_3NH_3PbI_3$. The crystal unit cells of the two phases are shown as insets. Adapted and printed with permission from

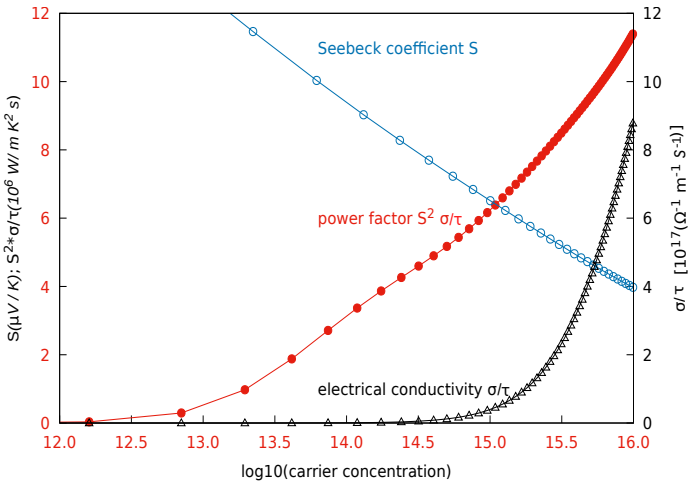

Figure 4.6: General relationship between Seebeck coefficient (S), conductivity ($\frac{\sigma}{\tau}$), and power factor ($S^2\frac{\sigma}{\tau}$) as a function of carrier concentration (n_c,). Curves generated based on $CH_3NH_3PbI_3$ and can be expected to change in shape and magnitude based on material system.

4.2.4 Strain Effects on the Electronic Band Structure:

$CH_3NH_3PbI_3$ crystallizes in the orthorhombic structure with space group $Pnma$ (No. 62) [101]at ambient conditions. The lattice constants of its unit cell are a, b and c. [3] C, N, H, Pb and I atoms occupy sites respectively see table (4.2). In order to simulate the interface misfit

N	$Element$		x	y	z	occupation	Wyckoff site
1	I	I_1	0.1865	0.01383	0.18556	1	$8d$
2	H	H_2	0.39555	0.31826	38481	1	$8d$
3	H	H_3	0.59173	0.314	0.58186	1	$8d$
4	Pb	Pb_4	0.5	0	0	1	$4b$
5	I	I_5	0.48258	0.25	-0.05115	1	$4c$
6	C	C_6	0.91185	0.25	0.04446	1	$4c$
7	H	H_7	0.33406	0.25	0.55344	1	$4c$
8	H	H_8	0.64777	0.25	0.42545	1	$4c$
9	N	N_9	0.93049	0.75	0.01491	1	$4c$

Table 4.3: The fractional atomic coordinates of C,N,H,Pb and I elements in orthorhombic-$MAPbI_3$ structure (Space group $Pnma$ (62)) .

strain, the $MAPbI_3$ unit cell model is employed and the biaxial isotropic tensile (compressive) strains are applied to $MAPbI_3$ unit cell along the [100] and [010] directions respectively as shown in Figure (4.7). Namely, the equivalent ϵ_{xx} and ϵ_{yy} strains are introduced along the directions of x and y axes respectively, where the lattice constants a and b of $MAPbI_3$ unit cell are constrained to several different values, differing from the equilibrium lattice constants by fractions ranging from -5% to +5% in the step of 1%. The perpendicular lattice

constant c is obtained by allowing all atomic positions to relax to a minimum energy. state under each strain.

For strain-free $\mathrm{MAPbI_3}$ unit cell, the calculated equilibrium lattice constants are $a = 8.807$ Å, $b = 12.611$ Å, and $c = 8.559$ Å, which are close to the experimental values of $a = 8.861$ Å, $b = 12.659$ Å, and $c = 8.581$ Å [**?**]. Once the equilibrium lattice constants are determined, the biaxial isotropic strains ϵ_{xx} and ϵ_{yy} will be imposed on $\mathrm{MAPbI_3}$ unit cell along the directions of x and y axes by equivalently constraining the lattice constants a and b. Then the biaxial isotropic strain is defined as Eq. (2.65):

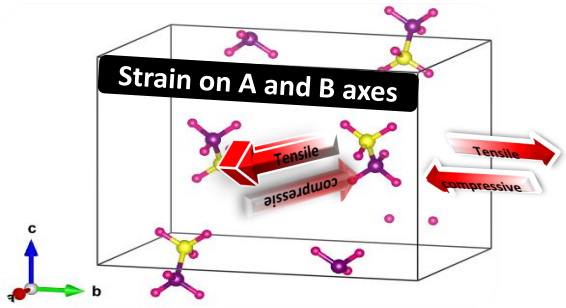

Figure 4.7: $\mathrm{MAPbI_3}$ unit cell model under biaxial isotropic strain. Tensile or Compressive arrows represent isotropic tensile or compressive strain ε_{xx}, ε_{yy} along x and y axes respectively.

4.2.5 Strain Effect on lattice structure:

This figure shows the extent of the strain effect on the lattice, especially with cation organic. We notice in part (a) the change in Orientation of cation N-C at (-5,0,5) points. And in part (b), we notice the shift of cation from their original place. This demonstrates the change in the structure band at the same points, and the overlap in the bands of valence and conduction.

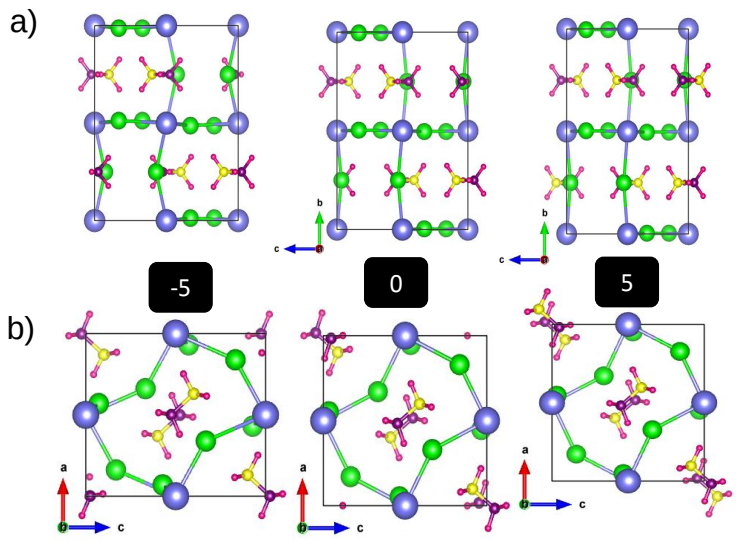

Figure 4.8: An atoms of lattice with strain (a) shows deviation in orientation for cation organic, (b) shows shifting in orientation for cation organic.

4.2.6 Band structure with strain:

As seen in the previous section, the disorder caused by the shifting and deviation in towards cation affected the band structure. This is clear at point -5 by the drop of the band-gap. We can see this drop is a result of the rotation and shift of the cation, and the cation organic approaching the iodine atom as noticed in the chart of charge distribution. The increase in the band structure to point 0, and then the decrease to point 5 as a result of shift and approximation of the iodine and copper atoms, as in figures (4.9) and (4.11).

4.2.7 Band-gap with Strain:

In the application of strain effect on $\mathrm{MAPbI_3}$ through compression or tension with the increase of 1%, we found a decrease in the band structure with compression of $\mathrm{MAPbI_3}$ from 1.73 eV to 1.48 eV and regarding the tension from 1.73 eV to 1.61 eV as shown in fig-

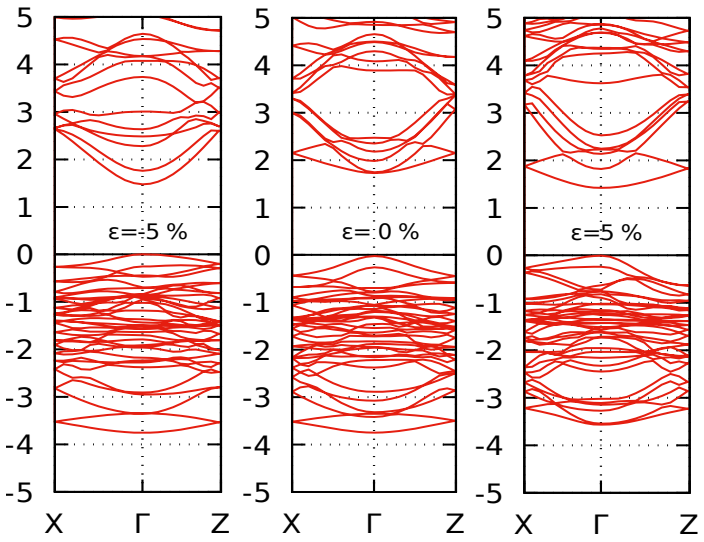

Figure 4.9: band-gaps in the (-5,0,5) points

ure (4.11). This decrease results from the shift and approximation of the iodine and copper atoms, as mentioned earlier.

$\xi(\%)$	-5	-4	-3	-2	-1	0	1	2	3	4	5
Band-gap (eV)	1.48	1.52	1.58	1.63	1.67	1.73	1.71	1.69	1.65	1.63	1.61

Table 4.4: The values of bands gap with percentage of strain effect.

4.2.8 Fermi Energy with Strain:

During the application of strain effort on $\mathrm{MAPbI_3}$ and with the change in the band-gap, especially in the connection band on $\mathrm{MAPbI_3}$, we noticed the change in the Fermi level with compression or. Yet, it is worth noting that during this compression, the shift of Fermi level towards the connection band indicates a change material type, particularly p-type to n-type, and with reserving the type p during the tension process and with making sure of this case,

we will study this broadly by focusing on the transport of this system. From the calculations, a clear change appear in the band connection in the process of compression, in contradiction to band valence, where pb is predominant as we noticed in figure 4.11. And here, we can see the clear role of copper Pb with cation in compression. Yet, in the case of tension we can see the key role of iodine and its strong connection with polyhedral.

4.2.9 Strain Effect on Charge Distribution:

We notice the overlap in the orbital between cation and the Iodine ions and we can also notice the overlap in the orbital between the cation and the ion and the overlap of I_1 with pb I_2 without strain effort, with clear overlap between I_1 with copper, and also breaking this overlap between cation and I_2 in the case of strain 5% Figure 4.10. The opposite happens with strain effect -5%, where we notice clear overlap in the orbital of the cation with I_2. And

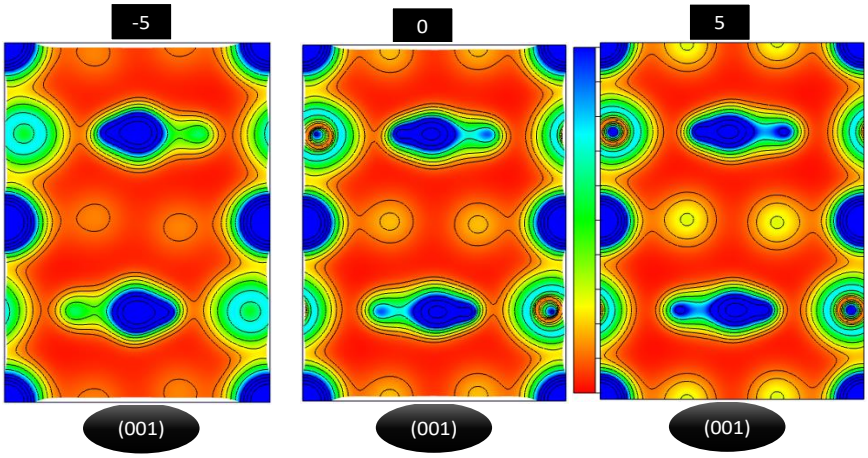

Figure 4.10: The difference in charge distribution -5) is overlap between cation ions with I_2 ions 0) is overlap between cation ions with I_2 ions, and overlap between I_1 ions with Pb ions 5) is overlap between I_1 ions with Pb ions

this explains at the same time the change of the band-gap mentioned earlier in part 4.3.3.

This clear difference in the change distribution plays a key role for the change process in the system n-type to p-type. The opposite happens with the increase and decrease of the carrier density of n or p, as we will see in the coming sections.

4.2.10 Electrical Conductivity, Carrier Density and Mobility:

Through the theoretical calculations, and using the DFT functional for studying the transport of this system, and also by using the Boltstrap Package; we arrived at many significant findings that confirm our previous findings. We focused on the electric conductivity, carrier density and mobility under strain effect (-5,0,5) , and behavior with this effect. We achieved

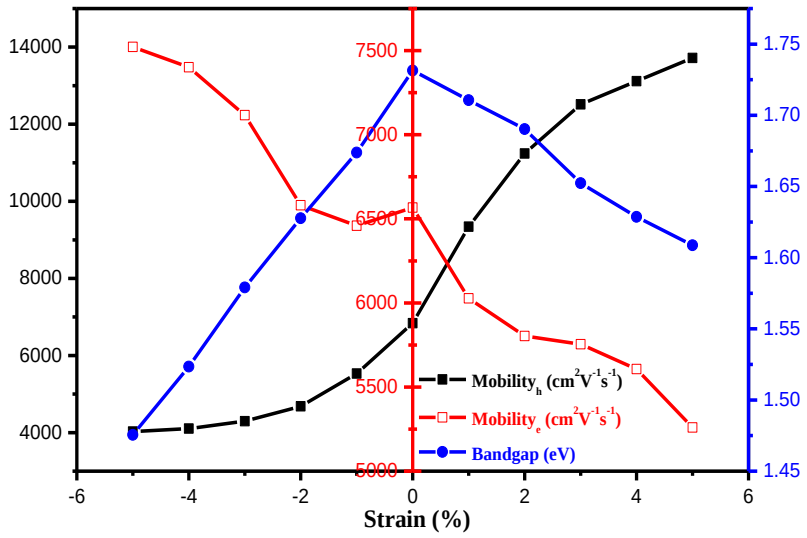

Figure 4.11: The predicted electron mobility varied with the strain based on the present calculations compared with that from the atomistic simulations.

different values for each variable, which all indicate a clear change in the behavior before and after the application of the strain effect, beside its change with the change of the strain level. To summarize, in table 4.5 we notice the increase in the hoe carrier density under strain effect from -5 to 5. On the contrary, there is decrease in the electron carrier density under

$\xi(\%)$	$p\ (\frac{1}{cm^3})$	$n\ (\frac{1}{cm^3})$	$\sigma_h\ (\frac{1}{\Omega*cm})$	$\sigma_e\ (\frac{1}{\Omega*cm})$	$\mu_h\ (\frac{cm^2}{V*s})$	$\mu_h\ (\frac{cm^2}{V*s})$
5	$1.39 * 10^{18}$	$1.29 * 10^{17}$	$3.1 * 10^3$	$8.0 * 10^2$	13719	5259
0	$1.3 * 10^{18}$	$9.13 * 10^{17}$	$1.4 * 10^3$	$9.6 * 10^2$	6837	6567
-5	$1.07 * 10^{18}$	$9.46 * 10^{18}$	$6.9 * 10^2$	$1.6 * 10^3$	4026	7522

Table 4.5: Carrier density, conductivity electric and mobility values under strain effect in (-5,0,5) points .

strain effect from –5 to 5 Figure 4.12. The same thing can be said about the conductivity and

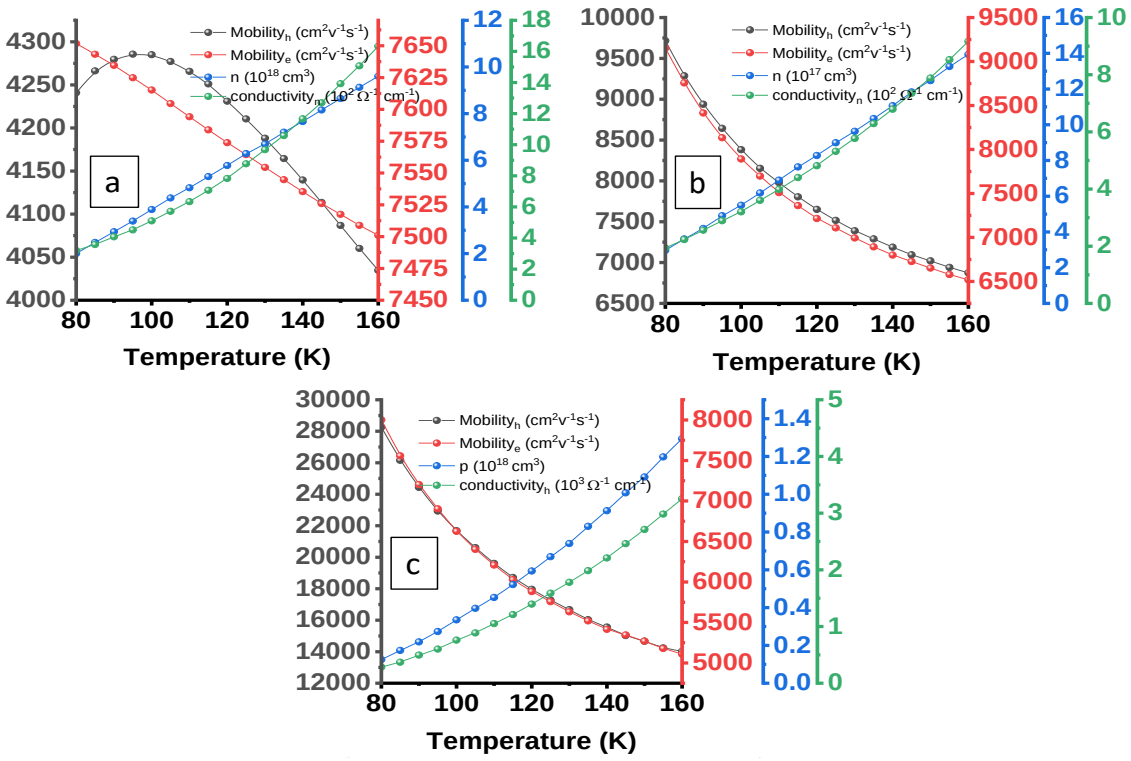

Figure 4.12: The predicted electron mobility varied with the strain based on the present calculations compared with that from the atomistic simulations where a- with (ϵ=-5), b- with (ϵ=0), and c- with (ϵ=+5) .

mobility. This confirms our conclusions in the previous sections about the change in the type

of system with strain effect. This is to say, the increase in the hole carrier density through the process of tension, means that the hole carrier density is responsible for the nobility in the system. The opposite happens with the compression where electron carrier density is responsible for the mobility as displayed in figure (4.11).

4.3 Conclusions

A novel mechanism for strain engineering the optical and electrical properties of orthorhombic hybrid perovskite $MAPbI_3$ have been proposed and demonstrated by using simple strain conditions. Firstprinciples simulations reveal that appropriate strain (5%) tensile or compressive; the conduction type can be rotated from n-type to p- type and vice versa, depending on the kind of process (tension or compression). This strain effect on the optical and electrical properties of OHP $MAPbI_3$ will be useful for exploring unusual optical and electrical effects and exotic electronic and photovoltaic cells applications based on Perovskite $MAPbI_3$

CHAPTER 5

Enhanced photocatalytic activity

5.1 Introduction

The increasing demand for energy and the deleterious environment impact resulting from the use of fossil fuels, urged the policy makers and the scientists to heavily look for alternative renewable energy production [102]. One of the most exciting research topics in the field of energy harvesting, nowadays, is the use of solar energy to produce green hydrogen (H_2) considered as a desirable energy vector [77, 103]. The pioneering work of Fujishima and Honda on solar-driven water splitting (WS) into H_2 and oxygen (O_2) using a titanium oxide (TiO_2) as photoanode, has triggered researchers to investigate novel strategies to produce and store clean H_2 [63, 79, 104, 105]. A major challenge is that the hydrogen-evolution reaction (HER) catalysts require complex materials with various functional properties, such as increasing surface area, high ions permeability, appropriate redox energy levels for the conduction and valence bands with respect to the WS potentials . During several decades, various semiconductors and molecular assemblies have been reported to achieve photocat-

alytic WS such as Ta_3N_5, CdS, ZnS, ZnO, TiO_2 among others [63, 79, 104, 105],. In view of the solar energy utilization and considering the surface overpotential, an ideal photocatalyst should possess a suitable bandgap of around 1.83 eV in the $2D$ state and band alignment with WS redox to better harvest the full sunlight spectrum and transform the absorbed solar energy into H_2 [106]. In the search for chemically stable and earth-abundant visible-light-driven photocatalysts, hybrid organic-inorganic perovskites such as methylammonium lead iodide perovskite, with the chemical formula $CH_3NH_3PbI_3$ (mostly known as $MAPbI_3$), has shown a great absorption coefficient (104-105 cm^{-1}) and an interesting optical bandgap (1.74 eV) that allows absorbing the visible light within wavelengths ranging from about 280 nm to 800 nm [107, 108]. Additionally, $MAPbI_3$ exhibits excellent electronic properties such as an ambipolar charge transport and long charge diffusion length ($\sim$ 25μm in $MAPbI_3$ single crystals) and thus has advanced the conversion power efficiency of new-generation solar cells to over 20 % in the last 10 years [109]. These attractive properties enabled $MAPbI_3$ to be a desirable candidate for photocatalytic HER, where its catalytic activity and durability have been promoted significantly since the pioneering work on $MAPbI_3$ in 2016 [65,110]. Nevertheless, $MAPbI_3$ materials still suffers from instability in the presence of water [111]. Besides, the holes generated in the $MAPbI_3$ valence band are unable to move through the electrolyte because they do not generate enough potential to produce OH^-. In fact, previous studies have reported on the interfacial electronic properties of coupled $ZnO:Al/MAPbI_3$ [50, 52, 112]. In this work, $MAPbI_3$ is investigated as a potential photocatalyst for HER through WS reaction using a $ZnO:Al/MAPbI_3/Fe_2O_3$ heterojunction model achieving the z-scheme photocatalysis mechanism.

5.2 Results and Discussion

Metal Halides, generalized by the chemical formula of ABX_3 ($A = CH_3NH_3, CHN_2H_4, ...$; $B = Sn, Pb, ...; X = I, Br, ...$), have versatile and unique properties that widen their range of applications. Particularly, $MAPbI_3$ (MA= methylammonium or $CH_3NH_3^+$) perovskites have emerged as one of the best performing photoanode materials due to their high absorption (1.4 a.u.), suitable bandgap of 1.73 eV for bulk $MAPbI_3$ and low production cost [113]. However, the position of their valence band (VB) relative to the redox potential of the water oxidation still hinders their performance for H_2 photocatalytic production. In such materials, electrons in the VB are excited to the conduction band (CB) by light irradiation with an energy equivalent to or larger than the material's bandgap, subsequently electron-hole pairs are formed. These latter contribute directly to the reactions of reducing protons to generate H_2 and oxidize H_2O to produce O_2, respectively. To facilitate the WS reaction, the bottom of the CB and the top of the VB must be respectively lower and higher than the reduction/oxidation potentials of H^+/H_2: 0 V vs. normal hydrogen electrode (NHE) at pH nil and O_2/H_2O (1.23 V vs. NHE), respectively [114]. In what follows, we will attempt to engineer the band edge potentials of $MAPbI_3$ by coupling its side surfaces with Fe_2O_3 and $ZnO : Al$ while keeping its band gap within the visible region Fig 5.3. It is worth noting that, designing efficient z-scheme devices requires clarifying the interfacial properties and the ability to discern the physics behind the competing mechanisms. While the theory of semiconductor electrolyte interfaces has been well developed, it has not been rigorously expanded to accommodate double semiconductors and co-catalyst on their z-scheme surfaces [115]. In addition to exploring the improvement of the mechanism of H_2 generation using $MAPbI_3$ based photocatalyst, one can notice that coping with its surface degradation and finding a mechanism

for generating holes to activate the oxidation process through the z-scheme [116] could help to build an efficient reported experimentally elsewhere [117, 118].

5.2.1 Heterostructure Fabrication and Interface Electron Extraction:

5.2.1.1 $MAPbI_3$ (001)/Fe_2O_3 (110) z-scheme:

As mentioned above, one of the major challenges with $MAPbI_3$ in photocatalysis is the edge position of its valence band (1.15 V) lower than the oxidation energy of water oxidation redox (1.23 V), required to achieve WS. For $MAPbI_3$, the holes do not have enough energy to achieve this process, hence we first simulate the composition of $MAPbI_3$ coupled with Fe_2O_3 which was found to have the sufficient bandgap for WS as the oxidation (1.23 V) and reduction (0 V) potentials of $MAPbI_3$ (001)/Fe_2O_3 (110) are within the desired reduction (0 V vs. NHE at pH=0) and oxidation (1.23 V $vs.$ NHE at pH=0) WS potentials. The introduction of Fe_2O_3 allows to obtain a z-scheme composition leading to an increasing light absorption, as will be discussed later, with a rise in the formation of electron-hole pairs, which in turn increased the number of split H_2O molecules into HO^- and H^+ ions leading to H2 production. To assess the stability of the established heterostructure, we have calculated the binding energy ($E_{binding}$) of the $ZnO:Al/MAPbI_3/Fe_2O_3$ composition using the following equation:

$$E_{Binding}^{A/B/C} = \frac{E_{tot}^{A/B/C} - (E_{tot}^{A} + E_{tot}^{B} + E_{tot}^{C})}{Surfacearea(^2)} \tag{5.1}$$

where $A = ZnO:Al$, $B = MAPbI_3$, and $C = Fe_2O_3$. The heterostructure AB and BC have found to be stable with a calculated $E_{binding}$ value of 3.64 and 3.94 $V/^2$ respectively. The binding energy is calculated by varying the interlayer distance between the monolayers constituting the heterostructure by taking into consideration the van der Waals interac-

tions in the form of vdW-optB86b Fig 5.1 As can be seen in Fig **??**, binding energies of

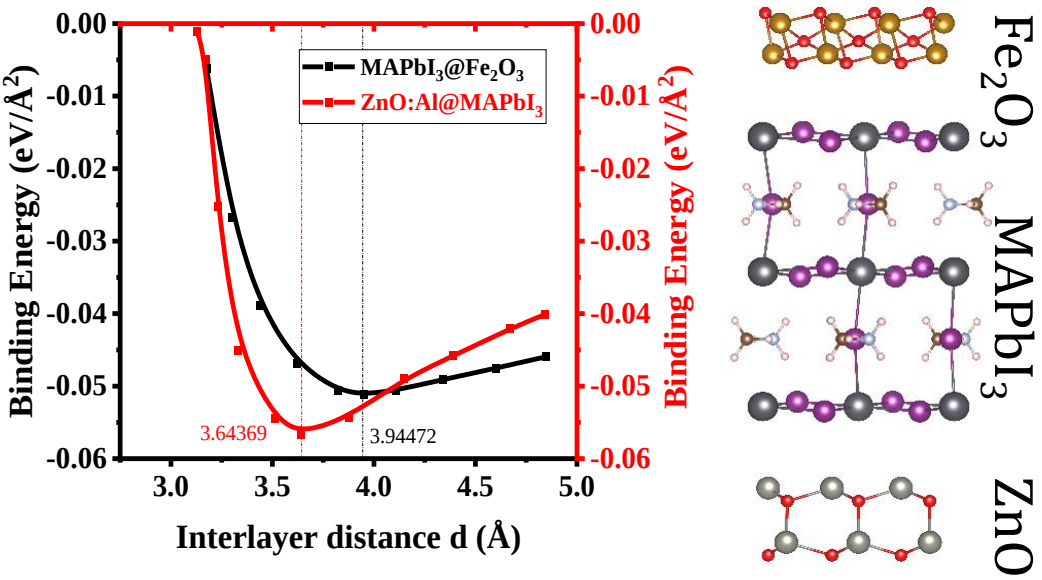

Figure 5.1: Variation in the interlayer binding energies, calculated using vdW-optB86b, with interlayer distance, d (Å), in $ZnO : Al/B = MAPbI_3$(3.64369 Å), and $B = MAPbI_3/C = Fe_2O_3$ (3.94472 Å) heterobilayers..

$ZnO : Al/MAPbI_3$ and $MAPbI_3/Fe_2O_3$ heterostructures are found to achieve -0.05665 and -0.05116 $eV/$, respectively at the vdW minima of $ZnO : Al/MAPbI_3$ (3.64369 Å), and $MAPbI_3/Fe_2O_3$ (3.94472 Å) suggesting that the process of heterobilayer build-up is exothermic. Moreover, it is worth noting that the obtained binding energy is high with respect to the typical vdW crystal of graphite (-0.012 eV/ Å2). [119]

5.2.1.2 $ZnO : Al$(001)/$MAPbI_3$(001) z-scheme and $ZnO : Al/MAPbI_3/Fe_2O_3$ Heterojunction:

Moreover, we have coupled its surface with $ZnO : Al$ to facilitate the process of attracting electrons from the CB of $MAPbI_3$ and transferring it to the H_2 reduction potentials. Ad-

ditionally, $ZnO:Al$ is also known to be a transparent material [112, 114, 120] that allows light radiation to reach $MAPbI_3$ and protects it from deterioration in the presence of H_2O. For $MAPbI_3$, our findings show that the CB electrons are mainly composed of $Pb-5p$ orbitals and hybridized between $Pb-5s$ and $I-5p$ in VB [93]. The top of the VB (1.15 V $vs.$ NHE) takes a much smaller position than 1.23 V $vs.$ NHE as illustrated in Fig **??**a. Therefore, it is not possible for the redox process for H^+/H_2 and O_2/H_2O to occur because the bottom of the CB is found at -0.64 V vs. NHE. On the other hand, the VB for Fe_2O_3 consists of strongly hybridized $O-2p$ and $Fe-3d$ orbitals [121]. The CB is, however,

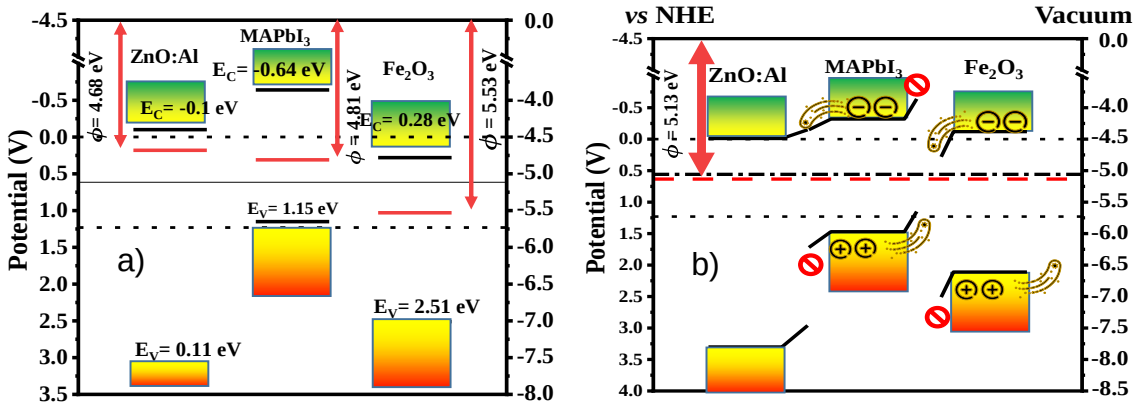

Figure 5.2: A schematic diagram of band edge potentials for a) freestanding $ZnO:Al$, $MAPbI_3$, and Fe_2O_3 and b) $ZnO:Al/MAPbI_3/Fe_2O_3$ heterostructure where ϕ denotes the work function.

dominated by $Fe-3d$ states, as shown by core-level absorption measurements. Some covalent mixing of the metal andO_2 states exists also in the CB and introduces a degree of O-2p character in unoccupied states. It is also known that ZnO is a direct bandgap semiconductor with a bottom CB and top VB located at the same Γ point of the Brillouin zone. VB and CB are mainly composed of $Zn-3d$ and $O-2p$ states [48], respectively, and the corresponding calculated bandgap is of 3.21 eV, in good agreement with the experiment [120]. When doping ZnO with Al, the Fermi level slowly upshifts towards the conduction band as

a function of the concentration of Al, indicating its n-type nature, until a semiconducting-metallic transition occurs at the value of 12% [113]. Such behavior has been reported for other materials using different bandgap engineering pathways [114]. In our calculations we will only focus on doped $ZnO : Al$ with a concentration of 2% which was consistent with our other calculations, as it confirmed how electrons migrate between the layers ZnO and $MAPbI_3$ after contact, as well as the Fermi level of $ZnO : Al$ with that of the Fermi level of redox. Additionally, we have studied the energetic stability of different surface planes for the three materials and then we have chosen the most stable ones, namely (110), (001) and (001) for Fe_2O_3, $ZnO : Al$ and $MAPbI_3$ respectively. These surface planes are identical to other studies [112, 115, 122]. The photocatalytic efficiency of water splitting is defined by the positions of the photocatalyst's band edges (e.g., Figure. 3). The VB and CB potentials of the Fe_2O_3 (110), $ZnO : Al$ (001) and $MAPbI_3$ (001) monolayers are calculated using the following empirical equations:

$$\begin{cases} E^0_{CB} = \chi - E^0 - \frac{1}{2}E_g \\ E^0_{CV} = E^0_{CB} + E_g \end{cases} \tag{5.2}$$

where E^0 is the energy of free electrons on the hydrogen scale (0 V), is the absolute electronegativity of the semiconductor, E^0_{VB} is the valence band maximum, E^0_{CB} is the conduction band minimum, and Eg is the bandgap. The values for Fe_2O_3, $ZnO : Al$ and $MAPbI_3$ are 5.53, 4.68, and 4.81, respectively, which were calculated by the Millikan approximation that is demonstrated by previous reports [123, 124] to be suitable for calculating the band edge potentials equations:

$$\begin{cases} \chi(S) = \sqrt[n]{\chi_1^{Z_1}\chi_2^{Z_2}\chi_3^{Z_3}.....\chi_n^{Z_n}} \\ \chi_i(S) = \dfrac{E_i^{IE} + E_i^{AE}}{2} \end{cases} \tag{5.3}$$

where E_i^{IE} is the ionization energy, E_i^{AE} is the affinity energy, N is the total number of atoms in the compound, $\chi_n^{Z_n}$ are the electronegativity of the constituent atom, Zn are the number of

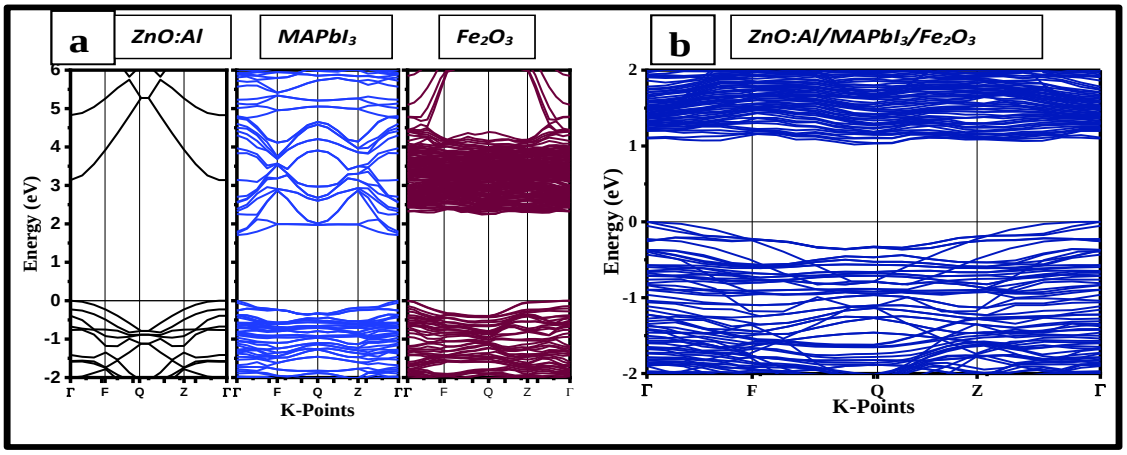

Figure 5.3: Calculated energy band structures of (a) freestanding $ZnO:Al$, $MAPbI_3$, and Fe_2O_3 respectively and (b) $Fe_2O_3/MAPbI_3/ZnO:Al$ heterostructure based on GGA-PBE. The Fermi level is set to be 0 eV and denoted as a black line.

species, and $\chi_i(S)$ is the electronegativity of the elements. According to Table 1, before the coupling of Fe_2O_3 and $ZnO:Al$ with $MAPbI_3$, the calculated band edge positions of the CB and VB for the $MAPbI_3$ (001) surface are found to be: -0.64 V and 1.15 V vs. NHE, respectively, and the bandgap is 1.79 V. Our calculated results reveal that the Fe_2O_3(110) surface has a band edge position of 0.28 V (CB) and 2.51 V (VB) vs. NHE, resulting in a bandgap of 2.23 V. Likewise, the $ZnO:Al$ (001) surface exihibits a band edge position of -0.1V (CB) and 3.11 V (VB) vs. NHE, giving rise of a bandgap of 3.21 V, respectively. After coupling of the Fe_2O_3 and $ZnO:Al$ systems with $MAPbI_3$ to form the heterostructure, the fermi levels of $MAPbI_3$ (001) and $ZnO:Al$ surfaces will upshift by 0.32 V and 0.45 V, respectively, while that of Fe_2O_3 monolayer will downshift by 0.40 V vs. NHE. Until the Fermi levels of the two components reach the same level (Figure 2b), hence a built-in electric field is formed on the interface from the Fe_2O_3 (110) monolayer to the $MAPbI_3$ (001) surface, as shown in Figure 2b.

$Materials$	$ZnO:Al$	$MAPbI_3$	Fe_2O_3	$ZnO:Al$	$MAPbI_3$	Fe_2O_3
ϕ	4.68	4.81	5.53	5.13	5.13	5.13
$E_g(eV)$	3.21	1.79	2.23	3.21	1.79	2.23
$E_F(eV)$	0.18	0.31	1.03	0.63	0.63	0.63
$E_{CV}(eV)$	3.11	1.15	2.51	3.3	1.48	2.11
$E_{CB}(eV)$	-0.1	-0.64	0.28	-0.01	-0.31	-0.12

Table 5.1: Calculated work function (ϕ), band gap (E_G), Fermi level (E_{FERMI}), conduction (EC) and valence (EV) edge positions for freestanding $ZnO:Al$, $MAPbI_3$ and Fe_2O_3 before coupling and the $ZnO:Al/MAPbI_3/Fe_2O_3$ heterostructure after coupling. All values are calculated $vs.$ NHE .

To determine the energy required for the electrons to escape from the Fermi level into a vacuum for heterostructure, we need to calculate a work function ($\phi = 5.13eV$) that is expressed as the difference between the vacuum and the minimum energy required for electrons to escape from the Fermi level. Moreover, we found the potential energy of $ZnO:Al/MAPbI_3/Fe_2O_3$ after contacting in the Z direction, and Fermi level position E_F=- 5.13 eV from the vacuum (Figure 5.4).

5.2.2 Water splitting mechanism :

To better understand how the modeled heterostructure operates in contact with water under the visible light irradiation, we have evaluated its stability and band gap alongside with the CB and VB edges for each system and calibrated them with the WS potentials as illustrated in Figure 5.2. After coupling the three materials into one compound, we have calculated the electrostatic potential through the Fermi level of the composition with respect to the vacuum and observed that there is a shift of the Fermi level and energy bands due to the migration

of the electrons between the three systems in quest for stability. This is mainly caused by the difference in electronegativity and chemical potentials as shown in Figure 5.4a. The

	$\sum Q \ \|e\|$	$N_{D,N}$ $(\frac{1}{cm(3)})$
$MAPbI_3/Fe_2O_3$	-0.52	$3.325 * 10^{18}$
$ZnO : Al/MAPbI_3$	0.15	$1.1875 * 10^{18}$

Table 5.2: Charge transfer $\sum Q$ and number of donor and acceptor electrons ($N_{D,A}$) within $MAPbI_3$ / Fe_2O_3 and $ZnO : Al$ / $MAPbI_3$. $\sum Q$ value for A/B denotes electron transfer from A to B while a negative one represents the opposite .

yellow region represents charge accumulation, whereas the blue region represents charge depletion. Charge redistribution occurred mostly at the ZnO/$MAPbI_3$/Fe_2O_3 contacts. The

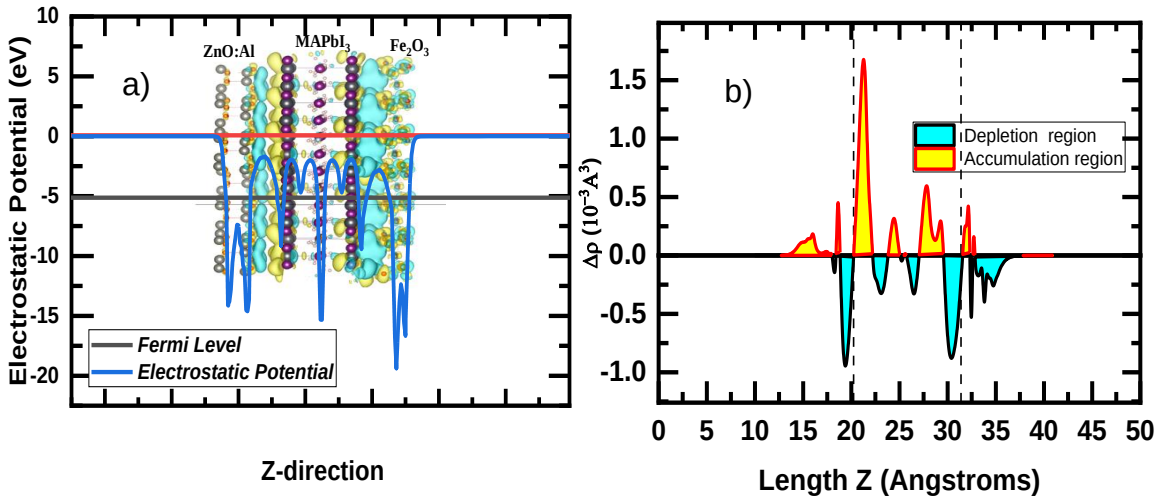

Figure 5.4: 3D charge density difference for (a) ZnOAl/$MAPbI_3$ and $MAPbI_3$/Fe_2O_3, (b) Planar-averaged electron density difference $\Delta\ \rho$ (z) for Fe_2O_3/$MAPbI_3$/ZnO.

weak vdW interaction between Fe_2O_3, $MAPbI_3$, and ZnO was mainly responsible for this result. Figure 5.4b is shown the planar-averaged charge density differential along the Z di-

rection. The change of charge density at the ZnO/$MAPbI_3$/Fe_2O_3 interfaces revealed that electrons mostly transferred from ZnO to $MAPbI_3$ and subsequently to Fe_2O_3 through the interfaces, whereas holes stayed on the ZnO and $MAPbI_3$ sides. In quantifying the charge change and transfer, Bader charge analysis was performed for the charge densities of the ZnO/$MAPbI_3$/Fe_2O_3 heterostructure. The results pointed out that about 0.15 e and 0.52 e charge transferred from ZnO to the $MAPbI_3$ (001) slab at the ZnO/$MAPbI_3$ (001) interface and transferred from $MAPbI_3$ to the Fe_2O_3 (110) slab at the $MAPbI_3$/Fe_2O_3 (001) interface. To elucidate the shifting process in the energy bands, we carried out a Bader charge analysis that will indicate the migration of electrons within the three systems [125]. After coupling, the Fermi level of Fe_2O_3 up shifted while those of $MAPbI_3$ and $ZnO : Al$ downshifted to reach an equilibrium point for the whole system. According to the charge transfer values summarized in Table 5.2, it can be seen that electrons have migrated from $MAPbI_3$ towards Fe_2O_3, while electrons have moved from $ZnO : Al$ towards $MAPbI_3$. A mechanism of WS, based on the light irradiation with energy equals or greater to the photocatalyst band gap energy produces an oxidative and reductive entity. In its first step, photo-generated hole-electron pairs are formed in the VB h_+ and the CB e_-, respectively. Consequently, these photogenerated charge carriers will react with water or dissolved oxygen to produce reactive oxidizing species such as HO^- and O_2^-. In our model consisting of three coupled materials, the initial objective is to improve the performance of $MAPbI_3$ in the photocatalytic process and stop its degradation caused by water molecules. When the heterostructure is exposed to illumination, a hole-electron pair is generated in the valence band and electrons start moving to the conduction band of $MAPbI_3$ and Fe_2O_3. When the three systems are coupled, an internal electric field is created at the contact surfaces between $MAPbI_3$ and Fe_2O_3 due to the difference in potentials which then alters the trajectories of charge carriers within the heterostructure. At the contact surfaces, an energy barrier is generated due to the movement

of the Fermi level preventing the transfer of charge carriers between $MAPbI_3$ and Fe_2O_3, while leading electrons have moved from $MAPbI_3$ to $ZnO : Al$ and then towards the reduction potential. While on the other hand, holes cannot move from Fe_2O_3 to $MAPbI_3$ due to the presence of an energy barrier between them, which makes them move towards the oxidation potential. The photocatalytic activity of the heterostructure model appears very well located in the NHE where the heterostructure is found to be suitable for photocatalytic H_2 production at pH = 0 based on water calculated oxidation and reduction potentials. Even after immersing the heterostructure in a neutral solution with pH = 7, it is still suitable for WS as displayed in Fig 5.2, but the production of H_2 is slightly greater than the amount of hydrogen ions H^+ generated at the edge of the oxidation potentials where the concentration of holes ($p = 6.53 * 10^{10} cm^{-3}$) is smaller than the concentration of electrons ($n = 5.86 * 10^{12} cm^{-3}$) for the heterostructure. In order to improve the potential edges and neutrality in the process of generating positive ions and efficiently producing H_2, we have increased the acidity degree. This study suggests using the heterostructure as a photocatalyst in an acid solution ($pH \leq 7$), with the surface coated with $ZnO : Al$ as a visible-light transparent material to maintain the electronic, optical and photocatalytic activity of the clean surface of the heterostructure. The potential edges in the presence of acidic pH were calculated by the following equation:

$$E_{CB,CV} = E^0_{CB,CV} - 2.3 K_B T \Delta pH \tag{5.4}$$

5.2.3 production yield of H_2 :

The calculated production yield of H2 is shown in Figure 5.5. Pristine $MAPbI_3$ demonstrates moderate catalytic HER from hydrogen iodide acid (150 $\mu mol/g$) which is similar to other works [119, 126]. For the $ZnO : Al/MAPbI_3/Fe_2O_3$ composition, the photocatalytic activity has been significantly improved to yield to 151.08 $\mu mol/g$ as shown in Figure 5.5.

It is worth noting that the H_2 yield rate for $ZnO : Al/MAPbI_3/Fe_2O_3$ proportionally in-

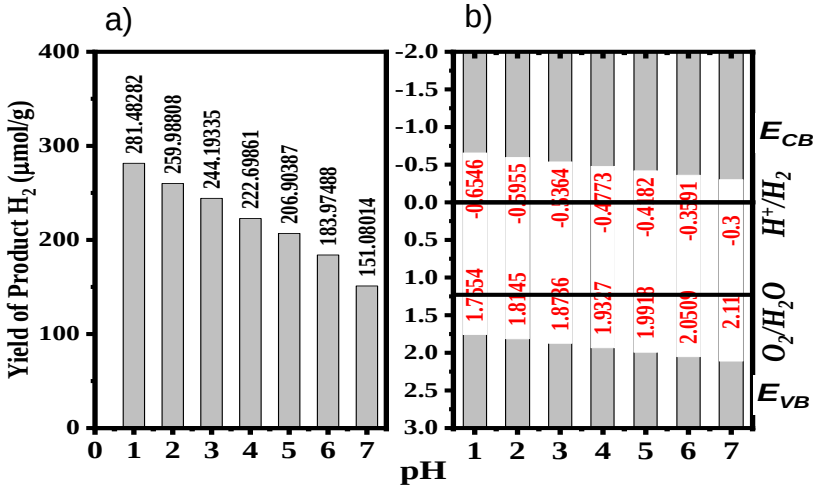

Figure 5.5: Photocatalytic performance of $ZnO : Al/MAPbI_3/Fe_2O_3$ in H_2 evolution from H_2O splitting. (a) Photocatalytic H_2production rate with different pH (1-7). (b) Energy levels of conduction band and valence band with different pH (1-7).

creased with the decreasing of pH. Moreover, with continuous reaction at pH = 5, the H2 yield rate for $ZnO : Al/MAPbI_3/Fe_2O_3$ reaches 281.48 $\mu mol/g$, which is larger than the value obtained with pH = 7 of reaction and is even superior to most of the reported works on pristine $MAPbI_3$ [118]. In this part, we assumed the device shown in Figure 5.6. Where we calculated the current flowing in the circuit by using equations from 1 to 3 shown in the computational methods.

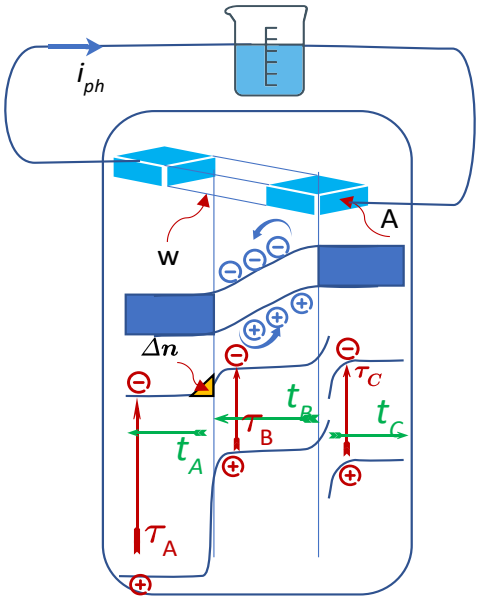

Figure 5.6: A hypothetical diagram showing the movement of electrons and holes and the current I_{ph} passing through them.

5.2.4 Thermal stability:

Molecular dynamics simulations were performed to investigate the deposition behavior of the specific surface of Fe_2O_3 or $ZnO:Al$ loaded to $MAPbI_3$ (001). Geometric optimization was carried out for the three materials where the planar surfaces are modified until the total energy of the individual structure reaches a minimum potential corresponding to the local minimum in the potential energy surface. In our calculations, Fe_2O_3 and $ZnO:Al$ were deposited on a $MAPbI_3$ (001) surface to detect the lowest energy absorption sites with their appropriate composition. Both materials appear to adequately stick to the $MAPbI_3$ (001) surface without causing deterioration to the material as shown in Fig 5.7. All three materials have maintained their structural properties with increasing temperature up to 300 K. A transformation of $MAPbI_3$ (001) phase from an orthorhombic to a cubic structure at

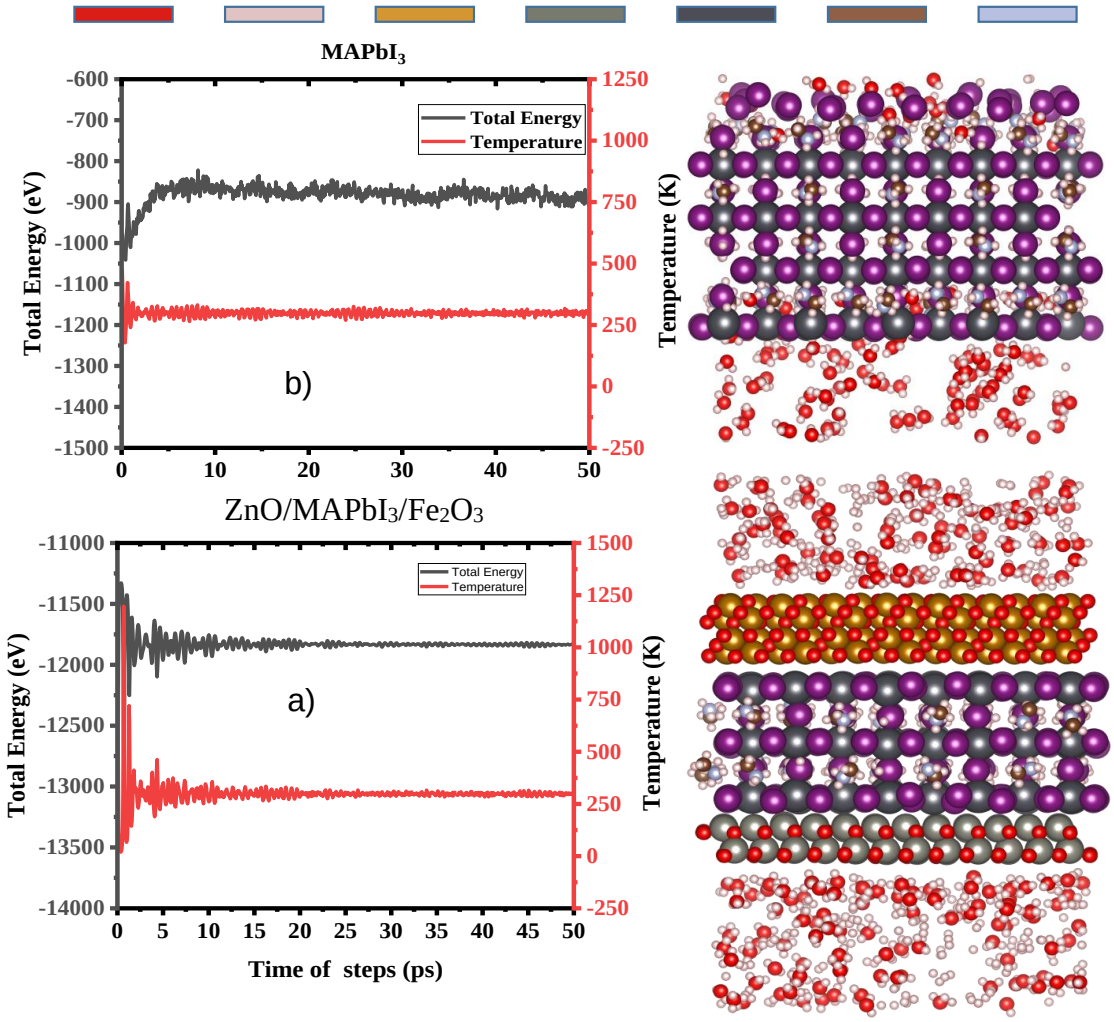

Figure 5.7: The fluctuations of energy and temperature for (a) $ZnO/MAPbI_3/Fe_2O_3$ heterostructure and (b) $MAPbI_3$ (001) surface in a solution of H_2O, HO^-, H_3O^+, and H^+ molecules. Snapshots were taken at 50 ps from AIMD simulations at 300 K..

300 K, which is in total agreement with reported experimental results [70]. When $MAPbI_3$ is immersed in water, we noticed deterioration in the contact surface with water (Fig 5.7b), which is not the case when the $ZnO : Al/MAPbI_3/Fe_2O_3$ heterostructure was immersed in water. This demonstrates clearly the extent of improvement in preserving $MAPbI_3$ (001) from degradation in the heterostructure form (Figure 5.7a). Additionally, no contact was observed between the H_2O molecules and HO^- and H_3O^+ions in the solution with $MAPbI_3$ (001) surface. These findings open the door for discovering more suitable solutions to cope with the degradation of $MAPbI_3$ (001) in the presence of oxygen or water.

5.2.5 Optical Properties:

Light absorption was used to evaluate the performance of the investigated photocatalyst. The absorption spectrums of the freestanding Fe_2O_3, $MAPbI_3$ and ZnO:Al systems were simulated. The results show that $MAPbI_3$ has a strong light absorption (1.4 a.u.) in the visible light region, but weak light absorption in the UV region (300-500 nm) as shown in Figure 8. After coupling, the light absorption capacity of the ZnO:Al /$MAPbI_3/Fe_2O_3$ heterostructure in the UV region was much improved (1.62 a.u.) in comparison to that of freestanding $MAPbI_3$ while the visible light absorption was maintained. Besides, as expected the $ZnO : Al$ spectrum in the UV region is showing high transparency, thus, allowing for the visible spectrum to reach $MAPbI_3$ which explains why the excellent absorption obtained in the visible light was not altered. Thus, the absorption was calculated according to the following equation:

$$A(hv - E_g) = (\alpha hv)^{\frac{1}{n}} \tag{5.5}$$

where α is the absorption index, h is the Planck constant, ν is the frequency, A is the constant,$E_g$is the bandgap width of semiconductor, and the exponent n is related to the semi-

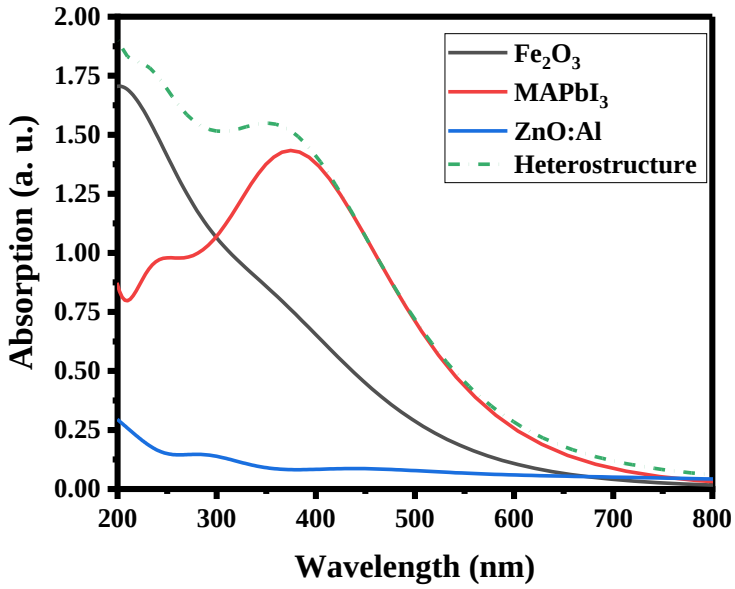

Figure 5.8: Calculated optical absorption spectra of Fe_2O_3 (110), $MAPbI_3$ (001), $ZnO:Al$ (001) surfaces and $ZnO:Al, MAPbI_3, and Fe_2O_3$ heterostructure.

conducting type: $n = 1/2 or 2$ for a direct or indirect bandgap, respectively. Freestanding $ZnO:Al$ and $MAPbI_3$ are semiconductors with a direct bandgap ($n = 1/2$) while Fe_2O_3 has an indirect nature ($n = 2$). The bandgap energies of $ZnO:Al$, $MAPbI_3$ and Fe_2O_3 are calculated to be 3.21 eV, 1.79 eV and 2.2 eV, respectively, by the measured optical absorption values (Figure 5.8). The results are consistent with the data reported in the literature [122, 127, 128].

5.3 CONCLUSION

The constructed heterostructure system consisting of the following building blocks, namely $ZnO:Al, MAPbI_3$, and Fe_2O_3 and materials exhibited increased improvement of the photocatalytic performance of $MAPbI_3$ by re-adjusting its band edges through coupling with

Fe_2O_3 (110) and $ZnO : Al$ (001). The band edge potentials in $MAPbI_3$ (001) have shifted down in the valence band from 1.15 to 1.45 eV to exceed the required value of 1.23 V at the oxidation edge while maintaining high light absorption in the visible light region. The resulting z-scheme has allowed decreasing the probability of the charges recombination and their lifespan in $MAPbI_3$, thus, leading to an improved hydrogen generation rate under the visible light irradiation attaining a hydrogen production rate of 265.05 $\mu mol/g$ and 362.99 $\mu mol/g$, respectively for neutral pH and acidic pH of 5. Subsequently, the selected compounds composing the $MAPbI_3$ heterostructure, appear to prevent its surface deterioration by covering its side surfaces and to enhance its structural stability in the presence of oxygen and water molecules. These findings represent a key route to develop novel strategies preserving the sensitive $MAPbI_3$ based perovskites at room temperature and in humid environment while maintaining its superlative optical absorption.

Conclusions

Solar energy is the most environmentally friendly and plentiful kind of renewable energy that is currently accessible. In recent years, the age of perovskites has seen a wonderful growth in terms of its progress. Within the category of perovskites, flexible perovskite solar cells have garnered a growing amount of interest as a result of their high efficiency, cheap cost, low weight, and exceptional flexibility. They do not have a comprehensive and correct understanding of many of the qualities, benefits, and advances of these materials because of their newness. On the basis of this, we came to the conclusion that it would be beneficial to conduct an in-depth investigation on the effect of the various approaches that were taken to enhance the characteristics of $CH_3NH_3PbI_3$ in two sections. In the first portion of this study, the band gap of the material was used as a control to explore how strain affects the material's electronic characteristics and electrical conductivity. In addition to this, we looked at the possibility of increasing the power conversion efficiency (PCE) by replacing the cations. According to the findings of the research, there was a discernible increase in the magnitude of these impacts on the electrical properties, as well as a 25 % rise in the PCE. In the second part of this series, we also explored the construction of a heterostructure consisting of Fe_2O_3, $CH_3NH_3PbI_3$, and ZnO for the purpose of splitting water and producing hydrogen gas while preventing $CH_3NH_3PbI_3$ from being degraded by water. The oxidation process has been greatly sped up due to the presence of Fe_2O_3. ZnO is a transparent carrier that shields

$CH_3NH_3PbI_3$ from degradation and, more significantly, transmits electrons while enabling photons of light to reach $CH_3NH_3PbI_3$. The research indicated that there was a production rate of around (150 moles/gram).

Bibliography

[1] Karl Leo. Signs of stability. *Nature nanotechnology*, 10(7):574–575, 2015.

[2] David R Como. Printing the levellers: Clandestine print, radical propaganda, and the new model army. *The Library*, 22(4):441–486, 2021.

[3] Mark T Weller, Oliver J Weber, Paul F Henry, Antonietta M Di Pumpo, and Thomas C Hansen. Complete structure and cation orientation in the perovskite photovoltaic methylammonium lead iodide between 100 and 352 k. *Chemical communications*, 51(20):4180–4183, 2015.

[4] Henry J Snaith. Perovskites: the emergence of a new era for low-cost, high-efficiency solar cells. *The journal of physical chemistry letters*, 4(21):3623–3630, 2013.

[5] PAM Dirac. Proc. camb. phil. soc., 1930.

[6] Brian O'regan and Michael Grätzel. A low-cost, high-efficiency solar cell based on dye-sensitized colloidal tio2 films. *nature*, 353(6346):737–740, 1991.

[7] Yun Wang, Tim Gould, John F Dobson, Haimin Zhang, Huagui Yang, Xiangdong Yao, and Huijun Zhao. Density functional theory analysis of structural and electronic properties of orthorhombic perovskite ch 3 nh 3 pbi 3. *Physical Chemistry Chemical Physics*, 16(4):1424–1429, 2014.

[8] Julian Burschka, Norman Pellet, Soo-Jin Moon, Robin Humphry-Baker, Peng Gao, Mohammad K Nazeeruddin, and Michael Grätzel. Sequential deposition as a route to high-performance perovskite-sensitized solar cells. *Nature*, 499(7458):316–319, 2013.

[9] Xiong Li, Dongqin Bi, Chenyi Yi, Jean-David Décoppet, Jingshan Luo, Shaik Mohammed Zakeeruddin, Anders Hagfeldt, and Michael Grätzel. A vacuum flash–assisted solution process for high-efficiency large-area perovskite solar cells. *Science*, 353(6294):58–62, 2016.

[10] Anthony M Glazer. The classification of tilted octahedra in perovskites. *Acta Crystallographica Section B: Structural Crystallography and Crystal Chemistry*, 28(11):3384–3392, 1972.

[11] Richard J Worhatch, HyunJeong Kim, Ian P Swainson, André L Yonkeu, and Simon JL Billinge. Study of local structure in selected organic–inorganic perovskites in the pm3m phase. *Chemistry of Materials*, 20(4):1272–1277, 2008.

[12] Dieter Weber. Ch3nh3pbx3, ein pb (ii)-system mit kubischer perowskitstruktur/ch3nh3pbx3, a pb (ii)-system with cubic perovskite structure. *Zeitschrift für Naturforschung B*, 33(12):1443–1445, 1978.

[13] Roderick E Wasylishen, Osvald Knop, and J Bruce Macdonald. Cation rotation in methylammonium lead halides. *Solid state communications*, 56(7):581–582, 1985.

[14] Noriko Onoda-Yamamuro, Osamu Yamamuro, Takasuke Matsuo, and Hiroshi Suga. pt phase relations of ch3nh3pbx3 (x= cl, br, i) crystals. *Journal of Physics and Chemistry of Solids*, 53(2):277–281, 1992.

[15] Noriko Onoda-Yamamuro, Takasuke Matsuo, and Hiroshi Suga. Calorimetric and ir spectroscopic studies of phase transitions in methylammonium trihalogenoplumbates (ii). *Journal of Physics and Chemistry of Solids*, 51(12):1383–1395, 1990.

[16] Albrecht Poglitsch and Daniel Weber. Dynamic disorder in methylammoniumtrihalogenoplumbates (ii) observed by millimeter-wave spectroscopy. *The Journal of chemical physics*, 87(11):6373–6378, 1987.

[17] Tom Baikie, Yanan Fang, Jeannette M Kadro, Martin Schreyer, Fengxia Wei, Subodh G Mhaisalkar, Michael Graetzel, and Tim J White. Synthesis and crystal chemistry of the hybrid perovskite (ch 3 nh 3) pbi 3 for solid-state sensitised solar cell applications. *Journal of Materials Chemistry A*, 1(18):5628–5641, 2013.

[18] M Grätzel. Solar water splitting cells. *Nature*, 414:338–344, 2001.

[19] Federico Brivio, Jarvist M Frost, Jonathan M Skelton, Adam J Jackson, Oliver J Weber, Mark T Weller, Alejandro R Goni, Aurélien MA Leguy, Piers RF Barnes, and Aron Walsh. Lattice dynamics and vibrational spectra of the orthorhombic, tetragonal, and cubic phases of methylammonium lead iodide. *Physical Review B*, 92(14):144308, 2015.

[20] Jarvist M Frost, Keith T Butler, and Aron Walsh. Molecular ferroelectric contributions to anomalous hysteresis in hybrid perovskite solar cells. *Apl Materials*, 2(8):081506, 2014.

[21] Christopher Eames, Jarvist M Frost, Piers RF Barnes, Brian C O'regan, Aron Walsh, and M Saiful Islam. Ionic transport in hybrid lead iodide perovskite solar cells. *Nature communications*, 6(1):1–8, 2015.

[22] Walter Kohn and Lu Jeu Sham. Self-consistent equations including exchange and correlation effects. *Physical review*, 140(4A):A1133, 1965.

[23] Nam-Gyu Park. Organometal perovskite light absorbers toward a 20% efficiency low-cost solid-state mesoscopic solar cell. *The Journal of Physical Chemistry Letters*, 4(15):2423–2429, 2013.

[24] Wayne E Buschmann, Atta M Arif, and Joel S Miller. Structure and properties of tetracyanomanganate (ii),[mnii (cn) 4] 2-, the first paramagnetic tetrahedral cyanometalate complex. *Angewandte Chemie International Edition*, 37(6):781–783, 1998.

[25] Kiyoshi Miyata, Timothy L Atallah, and X-Y Zhu. Lead halide perovskites: Crystal-liquid duality, phonon glass electron crystals, and large polaron formation. *Science Advances*, 3(10):e1701469, 2017.

[26] Jingfan Chen and Ya Wang. Personalized dynamic transport of magnetic nanorobots inside the brain vasculature. *Nanotechnology*, 31(49):495706, 2020.

[27] SJ Moon, R Humphry-Baker, JH Yum, and J Moser. 1692 e.; et al. lead iodide perovskite sensitized all-solid-state submicron 1693 thin film mesoscopic solar cell with efficiency exceeding 9%. *Sci. 1694 Rep*, 2:591, 2012.

[28] Yun Wang, Tao Sun, Dongjiang Yang, Hongwei Liu, Haimin Zhang, Xiangdong Yao, and Huijun Zhao. Structure, reactivity, photoactivity and stability of ti–o based materials: a theoretical comparison. *Physical Chemistry Chemical Physics*, 14(7):2333–2338, 2012.

[29] Felix Utama Kosasih and Caterina Ducati. Characterising degradation of perovskite solar cells through in-situ and operando electron microscopy. *Nano Energy*, 47:243–256, 2018.

[30] Jeong-Hyeok Im, Hui-Seon Kim, and Nam-Gyu Park. Morphology-photovoltaic property correlation in perovskite solar cells: One-step versus two-step deposition of ch3nh3pbi3. *Apl Materials*, 2(8):081510, 2014.

[31] Domanski K Correa-Baena JP Nazeeruddin and MK Zakeeruddin SM Tress W Abate. A. hagfeldt a. grätzel m. *Energy Environ. Sci*, 9:1989–1997, 2016.

[32] Y Rong, Y Hu, A Mei, H Tan, MI Saidaminov, and S Seok. Il; mcgehee, md; sargent, eh; han, h. challenges for commercializing perovskite solar cells. *Science*, 361:6408, 2018.

[33] David J Griffiths and Darrell F Schroeter. *Introduction to quantum mechanics*. Cambridge university press, 2018.

[34] E Schrödinger. Schrödinger 1926e. *Annalen der Physik*, 81:109, 1926.

[35] Xiaosong Hu. *Structural studies of oligosaccharides using NMR methods and molecular dynamics simulations*. University of Notre Dame, 2010.

[36] Matthieu Buchs. *A study of the photophysical and photochemical properties of metal complexes using density functional theory*. PhD thesis, Université de Fribourg, 2001.

[37] W. Kohn and L. J. Sham. Self-consistent equations including exchange and correlation effects. *Phys. Rev.*, 140:A1133–A1138, Nov 1965.

[38] Jean-Louis Calais. Density-functional theory of atoms and molecules. rg parr and w. yang, oxford university press, new york, oxford, 1989. ix+ 333 pp. price£ 45.00, 1993.

[39] Pierre Hohenberg and Walter Kohn. Inhomogeneous electron gas. *Physical review*, 136(3B):B864, 1964.

[40] John P Perdew and Alex Zunger. Self-interaction correction to density-functional approximations for many-electron systems. *Physical Review B*, 23(10):5048, 1981.

[41] David M Ceperley and Berni J Alder. Ground state of the electron gas by a stochastic method. *Physical review letters*, 45(7):566, 1980.

[42] Seymour H Vosko, Leslie Wilk, and Marwan Nusair. Accurate spin-dependent electron liquid correlation energies for local spin density calculations: a critical analysis. *Canadian Journal of physics*, 58(8):1200–1211, 1980.

[43] Alain St.-Amant, Wendy D Cornell, Peter A Kollman, and Thomas A Halgren. Calculation of molecular geometries, relative conformational energies, dipole moments, and molecular electrostatic potential fitted charges of small organic molecules of biochemical interest by density functional theory. *Journal of computational chemistry*, 16(12):1483–1506, 1995.

[44] John P Perdew and Yue Wang. Accurate and simple analytic representation of the electron-gas correlation energy. *Physical review B*, 45(23):13244, 1992.

[45] John P Perdew, John A Chevary, Sy H Vosko, Koblar A Jackson, Mark R Pederson, Dig J Singh, and Carlos Fiolhais. Atoms, molecules, solids, and surfaces: Applications of the generalized gradient approximation for exchange and correlation. *Physical review B*, 46(11):6671, 1992.

[46] Max Dion, Henrik Rydberg, Elsebeth Schröder, David C Langreth, and Bengt I Lundqvist. Van der waals density functional for general geometries. *Physical review letters*, 92(24):246401, 2004.

[47] HJ Butt and M Kappl. van der waals forces. *Surface and Interfacial Forces*, 1:43–98, 2018.

[48] John P. Perdew, Kieron Burke, and Matthias Ernzerhof. Generalized gradient approximation made simple. *Phys. Rev. Lett.*, 77:3865–3868, Oct 1996.

[49] Jiri Klimes, D Bowler, and Angelos Michaelides. vdw-df functional of langreth and lundqvist et al. *Phys. Rev. B*, 83:195131, 2011.

[50] Peter E Blöchl, Ove Jepsen, and Ole Krogh Andersen. Improved tetrahedron method for brillouin-zone integrations. *Physical Review B*, 49(23):16223, 1994.

[51] Andrea Dal Corso. A pseudopotential plane waves program (pwscf) and some case studies. In *Quantum-mechanical Ab-initio calculation of the properties of crystalline materials*, pages 155–178. Springer, 1996.

[52] Paolo Giannozzi, Stefano Baroni, Nicola Bonini, Matteo Calandra, Roberto Car, Carlo Cavazzoni, Davide Ceresoli, Guido L Chiarotti, Matteo Cococcioni, Ismaila Dabo, et al. Quantum espresso: a modular and open-source software project for quantum simulations of materials. *Journal of physics: Condensed matter*, 21(39):395502, 2009.

[53] Stefano Baroni, Paolo Giannozzi, and Andrea Testa. Green's-function approach to linear response in solids. *Physical review letters*, 58(18):1861, 1987.

[54] David J Singh. Doping-dependent thermopower of pbte from boltzmann transport calculations. *Physical Review B*, 81(19):195217, 2010.

[55] P Blaha. Wien2k, an augmented plane wave local orbitals program for calculating crystal properties karlheinz schwarz. *Techn. Universität Wien, Austria*, 2001.

[56] G Kresse and J Hafner. Norm-conserving and ultrasoft pseudopotentials for first-row and transition elements. *Journal of Physics: Condensed Matter*, 6(40):8245, 1994.

[57] H Rydberg, E Schröder, DC Langreth, and BI Lundqvist. Van der waals density functional for general geometries. ... *review letters*, 2004.

[58] Antonio Tilocca and Nora H de Leeuw. Structural and electronic properties of modified sodium and soda-lime silicate glasses by car–parrinello molecular dynamics. *Journal of Materials Chemistry*, 16(20):1950–1955, 2006.

[59] Claudio Quarti, Edoardo Mosconi, James M Ball, Valerio D'Innocenzo, Chen Tao, Sandeep Pathak, Henry J Snaith, Annamaria Petrozza, and Filippo De Angelis. Structural and optical properties of methylammonium lead iodide across the tetragonal to cubic phase transition: implications for perovskite solar cells. *Energy & Environmental Science*, 9(1):155–163, 2016.

[60] Edoardo Mosconi, Claudio Quarti, Tanja Ivanovska, Giampiero Ruani, and Filippo De Angelis. Structural and electronic properties of organo-halide lead perovskites: a combined ir-spectroscopy and ab initio molecular dynamics investigation. *Physical chemistry chemical physics*, 16(30):16137–16144, 2014.

[61] MA Pena and JLG Fierro. Chemical structures and performance of perovskite oxides. *Chemical reviews*, 101(7):1981–2018, 2001.

[62] Luke Jonathan, Lina Jaya Diguna, Omnia Samy, Muqoyyanah Muqoyyanah, Suriani Abu Bakar, Muhammad Danang Birowosuto, and Amine El Moutaouakil. Hybrid organic–inorganic perovskite halide materials for photovoltaics towards their commercialization. *Polymers*, 14(5):1059, 2022.

[63] Zhiwei Zhu, Huanhuan Cai, and Da-Wen Sun. Titanium dioxide (tio2) photocatalysis technology for nonthermal inactivation of microorganisms in foods. *Trends in Food Science & Technology*, 75:23–35, 2018.

[64] Nitu Kumari, Sanjaykumar R Patel, and Jignasa V Gohel. Superior efficiency achievement for fapbi3-perovskite thin film solar cell by optimization with response surface methodology technique and partial replacement of pb by sn. *Optik*, 176:262–277, 2019.

[65] Fei Ye, Hong Lin, Haodi Wu, Lu Zhu, Zhanfeng Huang, Dan Ouyang, Guangda Niu, and Wallace CH Choy. High-quality cuboid ch3nh3pbi3 single crystals for high performance x-ray and photon detectors. *Advanced Functional Materials*, 29(6):1806984, 2019.

[66] Mark T Weller, Oliver J Weber, Jarvist M Frost, and Aron Walsh. Cubic perovskite structure of black formamidinium lead iodide, α-[hc (nh2) 2] pbi3, at 298 k. *The journal of physical chemistry letters*, 6(16):3209–3212, 2015.

[67] Janusz Edward Jacak and Witold Aleksander Jacak. Routes for metallization of perovskite solar cells. *Materials*, 15(6):2254, 2022.

[68] Zhichao Zeng, Yueshan Xu, Zheshan Zhang, Zhansheng Gao, Meng Luo, Zongyou Yin, Chao Zhang, Jun Xu, Bolong Huang, Feng Luo, et al. Rare-earth-containing

perovskite nanomaterials: design, synthesis, properties and applications. *Chemical Society Reviews*, 49(4):1109–1143, 2020.

[69] Hiromitsu Takaba, Shou Kimura, and Md Khorshed Alam. Crystal and electronic structures of substituted halide perovskites based on density functional calculation and molecular dynamics. *Chemical physics*, 485:22–28, 2017.

[70] Hongzhe Wen and Xuan Luo. Tuning bandgaps of mixed halide and oxide perovskites cssnx3 (x= cl, i), and srbo3 (b= rh, ti). *Applied Sciences*, 11(15):6862, 2021.

[71] Gregor Kieslich, Shijing Sun, and Anthony K Cheetham. An extended tolerance factor approach for organic–inorganic perovskites. *Chemical science*, 6(6):3430–3433, 2015.

[72] Ruijie Ma, Cenqi Yan, Patrick Wai-Keung Fong, Jiangsheng Yu, Heng Liu, Junli Yin, Jianhua Huang, Xinhui Lu, He Yan, and Gang Li. In situ and ex situ investigations on ternary strategy and co-solvent effects towards high-efficiency organic solar cells. *Energy & Environmental Science*, 2022.

[73] Roshan Ali, Guo-Jiao Hou, Zhen-Gang Zhu, Qing-Bo Yan, Qing-Rong Zheng, and Gang Su. Predicted lead-free perovskites for solar cells. *Chemistry of Materials*, 30(3):718–728, 2018.

[74] Farhad Fouladi Targhi, Yousef Seyed Jalili, and Faramarz Kanjouri. Mapbi3 and fapbi3 perovskites as solar cells: Case study on structural, electrical and optical properties. *Results in physics*, 10:616–627, 2018.

[75] Amina Boubekraoui, Hajar Moatassim, Ahmed Al-Shami, and Hamid Ez-Zahraouy. Dft study of structural, electronic, and thermoelectric properties of cs2pdx (x= br2be2te2) compound. *Computational Condensed Matter*, 29:e00600, 2021.

[76] Denis Stanić, Vedran Kojić, Tihana Čižmar, Krunoslav Juraić, Lara Bagladi, Jimmy Mangalam, Thomas Rath, and Andreja Gajović. Simulating the performance of a formamidinium based mixed cation lead halide perovskite solar cell. *Materials*, 14(21):6341, 2021.

[77] Xiaolin Zhu, Yixiong Lin, Yue Sun, Matthew C Beard, and Yong Yan. Lead-halide perovskites for photocatalytic α-alkylation of aldehydes. *Journal of the American Chemical Society*, 141(2):733–738, 2019.

[78] Ghassane Tiouitchi, Mustapha Ait Ali, Abdelilah Benyoussef, Mohammed Hamedoun, Abdessadek Lachgar, Abdelkader Kara, Ahmed Ennaoui, Abdelfattah Mahmoud, Frederic Boschini, Hamid Oughaddou, et al. Efficient production of few-layer black phosphorus by liquid-phase exfoliation. *Royal Society Open Science*, 7(10):201210, 2020.

[79] Guo Yang, Honglin Chen, Hangdao Qin, and Yujun Feng. Amination of activated carbon for enhancing phenol adsorption: effect of nitrogen-containing functional groups. *Applied Surface Science*, 293:299–305, 2014.

[80] Huanping Zhou, Qi Chen, Gang Li, Song Luo, Tze-bing Song, Hsin-Sheng Duan, Ziruo Hong, Jingbi You, Yongsheng Liu, and Yang Yang. Interface engineering of highly efficient perovskite solar cells. *Science*, 345(6196):542–546, 2014.

[81] Tianran Chen, Benjamin J Foley, Bahar Ipek, Madhusudan Tyagi, John RD Copley, Craig M Brown, Joshua J Choi, and Seung-Hun Lee. Rotational dynamics of or-

ganic cations in the ch 3 nh 3 pbi 3 perovskite. *Physical chemistry chemical physics*, 17(46):31278–31286, 2015.

[82] Alessandro Stroppa, Domenico Di Sante, Paolo Barone, Menno Bokdam, Georg Kresse, Cesare Franchini, Myung-Hwan Whangbo, and Silvia Picozzi. Tunable ferroelectric polarization and its interplay with spin–orbit coupling in tin iodide perovskites. *Nature communications*, 5(1):1–8, 2014.

[83] Ioannis Deretzis, Bruno N Di Mauro, Alessandra Alberti, Giovanna Pellegrino, Emanuele Smecca, and Antonino La Magna. Spontaneous bidirectional ordering of ch3nh3+ in lead iodide perovskites at room temperature: The origins of the tetragonal phase. *Scientific reports*, 6(1):1–7, 2016.

[84] O Mounkachi, E Salmani, M Lakhal, H Ez-Zahraouy, M Hamedoun, M Benaissa, A Kara, A Ennaoui, and A Benyoussef. Band-gap engineering of sno2. *Solar Energy Materials and Solar Cells*, 148:34–38, 2016.

[85] FEI Ruixiang and YANG Li. Strain-engineering the anisotropic electrical conductance of few-layer black phosphorus [j]. *Nano Letters*, 14(5):2884–2889, 2014.

[86] J Bardeen and W Shockley. Deformation potentials and mobilities in non-polar crystals. *Physical review*, 80(1):72, 1950.

[87] Conyers Herring and Erich Vogt. Transport and deformation-potential theory for many-valley semiconductors with anisotropic scattering. *Physical review*, 101(3):944, 1956.

[88] Georg KH Madsen and David J Singh. Boltztrap. a code for calculating band-structure dependent quantities. *Computer Physics Communications*, 175(1):67–71, 2006.

[89] Huizhi Lv, Hongwei Gao, Yue Yang, and Lekun Liu. Density functional theory (dft) investigation on the structure and electronic properties of the cubic perovskite pbtio3. *Applied Catalysis A: General*, 404(1):54–58, 2011.

[90] Linn Leppert, Sebastian E Reyes-Lillo, and Jeffrey B Neaton. Electric field-and strain-induced rashba effect in hybrid halide perovskites. *The journal of physical chemistry letters*, 7(18):3683–3689, 2016.

[91] Christopher Grote and Robert F Berger. Strain tuning of tin–halide and lead–halide perovskites: a first-principles atomic and electronic structure study. *The Journal of Physical Chemistry C*, 119(40):22832–22837, 2015.

[92] Banavoth Murali, Emre Yengel, Wei Peng, Zhijie Chen, Mohd S Alias, Erkki Alarousu, Boon S Ooi, Victor Burlakov, Alain Goriely, Mohamed Eddaoudi, et al. Temperature-induced lattice relaxation of perovskite crystal enhances optoelectronic properties and solar cell performance. *The Journal of Physical Chemistry Letters*, 8(1):137–143, 2017.

[93] Ze Liu, Jefferson Zhe Liu, Yao Cheng, Zhihong Li, Li Wang, and Quanshui Zheng. Interlayer binding energy of graphite: A mesoscopic determination from deformation. *Physical Review B*, 85(20):205418, 2012.

[94] Feng Wang, Jiale Ma, Fangyan Xie, Linkai Li, Jian Chen, Jun Fan, and Ni Zhao. Organic cation-dependent degradation mechanism of organotin halide perovskites. *Advanced Functional Materials*, 26(20):3417–3423, 2016.

[95] Yuping He and Giulia Galli. Perovskites for solar thermoelectric applications: A first principle study of ch3nh3ai3 (a= pb and sn). *Chemistry of Materials*, 26(18):5394–5400, 2014.

[96] Jingxiu Yang, Peng Zhang, and Su-Huai Wei. Band structure engineering of cs2agbibr6 perovskite through order–disordered transition: A first-principle study. *The journal of physical chemistry letters*, 9(1):31–35, 2018.

[97] Fengshuo Zu, Patrick Amsalem, David A Egger, Rongbin Wang, Christian M Wolff, Honghua Fang, Maria Antonietta Loi, Dieter Neher, Leeor Kronik, Steffen Duhm, et al. Constructing the electronic structure of ch3nh3pbi3 and ch3nh3pbbr3 perovskite thin films from single-crystal band structure measurements. *The journal of physical chemistry letters*, 10(3):601–609, 2019.

[98] Mingzhe Zhu, Chongwen Li, Bingyu Li, Jiakang Zhang, Yuqian Sun, Weisi Guo, Zhongmin Zhou, Shuping Pang, and Yanfa Yan. Interaction engineering in organic–inorganic hybrid perovskite solar cells. *Materials Horizons*, 7(9):2208–2236, 2020.

[99] Qingdong Ou, Xiaozhi Bao, Yinan Zhang, Huaiyu Shao, Guichuan Xing, Xiangping Li, Liyang Shao, and Qiaoliang Bao. Band structure engineering in metal halide perovskite nanostructures for optoelectronic applications. *Nano Materials Science*, 1(4):268–287, 2019.

[100] Xin Yu Chin, Daniele Cortecchia, Jun Yin, Annalisa Bruno, and Cesare Soci. Lead iodide perovskite light-emitting field-effect transistor. *Nature communications*, 6(1):1–9, 2015.

[101] Ryotaro Aso, Daisuke Kan, Yuichi Shimakawa, and Hiroki Kurata. Atomic level observation of octahedral distortions at the perovskite oxide heterointerface. *Scientific reports*, 3(1):1–6, 2013.

[102] Shuyi Huang, Haoze Kuang, Taoyu Zou, Lin Shi, Hongsheng Xu, Jinkai Chen, Weipeng Xuan, Shijie Zhan, Yubo Li, Hao Jin, et al. Surface electrical properties

modulation by multimode polarizations inside hybrid perovskite films investigated through contact electrification effect. *Nano Energy*, 89:106318, 2021.

[103] A Al-Shami, M Lakhal, M Hamedoun, A El Kenz, A Benyoussef, M Loulidi, A Ennaoui, and O Mounkachi. Tuning the optical and electrical properties of orthorhombic hybrid perovskite ch3nh3pbi3 by first-principles simulations: strain-engineering. *Solar Energy Materials and Solar Cells*, 180:266–270, 2018.

[104] Sulakshana Shenoy and Kartick Tarafder. Enhanced photocatalytic efficiency of layered cds/cdse heterostructures: Insights from first principles electronic structure calculations. *Journal of Physics: Condensed Matter*, 32(27):275501, 2020.

[105] Donghun Kim, Byung Chul Yeo, Dongbin Shin, Heechae Choi, Seungchul Kim, Noejung Park, and Sang Soo Han. Dissimilar anisotropy of electron versus hole bulk transport in anatase tio 2: Implications for photocatalysis. *Physical Review B*, 95(4):045209, 2017.

[106] KGU Wijayantha and DH Auty. Twin cell technology for hydrogen generation. 2005.

[107] Francis Opoku, Krishna Kuben Govender, Cornelia Gertina Catharina Elizabeth van Sittert, and Penny Poomani Govender. Recent progress in the development of semiconductor-based photocatalyst materials for applications in photocatalytic water splitting and degradation of pollutants. *Advanced Sustainable Systems*, 1(7):1700006, 2017.

[108] Eser M Akinoglu, Dijon A Hoogeveen, Chang Cao, Alexandr N Simonov, and Jacek J Jasieniak. Prospects of z-scheme photocatalytic systems based on metal halide perovskites. *ACS nano*, 15(5):7860–7878, 2021.

[109] Chao Peng, Jianfu Chen, Haifeng Wang, and Peijun Hu. First-principles insight into the degradation mechanism of ch3nh3pbi3 perovskite: light-induced defect formation and water dissociation. *The Journal of Physical Chemistry C*, 122(48):27340–27349, 2018.

[110] Tomasz Jakubczyk, Valentin Delmonte, Maciej Koperski, Karol Nogajewski, Clément Faugeras, Wolfgang Langbein, Marek Potemski, and Jacek Kasprzak. Radiatively limited dephasing and exciton dynamics in mose2 monolayers revealed with four-wave mixing microscopy. *Nano letters*, 16(9):5333–5339, 2016.

[111] H Yockell-Lelièvre, F Lussier, and J-F Masson. Influence of the particle shape and density of self-assembled gold nanoparticle sensors on lspr and sers. *The Journal of Physical Chemistry C*, 119(51):28577–28585, 2015.

[112] Faruk Sani, Suhaidi Shafie, Hong Ngee Lim, and Abubakar Ohinoyi Musa. Advancement on lead-free organic-inorganic halide perovskite solar cells: a review. *Materials*, 11(6):1008, 2018.

[113] Claudio Quarti, Edoardo Mosconi, and Filippo De Angelis. Structural and electronic properties of organo-halide hybrid perovskites from ab initio molecular dynamics. *Physical Chemistry Chemical Physics*, 17(14):9394–9409, 2015.

[114] Jacky Even, Soline Boyer-Richard, Marcelo Carignano, Laurent Pedesseau, Jean-Marc Jancu, and Claudine Katan. Theoretical insights into hybrid perovskites for photovoltaic applications. In *Physics and Simulation of Optoelectronic Devices XXIV*, volume 9742, page 97421A. International Society for Optics and Photonics, 2016.

[115] Jorge J Palop, Lennart Mucke, and Erik D Roberson. Quantifying biomarkers of cognitive dysfunction and neuronal network hyperexcitability in mouse models of

alzheimer's disease: depletion of calcium-dependent proteins and inhibitory hippocampal remodeling. In *Alzheimer's Disease and Frontotemporal Dementia*, pages 245–262. Springer, 2010.

[116] Limin She, Meizhuang Liu, and Dingyong Zhong. Atomic structures of ch3nh3pbi3 (001) surfaces. *Acs Nano*, 10(1):1126–1131, 2016.

[117] Thomas J Mills, Fuding Lin, and Shannon W Boettcher. Theory and simulations of electrocatalyst-coated semiconductor electrodes for solar water splitting. *Physical review letters*, 112(14):148304, 2014.

[118] Sampreetha Thampy, Boya Zhang, Ki-Ha Hong, Kyeongjae Cho, and Julia WP Hsu. Altered stability and degradation pathway of ch3nh3pbi3 in contact with metal oxide. *ACS Energy Letters*, 5(4):1147–1152, 2020.

[119] Cheng Cai, Yuan Teng, Jian-Hao Wu, Jun-Yan Li, Hong-Yan Chen, Jing-Hua Chen, and Dai-Bin Kuang. In situ photosynthesis of an mapbi3/cop hybrid heterojunction for efficient photocatalytic hydrogen evolution. *Advanced Functional Materials*, 30(35):2001478, 2020.

[120] Wenhao Guan, Yi Li, Qixuan Zhong, Haiyu Liu, Jianian Chen, Huicheng Hu, Kangxiao Lv, Jin Gong, Yong Xu, Zhenhui Kang, et al. Fabricating mapbi3/mos2 composites for improved photocatalytic performance. *Nano Letters*, 21(1):597–604, 2020.

[121] Cao Qiang, Deng Jiang-Xia, Liu Guo-Lei, Chen Yan-Xue, Yan Shi-Shen, and Mei Liang-Mo. Epitaxial properties of co-doped zno thin films grown by plasma assisted molecular beam epitaxy. *Chinese Physics Letters*, 24(10):2951, 2007.

[122] Jin Young Kim, Jin-Wook Lee, Hyun Suk Jung, Hyunjung Shin, and Nam-Gyu Park. High-efficiency perovskite solar cells. *Chemical Reviews*, 120(15):7867–7918, 2020.

[123] Ameya Sathe, Munetoshi Seki, Hang Zhou, Jia Xin Chen, and Hitoshi Tabata. Bandgap engineering in v-substituted α-fe2o3 photoelectrodes. *Applied Physics Express*, 12(9):091003, 2019.

[124] Sanjoy C Das, Robert J Green, Jiban Podder, Tom Z Regier, Gap Soo Chang, and Alexander Moewes. Band gap tuning in zno through ni doping via spray pyrolysis. *The Journal of Physical Chemistry C*, 117(24):12745–12753, 2013.

[125] Fatemeh Mazloom, Maryam Masjedi-Arani, Maryam Ghiyasiyan-Arani, and Masoud Salavati-Niasari. Novel sodium dodecyl sulfate-assisted synthesis of zn3v2o8 nanostructures via a simple route. *Journal of Molecular Liquids*, 214:46–53, 2016.

[126] Yang Tian and Tetsu Tatsuma. Plasmon-induced photoelectrochemistry at metal nanoparticles supported on nanoporous tio 2. *Chemical communications*, (16):1810–1811, 2004.

[127] Radka Svobodova Varekova, Zuzanna Jirouskova, Jakub Vanek, Simon Suchomel, and Jaroslav Koca. Electronegativity equalization method: parameterization and validation for large sets of organic, organohalogene and organometal molecule. *International journal of molecular sciences*, 8(7):572–582, 2007.

[128] A Sibari, Z Kerrami, A Kara, and M Benaissa. Strain-engineered p-type to n-type transition in mono-, bi-, and tri-layer black phosphorene. *Journal of Applied Physics*, 127(22):225703, 2020.

Résume

L'énergie solaire est la source d'énergie renouvelable la plus propre et la plus abondante qui existe. Ces dernières années, l'ère des matériaux pérovskites a connu un développement immense. Parmi eux, les cellules solaires flexibles en pérovskite ont reçu une attention croissante en raison de leur haut rendement, légèreté, faible coût et de leur excellente flexibilité. En raison de la nouveauté de ces matériaux, il manque une connaissance complète et précise de leurs propriétés, avantages et développement. Partant de ce constat, nous avons décidé de réaliser une étude approfondie sur l'influence des différentes stratégies utilisées pour améliorer les propriétés du pérovskite **$CH_3NH_3PbI_3$** en deux parties. Dans la première partie, nous avons étudié l'effet de la contrainte sur les propriétés électroniques et la conductivité électrique en contrôlant la bande interdite du matériau. En plus, nous avons étudié l'amélioration de l'efficacité de conversion de puissance (PCE) par le remplacement des cations où l'étude a montré une augmentation significative de ces effets sur les propriétés électroniques et une augmentation du (PCE) à **25%** avec le cation **NH_3OHPbI_3**. Nous avons également discuté dans la deuxième partie de la formation d'une hétérostructure de **Fe_2O_3**, **$CH_3NH_3PbI_3$**, et **ZnO** pour séparer l'eau et produire du gaz hydrogène tout en protégeant **CH3NH3PbI3** de la dégradation par l'eau. **Fe_2O_3** a considérablement augmenté le processus d'oxydation. Quant au **ZnO**, c'est un support transparent qui transfère les électrons tout en permettant aux photons de lumière d'atteindre le **$CH_3NH_3PbI_3$** et surtout de protéger la dégradation du **$CH_3NH_3PbI_3$**. L'étude a montré une production d'environ 151 moles/gramme.

Mots-clefs :
Pérovskite, Photovoltaïque, Photocatalyse, la théorie de la densité fonctionnelle, Effet de contrainte, Cation.

Abstract

Solar energy is the cleanest and most abundant renewable energy source available. In recent years, the era of perovskites has experienced splendid development. Among perovskites, flexible perovskite solar cells have received increasing attention due to their high efficiency, light weight, low cost, excellent flexibility, Due to the novelty of these materials, they lack complete and accurate knowledge of many of their properties, advantages, and development. Based on this, we decided to do an in-depth study on the influence of the different strategies used to improve the properties of **$CH_3NH_3PbI_3$** in two parts. The first part investigated the effect of strain on the electronic properties and electrical conductivity by controlling the band gap of the material. In addition, we investigated the improvement of power conversion efficiency (PCE) through cation replacement. Where the study showed a significant increase of these effects on the electronic properties and an increase in the (PCE)to **25%** with the **NH_3OHPbI_3** cation. We also discussed in the second part the formation of a heterostructure of **Fe_2O_3**, **$CH_3NH_3PbI_3$**, and **ZnO** to split water and produce hydrogen gas while protecting **$CH_3NH_3PbI_3$** from degradation by water. **Fe_2O_3** has significantly increased the oxidation process. As for **ZnO**, it is a transparent carrier that transfers electrons while allowing photons of light to reach **$CH_3NH_3PbI_3$** and most importantly protect the degradation of **$CH_3NH_3PbI_3$**. Where the study showed a production of about **151** moles/gram.

Keywords:

Perovskite, Photovoltaic, Photocatalysis, First-principles calculation, Strain effect, Substation, Cation